Modeling Liquid Film Flow Inside a Vertical Tube

H. Reed Ogrosky

A dissertation submitted to the faculty of the University of North Carolina at Chapel Hill in partial fulfillment of the requirements for the degree of Doctor of Philosophy in the Department of Mathematics.

Chapel Hill
2013

Approved by:

Roberto Camassa

Greg Forest

David Adalsteinsson

Jeremy Marzuola

Rich McLaughlin

ABSTRACT

H. REED OGROSKY: Modeling Liquid Film Flow Inside a Vertical Tube
(Under the direction of Roberto Camassa and Greg Forest)

The flow of a viscous liquid film coating the inside of a vertical tube is studied theoretically and experimentally. As the film flows, small perturbations to the free surface grow in time and space due to the Rayleigh-Plateau instability mode. In the simplest case, the flow of a highly viscous Newtonian film falling due to gravity is considered, and a single model equation is derived using long-wave asymptotics to study the evolution of the free surface. Both linear stability analysis and nonlinear solutions are studied and shown to give excellent agreement with experiments performed in the Joint Fluids Lab.

In the second case, the core of air is forced to flow at a constant volume flux due to an imposed pressure gradient. The stress exerted on the film by the airflow at the interface contributes to the transport of the fluid; at a high enough (upwards) air volume flux, the liquid is transported upwards against gravity. The free surface again exhibits instability growth which in many regimes saturate as a series of traveling waves. We alter the model developed in the first section to include the interfacial stress exerted by the airflow using two different methods, and compare the results of each through linear stability analysis and numerical solutions. The flow of the fluid inside the layer is also studied using streamlines in a traveling reference frame and again compared to experiments.

A comparison is also made between long-wave and thin-film modeling approaches for the problems described above. Qualitative differences in the behavior of numerical solutions to each class of models are explored. Finally, the flow of a non-Newtonian liquid film with shear-thinning properties is briefly studied theoretically for gravity-driven flow.

ACKNOWLEDGMENTS

First, I thank my advisors Roberto Camassa and Greg Forest for their guidance and support. They have provided many valuable insights and suggestions along the way, and I have learned a tremendous amount from them. I am also very grateful for helpful discussions with the other members of my committee, David Adalsteinsson, Jeremy Marzuola, and Rich McLaughlin, as well as Long Lee and Leah Vicci for helpful conversations concerning the modeling and experiments, respectively. I am grateful to many other faculty, too many to name here, who have shaped my thinking as well, and I thank the department as a whole for its support.

I also thank Jeff Olander in the physics department for many helpful conversations and ideas and many hours of hard work on experiments. I thank Michael Jenkinson, John Mellnik, Shreyas Tikare, Jeeho Kim, and Girard Iervolino for their experimental contributions and ideas.

Words cannot express how important the support of my family has been over the last four years. I am so thankful for the joy, love and encouragement that my wife Carolyn and son Josh fill our home with. I am also very grateful for the support of my parents, who have always encouraged me to continue learning.

Finally, I thank God for his provisions, love, grace and strength.

TABLE OF CONTENTS

LIST OF TABLES

LIST OF FIGURES

CHAPTER 1

Introduction

This thesis considers the flow of a liquid film lining the inside of a rigid vertical tube. Such flows arise naturally in various applications ranging from engineering to biology. The work presented here is in part motivated by a desire to better understand the movement of mucus lining the upper airways due to the effects of breathing and gravity. The bulk of this work will focus on two situations: (i) the flow of a liquid film downwards due to gravity, and (ii) the flow of a liquid film upwards due to steady upwards airflow in the core region overcoming the effects of gravity on the liquid.

Such liquid film flows have received much attention over the last century, and there is a large body of work upon which to ground the current study. Stability analysis of such flows reveal that the free surface in these cylindrical settings are unstable to long-wave perturbations; this is the Rayleigh-Plateau instability. Much modeling work has been done to explore these instabilities. Historically, modeling innovations have typically begun in the flat-film setting and then been subsequently altered for the cylindrical geometries of interest here. Models developed over the last three decades have generally fallen into one of four categories: (i) weakly nonlinear models, (ii) thin-film asymptotic models, (iii) long-wave asymptotic models, and (iv) integral models. Weakly nonlinear, thin-film, and long-wave asymptotic models are all derived by exploiting a small ratio of lengthscales, either film perturbation to film thickness, film thickness to cylinder thickness, or radial to axial lengthscale, respectively. In each case a single evolution equation can be found for the location of the fluid-air free surface. The progressive development of such models has generally been in the order listed above, as each successive assumption is less restrictive but typically leads to more complicated models than the previous one. Solutions to such models have been studied both theoretically and numerically. Integral models have been developed over the last decade to examine flows with moderate Reynolds

number by departing from the traditional long-wave expansion when calculating the first- and second-order corrections. The result is a system of coupled PDEs, usually two, that describe the location of the free surface and the local flux. Relevant examples and comments will be made about each type of model in Chapters 2-5 (and further discussion of the various approaches can also be found in [12; 61]).

1.1. Outline

An outline of this thesis is now given. In Section 1.2 exact solutions and their stability are discussed for gravity-driven film flow. A brief overview of experiments conducted in the UNC Joint Fluids Lab and some motivation for the present long-wave modeling study is given. Section 1.3 discusses exact solutions and their stability for core-annular flow; corresponding experiments are again briefly explained.

The case of gravity-driven flow is discussed further in Chapter 2. Long-wave asymptotics is used to model the film-flow and both linear stability analysis and numerical solutions are used to explore the primary features of the model. Stability from both a temporal and spatial viewpoint will be discussed, and the tendency of the film to pinch off and form liquid bridges, or plugs, due to the Rayleigh-Plateau instability is examined. Comparisons are made between the long-wave model, the corresponding thin-film model, and experiments. Traveling wave solutions are found to the long-wave model and the underlying fluid flow is briefly examined by switching to a traveling reference frame and studying the streamline topology.

The case where air is forced to flow due to an imposed pressure gradient is examined in Chapter 3. The leading-order effects of the free-surface stress due to the airflow are found, leading to a 'locally Poiseuille' model. The resulting model is compared with its thin-film counterparts, and several other models are recovered in the appropriate limits.

There are several interesting differences in the behavior of solutions to the long-wave and thin-film models. A detour is made in Chapter 4 to examine the ramifications of making the thin-film assumption in the case of core-annular flows with equal density fluids. Differences in instability growth, wave mergers, and streamline topology in a traveling reference frame are explored.

While the long-wave modeling approach for the airflow problem in Chapter 3 appears to be more satisfactory than the thin-film approach, Chapter 5 shows that comparisons with experiments indicate the long-wave model is not quantitatively accurate. As this is apparently due to insufficient modeling of the stress at the free-surface, a refinement to the model is suggested. Comparisons are made between the two models and other models and experiments in the literature in both flat and cylindrical geometry. Finally, a summary is included in Chapter 6.

1.2. Axisymmetric gravity-driven film flow

We first consider the case of gravity-driven film flow, where a liquid film coating the inside of a tube falls downward due to gravity.

1.2.1. Exact solutions and their stability. The film flow is governed by the axisymmetric, incompressible Navier-Stokes equations in cylindrical coordinates:

$$\begin{aligned}
\rho(\bar{u}_{\bar{t}} + \bar{u}\bar{u}_{\bar{r}} + \bar{w}\bar{u}_{\bar{z}}) &= -\bar{p}_{\bar{r}} + \mu\left(\frac{1}{\bar{r}}\partial_{\bar{r}}(\bar{r}\bar{u}_{\bar{r}}) + \bar{u}_{\bar{z}\bar{z}} - \frac{\bar{u}}{\bar{r}^2}\right), \\
\rho(\bar{w}_{\bar{t}} + \bar{u}\bar{w}_{\bar{r}} + \bar{w}\bar{w}_{\bar{z}}) &= -\bar{p}_{\bar{z}} + \mu\left(\frac{1}{\bar{r}}\partial_{\bar{r}}(\bar{r}\bar{w}_{\bar{r}}) + \bar{w}_{\bar{z}\bar{z}}\right) + \rho g, \\
\frac{1}{\bar{r}}\partial_{\bar{r}}(\bar{r}\bar{u}) + \bar{w}_{\bar{z}} &= 0,
\end{aligned} \tag{1.2.1}$$

where the coordinates are $(\bar{r}, \bar{\theta}, \bar{z})$, with associated velocity components $(\bar{u}, \bar{v}, \bar{w})$. Here $\bar{p}$ is pressure, ρ is density, μ is molecular viscosity, g is gravity, and axisymmetry dictates that $\bar{v} = \partial_{\bar{\theta}} = 0$. All dimensional quantities are marked by overbars (except for those quantities that are obviously dimensional, e.g. μ), and subscripts denote partial derivatives. The coordinate system is oriented so that $\bar{z}$ increases moving down the tube (see Figure 1.2.1).

There is an exact Poiseuille-like solution to (1.2.1) where $\bar{u} = 0$ and $\partial_{\bar{z}} = 0$ with flat interface at $\bar{r} = \bar{R}_0$. The axial velocity is

$$\bar{w} = -\frac{\rho g}{4\mu}\bar{r}^2 + A_1 \ln \bar{r} + A_2, \tag{1.2.2}$$

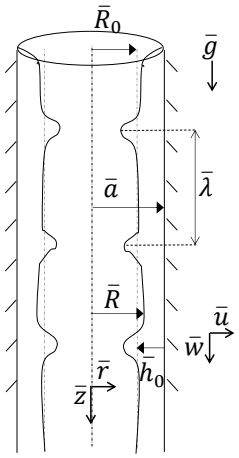

Figure 1.2.1: Variables definition sketch: gravity-driven flow.

and the boundary conditions

$$\bar{w}(\bar{a}) = 0, \tag{1.2.3}$$

$$\partial_{\bar{r}}\bar{w}|_{\bar{r}=\bar{R}_0} = 0, \tag{1.2.4}$$

are no-slip at the wall and continuity of tangential stress at the free surface, respectively. This gives

$$\bar{w} = \frac{\rho g}{4\mu}(\bar{a}^2 - \bar{r}^2) + \frac{\rho g}{2\mu}\bar{R}_0^2 \ln\frac{\bar{r}}{\bar{a}}. \tag{1.2.5}$$

In the experimental studies presented here, the film thickness is not determined *a priori*, but rather the volume flux of liquid is imposed. This results in a flux condition which must be satisfied,

$$\bar{Q} = \int_{\bar{R}_0}^{\bar{a}} 2\pi\bar{r}\bar{w}d\bar{r}. \tag{1.2.6}$$

Thus for a given liquid and volume flux $\bar{Q}$, the film thickness $\bar{h}_0 = \bar{a} - \bar{R}_0$ is then uniquely determined.

For later reference, we note that if the momentum equations are nondimensionalized with the film thickness $\bar{h}_0$ as the lengthscale and $\bar{W}_0 = g\bar{h}_0^2\rho/\mu$ as the velocity scale, then the

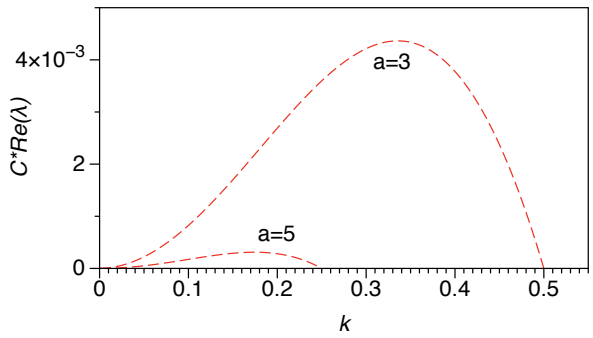

Figure 1.2.2: Non-dimensional growth rate Re(λ) as function of wavenumber k for two different film thicknesses. $C = \mu \bar{W}_0/\gamma$ is the capillary number, where γ is the surface tension.

nondimensional axial velocity is

$$w = \frac{1}{4}\left(a^2 - r^2 + 2R_0^2 \ln \frac{r}{a}\right). \tag{1.2.7}$$

Both experiments and analysis show that this flow is unstable to free surface perturbations. Goren [22] studied the stability of such flows for fluids with high and low viscosity. In the limiting case of a highly viscous liquid for which the inertial effects are insignficant, the governing equations can be simplified to the Stokes equations by neglecting the inertial terms. Analysis of the Stokes equations with a small-amplitude perturbation to the pressure, velocity, and interface allows the stream-function to be expressed in terms of Bessel functions. The boundary conditions (at the wall, no-slip; at the free surface, continuity of tangential stress, jump in normal stress as determined by the Young-Laplace equation, and the kinematic boundary condition) are used to determine the constants of integration in the expression for the streamfunction, and hence determine the stability of the free surface. It is found that there is a band of small wavenumbers to which the free surface is unstable while it is stable for large wavenumbers. The details of the analysis were repeated by the author, but are omitted here and can be found elsewhere (e.g. [22; 11]). Figure 1.2.2 displays the growth rate as a function of wave number for two different film thicknesses. There is a positive growth rate associated with small wavenumbers k; large wavenumbers have negative growth rate. In Chapter 2 we will thus pursue a long-wave model to further explore these instabilities.

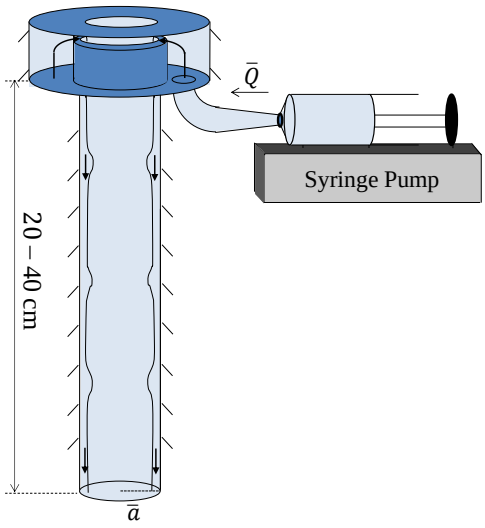

Figure 1.2.3: Experimental setup: gravity-driven flow.

1.2.2. Experiments. These instabilities were observed in experiments conducted by the author in the UNC Joint Fluids Lab. In the experiments, a Harvard Apparatus Syringe Pump was used to pump a viscous silicone oil at a prescribed volume flux $\bar{Q}$. The oil was fed through plastic tubing into the bottom of a chamber. The oil was forced to fill the chamber; upon reaching the top of the chamber, the oil was forced through a radial slit into the core region of the chamber. A glass tube of inner diameter $\bar{a}$ was inserted into the bottom of the core region of the oil chamber so that oil forced through the slit fell downward coating the tube. The glass tube was held in place by a series of O-rings. In early stages of the experiments, glass tubes of several different lengths were used; the data presented here was collected using 40 cm tubes unless otherwise specified. The tubes used had inner radius of $\bar{a} = 0.5$ cm, $\bar{a} = 0.295$ cm, and $\bar{a} = 0.17$ cm. The tube with largest inner radius fit snugly into the O-rings; the tubes of smaller radius were held in place by a rubber stopper wrapped around the top of the tube. See Figure 1.2.3 for a depiction of the experiment; Table 1.1 shows the range of volume fluxes $\bar{Q}$ used for each tube radius $\bar{a}$.

Early experiments used silicone oils with viscosities of $\mu = 129$ P and $\mu = 10$ P. The viscosities were verified by Jeff Olander using a rheometer in the lab; the viscosities were consistent over a wide range of shear rates, indicating that the oils were indeed Newtonian.

$\bar{a}$ (cm)	$\bar{Q}_{max}$ (cm^3/s)	$\bar{Q}_{min}$ (cm^3/s)
0.50	2.2×10^{-1}	8.9×10^{-3}
0.259	1.7×10^{-2}	7.4×10^{-4}
0.17	1.6×10^{-3}	2.2×10^{-4}

Table 1.1: Maximum and minimum liquid volume flow rates $\bar{Q}$ used for each tube radius $\bar{a}$.

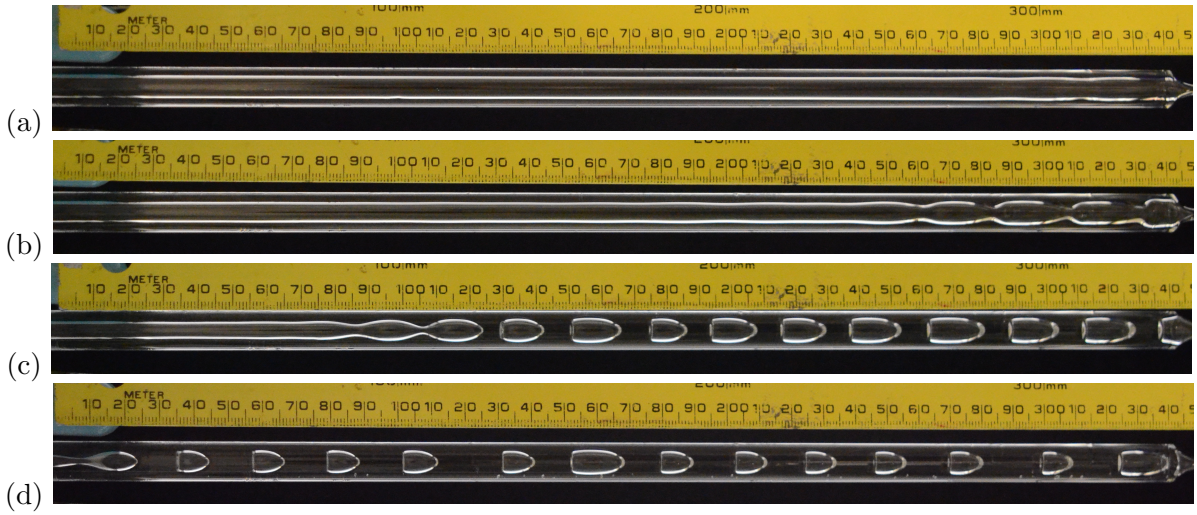

Figure 1.2.4: Snapshots of four experiments with $\mu = 129$ P and $\overline{a} = 0.5$ cm. (a) $\bar{Q} = 4.77 \times 10^{-2}$ cm^3/s, (b) $\bar{Q} = 6.74 \times 10^{-2}$ cm^3/s, (c) $\bar{Q} = 9.56 \times 10^{-2}$ cm^3/s, and (d) $\bar{Q} = 1.40 \times 10^{-1}$ cm^3/s. Acceleration due to gravity g acts from left to right.

Some difficulties arose in taking weight measurements with the $\mu = 10$ P oil due to the higher oil velocity; the data presented here is for $\mu = 129$ P unless otherwise indicated. The density of the oils was measured to be $\rho = 0.97$ g/cm^3. The surface tension of silicone oils with these viscosities is reported in the literature to be $\gamma \approx 21.5$ dyn/cm.

For large enough flow rates, as the film flows down under the influence of gravity, tiny perturbations grow into visible instabilities; Figure 1.2.4 shows snapshots of several different experiments. These instabilities either grow unchecked until they pinch off and clog the tube, creating a 'liquid bridge' or plug which separates the continuous core of air into two regions, or form a series of small-amplitude pulses which travel down the tube. In Chapter 2 this instability growth will be studied by tracking properties such as wavelength, speed, and the location in the tube of first visible growth and, if it occurred, liquid bridge formation. But before proceeding, one comparison between the exact solution and the experiments is made.

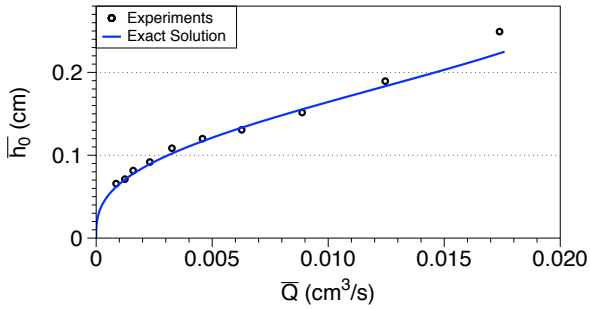

Figure 1.2.5: Comparison of volume flux and mean film thickness between gravity-driven exact solution and experiments for $\mu = 129$ P and $\overline{a} = 0.295$ cm.

In the experiments, the volume flux is held constant while the mean thickness of the film is not prescribed but settles to some value. To determine whether the exact solution (1.2.5) correctly predicts the experimental film thickness for a given liquid flux, it was necessary to calculate the mean thickness of the liquid film for each experiment. This was done by allowing each experiment to progress until a quasi-steady state had been reached. The tube was then removed from the oil chamber and weighed. Using the weight of the dry tube, the density of the oil, and assuming that the liquid film is distributed evenly from the top to the bottom of the tube, the mean thickness was calculated using simple geometry.

Figure 1.2.5 compares the thicknesses of the oil in each experiment with the flux-thickness dependence predicted by the exact solution for $\bar{a} = 0.295$ cm. Excellent agreement is seen when the film is not too thick, i.e. $\bar{h}_0 < 0.1$ cm. Thicker films form liquid bridges very near the inlet, so it is not surprising that there is disagreement between the exact solution and experiments.

1.3. Axisymmetric core-annular flow

The case of core-annular flow is now examined, where one fluid occupies the core region while another occupies an annulus coating the wall. Both fluids are forced to flow due to an imposed pressure gradient and/or gravity. There is a free-surface separating the two immiscible fluids, and the fluids may have unequal densities and unequal viscosities.

1.3.1. Exact solutions and their stability. The flow of both the annular liquid and the core fluid (here gas) is determined by the axisymmetric, incompressible Navier-Stokes equations

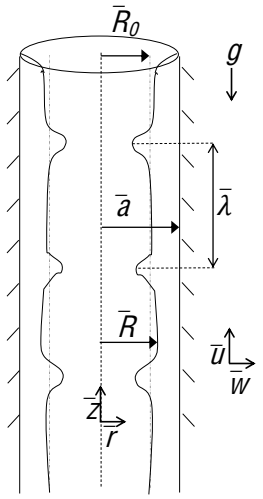

Figure 1.3.1: Variables definition sketch: core-annular flow.

in cylindrical coordinates:

$$\begin{aligned}
\rho^i(\bar{u}^i_{\bar{t}} + \bar{u}^i\bar{u}^i_{\bar{r}} + \bar{w}^i\bar{u}^i_{\bar{z}}) &= -\bar{p}^i_{\bar{r}} + \mu^i\left(\frac{1}{\bar{r}}\partial_{\bar{r}}(\bar{r}\bar{u}^i_{\bar{r}}) + \bar{u}^i_{\bar{z}\bar{z}} - \frac{\bar{u}^i}{\bar{r}^2}\right),\\
\rho^i(\bar{w}^i_{\bar{t}} + \bar{u}^i\bar{w}^i_{\bar{r}} + \bar{w}^i\bar{w}^i_{\bar{z}}) &= -\bar{p}^i_{\bar{z}} + \mu^i\left(\frac{1}{\bar{r}}\partial_{\bar{r}}(\bar{r}\bar{w}^i_{\bar{r}}) + \bar{w}^i_{\bar{z}\bar{z}}\right) - \rho^i g,\\
\frac{1}{\bar{r}}\partial_{\bar{r}}(\bar{r}\bar{u}^i) + \bar{w}^i_{\bar{z}} &= 0,
\end{aligned} \tag{1.3.1}$$

where $i = (l)$ corresponds to the liquid annulus and $i = (g)$ to the core (which is the region occupied by gas in the experiments considered here). As we will primarily be interested in the case where the film flows up the tube, the coordinate system is here oriented so that $\bar{z}$ increases moving up the tube (see Figure 3.1.1).

There is again an exact Poiseuille-like solution to (1.3.1) where $\bar{u}^{(l,g)} = 0$, $\partial_{\bar{z}} = 0$ and the free surface is again flat, i.e. $\bar{r} = \bar{R}_0$. The axial velocities of the liquid and gas are

$$\bar{w}^{(l)} = \frac{\bar{r}^2}{4\mu^{(l)}}(\bar{p}_{\bar{z}} + \rho^{(l)}g) + A_1\ln\bar{r} + A_2, \tag{1.3.2}$$

$$\bar{w}^{(g)} = \frac{\bar{r}^2}{4\mu^{(g)}}(\bar{p}_{\bar{z}} + \rho^{(g)}g) + A_3, \tag{1.3.3}$$

respectively. There is no term containing $\ln\bar{r}$ in the gas velocity in order to ensure finite velocity at $\bar{r} = 0$. The remaining three constants of integration A_j are determined by the three boundary

conditions

$$\bar{w}^{(l)}(\bar{a}) = 0, \tag{1.3.4}$$

$$\bar{w}^{(l)}(\bar{R}_0) = \bar{w}^{(g)}(\bar{R}_0), \tag{1.3.5}$$

$$\partial_{\bar{r}}\bar{w}^{(l)}|_{\bar{r}=\bar{R}_0} = \partial_{\bar{r}}\bar{w}^{(g)}|_{\bar{r}=\bar{R}_0}, \tag{1.3.6}$$

which are no-slip at the wall, continuity of velocity and of tangential stress at the free surface, respectively. This gives

$$\bar{w}^{(l)} = \frac{\bar{r}^2 - \bar{a}^2}{4\mu^{(l)}}(\bar{p}_{\bar{z}} + \rho^{(l)}g) + \frac{g\bar{R}_0^2}{2\mu^{(l)}}(\rho^{(g)} - \rho^{(l)})\ln\frac{\bar{r}}{\bar{a}}, \tag{1.3.7}$$

$$\bar{w}^{(g)} = \frac{\bar{r}^2 - \bar{R}_0^2}{4\mu^{(g)}}(\bar{p}_{\bar{z}} + \rho^{(g)}g) + \frac{\bar{R}_0^2 - \bar{a}^2}{4\mu^{(l)}}(\bar{p}_{\bar{z}} + \rho^{(l)}g) + \frac{g\bar{R}_0^2}{2\mu^{(l)}}(\rho^{(g)} - \rho^{(l)})\ln\frac{\bar{R}_0}{\bar{a}}. \tag{1.3.8}$$

As with the gravity-driven film flow, in the experimental studies presented here the film thickness and pressure gradient are not determined *a priori*; rather, the volume fluxes of air and liquid are imposed and the pressure gradient and film thickness vary accordingly. Thus there are now two unknowns, $\bar{p}_{\bar{z}}$ and $\bar{R}_0$, and two additional conditions

$$\bar{Q}^{(l)} = \int_{\bar{R}_0}^{\bar{a}} 2\pi\bar{r}\bar{w}^{(l)}d\bar{r}, \tag{1.3.9}$$

$$\bar{Q}^{(g)} = \int_0^{\bar{R}_0} 2\pi\bar{r}\bar{w}^{(g)}d\bar{r}, \tag{1.3.10}$$

which can be used to solve for $\bar{p}_{\bar{z}}$ and $\bar{R}_0$. After some algebra the following implicit equation is found for $\bar{R}_0$:

$$\begin{aligned}
&-8\mu^{(g)}\mu^{(l)}Q^{(g)}(\bar{a}^2 - \bar{R}_0^2)^2 + 16\mu^{(g)}\mu^{(l)}Q^{(l)}\bar{R}_0^2(\bar{a}^2 - \bar{R}_0^2) + 8(\mu^{(l)})^2Q^{(l)}\bar{R}_0^4 \\
&+4\pi g\mu^{(g)}(\rho^{(g)} - \rho^{(l)})\bar{R}_0^4(\bar{a}^2 - \bar{R}_0^2)^2 - \pi g\mu^{(l)}(\rho^{(g)} - \rho^{(l)})\bar{R}_0^4(\bar{a}^2 - \bar{R}_0^2)(\bar{a}^2 - 3\bar{R}_0^2) \\
&+4\pi g(\rho^{(g)} - \rho^{(l)})\bar{R}_0^4[(\bar{a}^4 - \bar{R}_0^4)\mu^{(g)} + \bar{R}_0^4\mu^{(l)}]\ln(\bar{R}_0/\bar{a}) = 0.
\end{aligned} \tag{1.3.11}$$

For a given liquid and volume fluxes $\bar{Q}^{(g)}$ and $\bar{Q}^{(l)}$, the film thickness is then uniquely determined by (1.3.11). The corresponding equation for $\bar{R}_0$ in the case of gravity-driven film flow can be recovered by setting $\mu^{(g)} = 0$. If the momentum equations are nondimensionalized, this time with the core thickness $\bar{R}_0$ as the lengthscale and the centerline laminar gas velocity

$\bar{W}_c = 2\bar{Q}^{(g)}/\pi\bar{R}_0^2$ as the velocity scale, then the axial velocities are given by

$$w^{(l)} = \frac{1}{4}(r^2 - a^2)\left(p_z + \frac{Re}{Fr^2}\right) - \frac{Re}{2Fr^2}\ln\frac{r}{a}, \tag{1.3.12}$$

$$w^{(g)} = \frac{m}{4}(r^2 - 1)\left(p_z + \frac{1}{l}\frac{Re}{Fr^2}\right) + \frac{1}{4}(1 - a^2)\left(p_z + \frac{Re}{Fr^2}\right) + \frac{1-l}{l}\frac{Re}{2Fr^2}\ln\frac{1}{a}, \tag{1.3.13}$$

where $Re = \rho^{(l)}\bar{R}_0\bar{W}_0/\mu^{(l)}$ is the Reynolds number, $Fr = \bar{W}_0/\sqrt{g\bar{R}_0^2}$ is the Froude number, $m = \mu^{(l)}/\mu^{(g)}$ is the viscosity ratio and $l = \rho^{(l)}/\rho^{(g)}$ is the density ratio of the fluids.

The stability of core-annular flows due to density and viscosity stratification was studied by Hickox [25], who adapted the long-wavenumber method developed by Yih [82] for flat films. By expressing small linear disturbances to the velocities and pressure as power series in wavenumber and taking the small wavenumber asymptotic limit, the propagation speed of an infinitesimal disturbance is determined at zeroth order and its stability at first order. Hickox showed that while pipe flow of a single fluid is stable to infinitesimal perturbations, core-annular flow can be unstable to long-wave perturbations at any Reynolds number. He found the speed and growth rate of such instabilities in both axisymmetric and asymmetric core-annular flows and his results have been verified [35]. A few of his results are given in Section 3.3 and compared with the models derived in Chapter 3.

1.3.2. Experiments. Another set of experiments similar to those described in Section 1.2 was performed to study the airflow problem; the experiments were conducted in the UNC Joint Fluids Lab by Jeff Olander and a team of undergraduate students. As before a Harvard Apparatus Syringe Pump was used to pump a viscous silicone oil at a prescribed volume flux $\bar{Q}^{(l)}$ through plastic tubing into the bottom of an oil chamber. The oil was forced to fill the chamber; upon reaching the top of the chamber, the oil was forced through a radial slit into the core region of the chamber. Unlike the gravity-driven experiments, a glass tube of inner diameter $\bar{a}$ was inserted into the top of the chamber, held in place by a series of O-rings. Several different length tubes were used in the experiments; the data presented here was collected using a tube with length $L = 20$ cm and inner radius $\bar{a} = 0.5$ cm. The oils used had viscosity $\mu^{(l)} = 129$ P and $\mu^{(l)} = 600$ P.

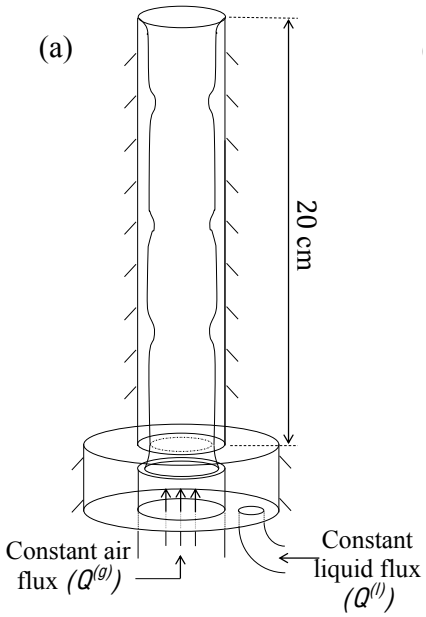

Figure 1.3.2: Experimental setup: core-annular flow.

The air in the tube was forced to flow upwards at a fixed volume flux $\bar{Q}^{(g)}$ by a Direct Flow Controller (DFC). Plastic tubing connected the DFC to the oil chamber so that as the oil entered the chamber, it was forced upwards into the tube by the airflow. Figure 1.3.2 shows a schematic diagram of the experimental setup; Table 1.2 shows the volume flow rates of air and liquid used with each oil.

As in the gravity-driven experiments in Section 1.2, free surface instabilities are visible in the tube. Unlike the gravity-driven instabilities the liquid film was never observed to form liquid bridges. (Liquid bridge formation was observed in early experiments conducted at much lower airflow rates than those reported here). These instabilities will be studied in Chapters 3-5;

$\mu^{(l)}$ (P)	$\bar{Q}^{(l)}$ (cm^3/s)	$\bar{Q}^{(g)}_{min}$ (cm^3/s)	$\bar{Q}^{(g)}_{max}$ (cm^3/s)
129	0.6	3.3×10^2	1.0×10^3
129	1.0	3.3×10^2	1.0×10^3
600	0.6	3.3×10^2	1.17×10^3
600	1.0	3.3×10^2	1.17×10^3

Table 1.2: Maximum and minimum air volume fluxes $\bar{Q}^{(g)}$ used for each oil viscosity $\mu^{(l)}$ and liquid volume flux $\bar{Q}^{(l)}$.

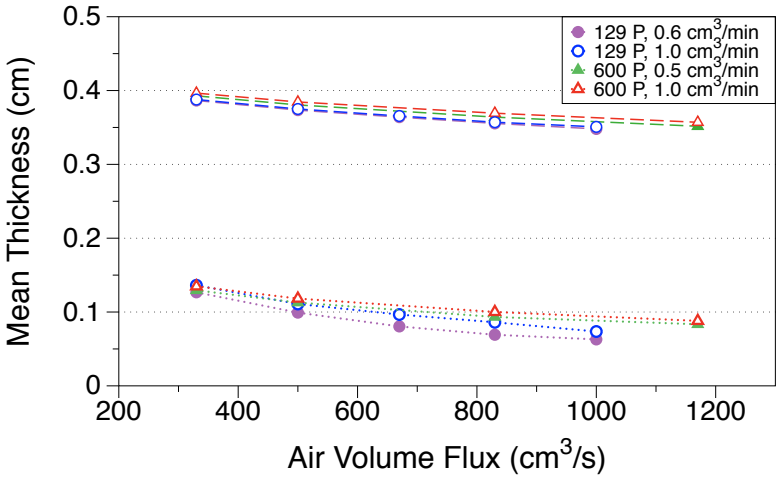

Figure 1.3.3: Comparison of volume flux and mean film thickness between core-annular exact solution and experiments for various viscosities $\mu^{(l)}$, liquid fluxes $\bar{Q}^{(l)}$ and air fluxes $\bar{Q}^{(g)}$. Dotted lines indicate trends in experimental data; dashed lines represent exact solution predictions. Experiments conducted by Jeff Olander *et al.*

before proceeding, the flux-thickness comparison between the exact solution (1.3.7)-(1.3.8) and the experiments is made for the airflow problem.

As with the gravity-driven film flow the liquid volume flux is held constant in the experiments while the mean thickness of the film is not prescribed but settles to some value. To determine whether the exact solution (1.3.7)-(1.3.8) correctly predicts the experimental film thickness for a given liquid flux, the mean thickness of the liquid film was calculated for each experiment. See Section 1.2 for a description of how this was achieved. Figure 1.3.3 compares the thicknesses of the oil in each experiment with the flux-thickness dependence predicted by the exact solution. Results are presented for six flow rates, two liquid volume fluxes, and two liquid viscosities. While the exact solution qualitatively predicts trends in thickness as each parameter changes, in all cases the quantitative agreement is poor; the exact solution consistently overstates the film thickness. The instabilities thus play a prominent role in the evolution of the basic film flow; models will be developed in Chapters 3 & 5 to study the problem.

CHAPTER 2

Gravity-driven film flow

The instabilities predicted by linear stability analysis of the Stokes equations and seen in experiments are now explored through long-wave asymptotic modeling. It should be noted that the problem considered here, gravity-driven film flow on the interior of a rigid vertical tube, has a natural counterpart, namely the same flow on the exterior of a tube. Much can be learned from the exterior problem, which has seen much work over the last several decades due to its numerous industrial applications. Before deriving the models a discussion of the literature for both the interior and exterior coating problems is given.

As is the case for interior models, exterior modeling efforts include weakly nonlinear, thin-film [24; 18; 69], long-wave [48; 43; 11], and integral models [78; 77; 73; 58; 59; 71]. (This is not an exhaustive list of modeling approaches; see, e.g., [68] for a centre-manifold approach). Weakly nonlinear, thin-film and long-wave asymptotic models all consist of a single evolution equation for the free surface. Hammond (1983) considered the growth of instabilities driven by capillary forces in a thin film in cylindrical geometry without the effects of gravity and studied the formation of stationary waves, or collars and lobes [24]. Frenkel [18] derived an evolution equation that included the effects of gravity. This model was studied by Kerchman & Frenkel [39] and Kalliadasis & Chang [36], who noted the finite-time blow-up of its solutions and studied its behavior near blow-up using self-similar solutions. Both the Hammond and Frenkel models are valid for both interior and exterior coatings. Roy *et al.* [69] derived a more refined thin-film model for exterior coatings that conserves mass.

Long-wave models have been derived by Lin & Liu [48] for both the interior and exterior coating, and Kliakhandler, Davis & Bankoff [43] and Craster & Matar [11] for the exterior coating only. We shall hereafter refer to these three long-wave models as the LL, KDB, and CM models, respectively. The derivation of the KDB model is performed in a somewhat ad-hoc

fashion, though the resulting single evolution equation is virtually identical to the CM model, whose derivation is based not only on long-wave asymptotics but also small Bond number, where the Bond number, $Bo = \rho g \bar{R}_0^2/\gamma$, is set equal to the long-wave parameter $\epsilon = \bar{R}_0/\bar{\lambda}$, where γ is surface tension and $\bar{\lambda}$ is a typical wavelength. Experimental work on the exterior problem includes that by Quere [67] who studied the formation and movement of beads flowing down a wetted fiber. More recent experiments done by Smolka, North & Guerra [74] have shown that the CM model accurately captures the linear stability of an exterior film flow with low to moderate Reynolds number.

While much from exterior modeling can be applied to interior coatings, one critical difference is that with interior coatings, if the film is thick enough, RP instabilities can grow unchecked until they pinch off and form a liquid plug or bridge. Lister *et al.* [49] used the Hammond equation to study the behavior of liquid collars and lobes without the effects of gravity, showing that oscillatory movement is possible. Jensen [30] studied the tendency of draining liquid collars to form plugs using the Frenkel model, and found a critical modified Bond number below which plugs form. Once a plug has formed, its movement with constant velocity or forced by a constant pressure gradient has been studied by Ubal *et al.* [6; 80], where the tendency of a plug to thin or thicken is studied along with the flow streamlines within the fluid. Other studies have focused on plug behavior in other geometries, including a channel [75] and flexible tube [23].

In Section 2.2, two long-wave models are derived, one of which is the interior version of the CM model. Comparisons are made to their thin-film counterparts in Section 2.3, and their linear stability properties are discussed in Section 2.4. The model solutions and their corresponding traveling wave solutions are explored and compared to experiments in Sections 2.5 and 2.6.

2.1. Governing equations and leading-order solution

The flow of a Newtonian liquid film is governed by the incompressible axisymmetric Navier-Stokes equations in cylindrical coordinates (1.2.1). Once again we let $\bar{z}$ increase as we move down the tube since the flow is gravity driven; see Figure 1.2.1.

The mean thickness of the film is given by $\bar{h}_0 = \bar{a} - \bar{R}_0$ where $\bar{R}_0$ is the mean radius of the free surface and $\bar{a}$ is the radius of the tube. If the free surface is perturbed and has

some typical wavelength $\bar{\lambda}$, we say that the perturbations are long-wave if $\bar{h}_0/\bar{\lambda} = \epsilon \ll 1$. Nondimensionalizing (1.2.1) using

$$r = \bar{r}/\bar{h}_0, \quad z = \bar{z}/\bar{\lambda}, \quad u = \bar{u}/\bar{U}_0, \quad w = \bar{w}/\bar{W}_0,$$
$$t = \bar{t}\bar{W}_0/\bar{\lambda}, \quad p = \bar{p}\bar{h}_0/(\mu\bar{W}_0), \tag{2.1.1}$$

where $\bar{W}_0 = g\bar{h}_0^2\rho/\mu$ is the axial velocity scale, and $\bar{U}_0 = \epsilon\bar{W}_0$ is the radial velocity scale as determined by the continuity equation, yields

$$\epsilon^2 Re(u_t + uu_r + wu_z) = -p_r + \epsilon\left(\frac{1}{r}\partial_r(ru_r) + \epsilon^2 u_{zz} - \frac{u}{r^2}\right), \tag{2.1.2}$$

$$\epsilon Re(w_t + uw_r + ww_z) = -\epsilon p_z + \frac{1}{r}\partial_r(rw_r) + \epsilon^2 w_{zz} + 1, \tag{2.1.3}$$

$$\frac{1}{r}\partial_r(ru) + w_z = 0, \tag{2.1.4}$$

where $Re = \bar{W}_0\bar{h}_0\rho/\mu$ is the Reynolds number. Boundary conditions are enforced at the wall and the free surface: At the wall, $r = a$, no-slip is enforced

$$w = u = 0, \tag{2.1.5}$$

while at the free surface, $r = R(z,t)$, continuity of tangential stress,

$$(w_r + \epsilon^2 u_z)[1 - (\epsilon R_z)^2] + 2\epsilon^2(u_r - w_z)R_z = 0, \tag{2.1.6}$$

and continuity of normal stress according to the Young-Laplace equation,

$$-p^{(l)}(1 + (\epsilon R_z)^2) + 2\epsilon(u_r + w_z(\epsilon R_z)^2) + \epsilon R_z(w_r + \epsilon^2 u_z)$$
$$= \frac{1 + (\epsilon R_z)^2}{C}\left(\frac{1}{R(1 + (\epsilon R_z)^2)^{1/2}} - \frac{\epsilon^2 R_{zz}}{(1 + (\epsilon R_z)^2)^{3/2}}\right), \tag{2.1.7}$$

are both enforced. Here the background pressure, $p^{(g)}$, has been set to 0, and $C = \frac{\mu\bar{W}_0}{\gamma}$ is the capillary number. Note that the sign of the left-hand side of (2.1.7) is opposite that found in the case of an exterior coating [11]. The final boundary condition at the free surface is the kinematic boundary condition

$$u = R_t + wR_z. \tag{2.1.8}$$

The goal is to find a single decoupled PDE governing the evolution of the free surface. Integrating the continuity equation (5.4.4) across the fluid layer and then substituting (2.1.8) using the Leibniz integral rule gives

$$R_t = \frac{1}{R}\frac{\partial}{\partial z}\int_R^a wrdr. \tag{2.1.9}$$

If an approximate expression can be found for w, (2.1.9) becomes the model for the evolution of the free surface.

Assuming a regular perturbation expansion in ϵ for u, w, and p,

$$\begin{aligned} u &= u_0 + \epsilon u_1 + ..., \\ w &= w_0 + \epsilon w_1 + ..., \\ p &= p_0 + \epsilon p_1 + ..., \end{aligned} \tag{2.1.10}$$

substituting (2.1.10) into (5.4.2)-(2.1.7), and letting $\epsilon \to 0$, to leading order in ϵ the momentum equations become

$$0 = p_{0r}, \quad \frac{1}{r}\partial_r(rw_{0r}) = -1, \quad \frac{1}{r}\partial_r(ru_0) + w_{0z} = 0, \tag{2.1.11}$$

with boundary conditions at the wall

$$u_0 = w_0 = 0, \tag{2.1.12}$$

and at the interface

$$w_{0r} = 0, \quad p_0 = -\frac{1}{C}\left(\frac{1}{R} - \epsilon^2 R_{zz}\right). \tag{2.1.13}$$

The last term of (2.1.13) is $O(\epsilon^2)$; this term is retained in most thin-film and lubrication models of this type. The reasons given in the literature are quite varied; two particularly compelling reasons are briefly discussed here. The first is that as instabilities grow due to the second-to-last term in (2.1.13), the slope of the interface steepens and the contributions of the last term become significant. As linear stability analysis will show, this term is responsible for slowing instability growth. The second is that in a wide variety of contexts, retention of this term vastly

improves the agreement between such models and experiments. So despite the asymptotically inconsistent approach, this term is kept.

The solution to (2.1.11)-(2.1.13) is readily found to be

$$\begin{aligned} u_0 &= -RR_z\left[\frac{r}{2}\ln\left(\frac{r}{a}\right) - \frac{r}{4} + \frac{a^2}{4r}\right], \\ w_0 &= \frac{1}{4}(a^2 - r^2) + \frac{R^2}{2}\ln(r/a), \\ p_0 &= -\frac{1}{C}\left(\frac{1}{R} - \epsilon^2 R_{zz}\right). \end{aligned} \tag{2.1.14}$$

Note that the leading-order pressure is not dependent on r. The axial velocity w_0 is the exact solution (1.2.7); substituting w_0 into (2.1.9) gives the leading-order model

$$R_t = \frac{1}{2}[R^2 - a^2 - 2R^2\ln(R/a)]R_z. \tag{2.1.15}$$

2.2. First- and second-order corrections

The procedure for generating the next two successively refined approximations of w is now clear. Knowledge of w_i allows u_i to be found from the continuity equation and p_i from the radial momentum equation while enforcing the no-slip and normal-stress boundary conditions. The next-order axial momentum equation then allows w_{i+1} to be found in terms of u_i and p_i.

At $O(\epsilon)$, the momentum and continuity equations are

$$p_{1r} = \frac{1}{r}\partial_r(ru_{0r}) - u_0/r^2, \tag{2.2.1}$$

$$\frac{1}{r}\partial_r(rw_{1r}) = Re(w_{0t} + u_0 w_{0r} + w_0 w_{0z}) + p_{0z}, \tag{2.2.2}$$

$$\frac{1}{r}\partial_r(ru_1) + w_{1z} = 0. \tag{2.2.3}$$

Boundary conditions at the wall are

$$u_1 = w_1 = 0, \tag{2.2.4}$$

and at the interface the stress conditions become

$$w_{1r} = 0, \quad p_1 = 2u_{0r}. \tag{2.2.5}$$

The only term in the axial momentum equation (2.2.2) which needs to be estimated before w_1 can be calculated is w_{0t}. This term is approximated by taking the time derivative of (2.1.14) and using the leading-order model (2.1.15) to estimate R_t. The solution to (2.2.1)-(2.2.5) is

$$\begin{aligned}
u_1 &= \frac{1}{16CR^3r}\Bigg[2(a^2-r^2)^2R_z^2 + 4\bigg(a^2-r^2+2r^2\ln\frac{r}{a}\bigg)R^4R_zR_{zzz} \\
&\quad -R\bigg\{(a^2-r^2)^2 - 2\bigg(a^2-r^2+2r^2\ln\frac{r}{a}\bigg)R^2\bigg\}(R_{zz}+R^2R_{zzzz})\Bigg] \\
&\quad +g_{11}(r,R;a)R_z^2 + g_{12}(r,R;a)R_{zz}, \\
w_1 &= \frac{1}{4C}[r^2-a^2-2R^2\ln(r/a)]\bigg(\frac{R_z}{R^2}+R_{zzz}\bigg) + g_{21}(r,R;a)R_z, \\
p_1 &= \frac{1}{2R}\bigg(a^2-R^2-2R^2\ln\frac{r}{a}\bigg)R_z,
\end{aligned} \tag{2.2.6}$$

where each $g_{ij}(r,z,t)$ is

$$\begin{aligned}
g_{11} &= \frac{Re}{768r}\Bigg(-13a^6+33a^4r^2-21a^2r^4+r^6+12a^2r^4\ln\frac{r}{a} \\
&\quad +6R^2\bigg(-17a^4+48a^2r^2-31r^4+12a^2r^2\ln\frac{r}{a}+32r^4\ln\frac{r}{a}-12r^4\bigg(\ln\frac{r}{a}\bigg)^2 \\
&\quad +\ln R\bigg(-6a^4+6a^2r^2-12a^2r^2\ln\frac{r}{a}\bigg)-36a^4\ln\frac{R}{a}+60a^2r^2\ln\frac{R}{a}-30r^4\ln\frac{R}{a} \\
&\quad -24a^2r^2\ln\frac{r}{a}\ln\frac{R}{a}+24r^4\ln\frac{r}{a}\ln\frac{R}{a}+2a^2\ln a\bigg(3a^2+2r^2+6r^2\ln\frac{R}{a}\bigg) \\
&\quad +6a^2r^2\ln\frac{R}{r}-2a^2r^2\ln r\bigg(5+6\ln\frac{R}{r}\bigg)\bigg) \\
&\quad -6R^4\bigg(a^2-r^2+2r^2\ln\frac{r}{a}\bigg)\bigg(-19-4\ln\frac{R}{a}+40\bigg(\ln\frac{R}{a}\bigg)^2\bigg)\bigg),
\end{aligned} \tag{2.2.7}$$

$$
\begin{aligned}
g_{12} = \frac{Re}{768r} R\Bigg(& -13a^6 + 33a^4r^2 - 21a^2r^4 + r^6 + 12a^2r^4 \ln\frac{r}{a} \\
& -6R^2\Bigg(a^4 - 8a^2r^2 + 31r^4 - 8a^2r^2\ln\frac{r}{a} - 8r^4\ln\frac{r}{a} + 4r^4\Big(\ln\frac{r}{a}\Big)^2 \\
& + \ln R\Big(2a^4 - 2a^2r^2 + 4a^2r^2\ln\frac{r}{a}\Big) + 12a^4\ln\frac{R}{a} - 20a^2r^2\ln\frac{R}{a} + 10r^4\ln\frac{R}{a} \\
& + 8a^2r^2\ln\frac{r}{a}\ln\frac{R}{a} - 8r^4\ln\frac{r}{a}\ln\frac{R}{a} - 2a^2\ln a\Big(a^2 + 2r^2\ln\frac{R}{a}\Big) \\
& - 2a^2r^2\ln\frac{R}{r} + 2a^2r^2\ln r\Big(1 + 2\ln\frac{R}{r}\Big)\Big) \\
& - 6R^4\Big(a^2 - r^2 + 2r^2\ln\frac{r}{a}\Big)\Big(-3 - 4\ln\frac{R}{a} + 8\Big(\ln\frac{R}{a}\Big)^2\Big)\Big), \\
g_{21} = \frac{Re}{128}\Bigg[& R\Big(-11a^4 + 12a^2r^2 - r^4 - 8a^2r^2\ln\frac{r}{a}\Big) \\
& + R^3\Big(-20(a^2 - r^2) - 24r^2\ln\frac{r}{a} + 16r^2\Big(\ln\frac{r}{a}\Big)^2\Big) \\
& + a^2R^3\Big(-16\ln\frac{r}{a} - 8\ln a\ln\frac{R}{a} + 8\ln r\ln\frac{R}{r} + 8\ln R\ln\frac{r}{a}\Big) \\
& + R^3\ln\frac{R}{a}\Big(32(r^2 - a^2) + 16a^2\ln\frac{r}{a} - 32r^2\ln\frac{r}{a}\Big) \\
& - 12R^5\ln\frac{r}{a} - 16R^5\ln\frac{r}{a}\ln\frac{R}{a} + 32R^5\ln\frac{r}{a}\Big(\ln\frac{R}{a}\Big)^2\Bigg].
\end{aligned} \tag{2.2.8}
$$

The evolution equation for the free surface including the first-order axial velocity correction is

$$
R_t = \frac{1}{R}\partial_z\int_R^a (w_0 + \epsilon w_1) r dr, \tag{2.2.9}
$$

which, after returning to the original aspect ratio (hence removing ϵ), is

$$
R_t = f_1(R;a)R_z + \frac{1}{R}[Sf_2(R;a)(R_z + R^2R_{zzz}) + Ref_3(R;a)R_z]_z, \tag{2.2.10}
$$

where

$$
\begin{aligned}
f_1(R;a) &= \frac{1}{2}[R^2 - a^2 - 2R^2\ln(R/a)], \\
f_2(R;a) &= -\frac{a^4}{R^2} + 4a^2 - 3R^2 + 4R^2\ln\frac{R}{a}, \\
f_3(R;a) &= \Bigg[-\frac{59}{48}R^7 + \frac{15}{16}a^2R^5 + \frac{9}{16}a^4R^3 - \frac{13}{48}a^6R + \frac{17}{4}a^2R^5\ln(R/a) \\
&\quad -\frac{7}{4}a^4R^3\ln(R/a) + \frac{5}{2}R^7(\ln(R/a))^2 - \frac{5}{2}a^2R^5(\ln(R/a))^2 - 2R^7(\ln(R/a))^3\Bigg],
\end{aligned} \tag{2.2.11}
$$

and $S = 1/16C$.

In (2.2.10) the first term represents the leading-order balance between gravity and viscosity and is hyperbolic in nature. The terms with the S coefficient represent the effects of capillary forces and the last term represents inertial effects. The role which each of these terms plays will be explored in detail in later sections, but a cursory look at (2.2.10) shows that the first capillary term and inertial term promote instability growth while the second capillary term smooths instabilities.

In applications where inertial effects are significant, i.e. $Re = O(1)$ or higher, the inclusion of the last term is necessary (though this term fails to quantitatively capture experimental results at these Reynolds numbers and typically an integral model is used in such situations; see e.g. [72; 70] for further discussion). Here we are concerned with the case of a very viscous annular liquid; $Re = O(10^{-2})$ while $C = O(1)$ in most experiments considered here. Thus, with the exception of some limited discussion of the inertial effects in Section 2.4, we will henceforth consider the case when $Re \approx 0$ and ignore the term containing f_3:

$$R_t = f_1(R;a)R_z + \frac{1}{R}[Sf_2(R;a)(R_z + R^2R_{zzz})]_z. \tag{2.2.12}$$

Omission of the inertial terms means that w_0 was nowhere used in the calculation of w_1, i.e. the first two orders of the axial velocity profile are in some sense independent of each other; this idea will be exploited in Section 3.1 when deriving a model for the airflow problem.

The first-order model (2.2.10) is very similar to the LL model derived in [48], the only difference being that the LL model approximates the surface tension/curvature terms with their linear approximation; here the fully nonlinear terms are retained. We also correct one coefficient in $f_3(R;a)$, an apparent typo in [48]. The Stokes model (2.2.12) is identical to the CM model derived in [11] (and similar to that studied in [43]) up to (i) a choice of scalings and (ii) a sign change in front of $f_2(R;a)$ corresponding to the sign change in the normal stress boundary condition. Craster & Matar used their equation to study the flow of a viscous film coating the exterior of a tube, and their model was derived using small Bond number, an assumption not appropriate for all experiments considered here. It is perhaps not surprising then that their

model equation also performs well even at relatively high Bond numbers. Note that they study the equation for $R > a$ (exterior coatings) while here the case $R < a$ (interior coatings) is considered. Note also that these models make no assumption of small film thickness. The place of (2.2.12) in a hierarchy of models will be considered in Section 2.3.

At $O(\epsilon^2)$ the momentum and continuity equations are

$$p_{2r} = \frac{1}{r}\partial_r(ru_{1r}) - u_1/r^2 - Re(u_{0t} + u_0u_{0r} + w_0u_{0z}), \tag{2.2.13}$$

$$\frac{1}{r}\partial_r(rw_{2r}) = -w_{0zz} + p_{1z} + Re(w_{1t} + u_1w_{0r} + u_0w_{1r} + w_0w_{1z} + w_1w_{0z}), \tag{2.2.14}$$

$$0 = \frac{1}{r}\partial_r(ru_2) + w_{2z}. \tag{2.2.15}$$

As discussed in Section 2.2, inertial effects are likely not significant in the evolution of the free surface, and we thus approximate $Re \approx 0$ in the momentum equations. Even in studies of moderate Reynolds number flows the second-order inertial effects are often neglected as the complicated nonlinearities restrict the existence of solutions (see, e.g. [70]).

Boundary conditions at the wall are

$$u_2 = w_2 = 0; \tag{2.2.16}$$

at the interface the tangential stress boundary condition is

$$w_{2r} = -u_{0z} + w_{0r}R_z^2 + 2R_z(w_{0z} - u_{0r}). \tag{2.2.17}$$

As third-order corrections to the model will not be pursued here, we only present the second-order solution for the axial velocity:

$$\begin{aligned} w_2 = {} & \frac{1}{8R^2}\left(a^4 - a^2r^2 + 3R^2(r^2 - a^2) + 4r^2R^2\ln\frac{a}{r} + 36R^4\ln\frac{a}{r}\ln\frac{a}{R}\right)R_z^2 \\ & + \frac{1}{8R}\left(-a^4 + a^2r^2 + 3R^2(r^2 - a^2) + 4(r^2 + R^2)R^2\ln\frac{a}{r} + 12R^4\ln\frac{a}{r}\ln\frac{a}{R}\right)R_{zz}. \end{aligned} \tag{2.2.18}$$

The evolution of the free surface is then described by

$$R_t = \frac{1}{R}\partial_z\int_R^a (w_0 + \epsilon w_1 + \epsilon^2 w_2)r\,dr, \tag{2.2.19}$$

which, again after returning to the original aspect ratio (hence removing ϵ) and neglecting inertial terms, is

$$R_t = f_1(R;a)R_z + \frac{1}{R}[Sf_2(R;a)(R_z + R^2R_{zzz}) + f_4(R;a)R_z^2 + f_5(R;a)R_{zz}]_z, \tag{2.2.20}$$

where f_1 and f_2 are defined in (2.2.11) and

$$\begin{aligned} f_4(R;a) &= \frac{1}{32R^2}\left[a^6 - 4a^4R^2 + a^2R^4\left(7 - 36\ln\frac{R}{a}\right) + R^6\left(-4 + 40\ln\frac{R}{a} - 72\ln^2\frac{R}{a}\right)\right], \\ f_5(R;a) &= \frac{1}{32R}\left[-a^6 + a^2R^4\left(9 - 12\ln\frac{R}{a}\right) + R^6\left(-8 + 24\ln\frac{R}{a} - 24\ln^2\frac{R}{a}\right)\right]. \end{aligned} \tag{2.2.21}$$

The last two terms in (2.2.20) are often referred to as viscous dispersive terms, as they arise from the second-order viscous terms in the axial momentum equation and have a dispersive effect as will be shown in Section 2.4.

2.3. Thin-film limits

The long-wave model (2.2.12) was derived without assuming the film's thickness was small relative to the tube. If the film is taken to be thin, (2.2.12) can be simplified by letting

$$\eta = (a - R)/a; \tag{2.3.1}$$

$\eta \ll a$ represents the thickness of the annular film. Each of the functions f_i in (2.2.11) and (2.2.21) can be expanded about $\eta = 0$,

$$\begin{aligned} &f_1 = -a^2\eta^2 + O(\eta^4), \qquad f_2 = -\frac{16a^2}{3}\eta^3(1+\eta) + O(\eta^5), \\ &f_3 = -\frac{32a}{15}\eta^6 + O(\eta^7), \qquad f_4 = \frac{7a}{3}\eta^3 + O(\eta^4), \qquad f_5 = -a\eta^4 + O(\eta^5). \end{aligned} \tag{2.3.2}$$

If we neglect f_3, f_4, and f_5, we recover

$$\left(1 - \frac{\eta}{a}\right)\eta_t + \frac{1}{3}\frac{\partial}{\partial z}\left[\eta^3\left(1 - \frac{\eta}{a}\right)\left(1 + \frac{\tilde{S}_F\eta_z}{a^2(1-\eta/a)^2} + \tilde{S}_F\eta_{zzz}\right)\right] = 0, \tag{2.3.3}$$

where $\tilde{S}_F = 16S$, and which is an interior model analogous to the thin-film exterior model derived by Roy *et al.* [69]. (If f_4 and f_5 are not neglected, the appropriate second-order terms are found corresponding to the flat film models in [47]). As these authors pointed out in the exterior tube case, this model is still a conservation law for mass. If one assumes a very thin

film by letting $\eta/a \to 0$, then the model simplifies to the Frenkel model

$$\eta_t + \frac{1}{3}\frac{\partial}{\partial z}\left[\eta^3\left(1 + \frac{\tilde{S}_F\eta_z}{a^2} + \tilde{S}_F\eta_{zzz}\right)\right] = 0. \tag{2.3.4}$$

In dimensional form, this is

$$\bar{\eta}_{\bar{t}} + \frac{1}{3\bar{\mu}}\frac{\partial}{\partial \bar{z}}\left[\bar{\eta}^3\left(\bar{\rho}\bar{g} + \frac{\bar{\gamma}\bar{\eta}_{\bar{z}}}{\bar{a}^2} + \bar{\gamma}\bar{\eta}_{\bar{z}\bar{z}\bar{z}}\right)\right] = 0. \tag{2.3.5}$$

(In (2.3.4) the a^2 has been retained in the denominator of the azimuthal curvature term reflecting the scalings of the original Frenkel model; a change in axial scaling removes this factor and has been studied as such in [11].)

Note that in (2.3.5) as $\bar{a} \to \infty$, the mechanism for instability growth provided by the azimuthal curvature vanishes corresponding to the flat-film limit. Note that in (2.3.4), $a \to \infty$ only corresponds to the flat-film limit if the magnitude of $\bar{h}$ is fixed; if $\bar{a}$ is fixed and $\bar{h} \to 0$, then $a \to \infty$ corresponds to an arbitrarily thin film in a cylindrical tube, and the azimuthal curvature remains present as an instability growth mechanism. The thin-film model (2.3.4) was derived by Frenkel [18] and studied by Kerchman & Frenkel [39] and Kalliadasis & Chang [36]; we refer to it here as the Frenkel model. Note that this model does not conserve mass, as was pointed out in [69], but approximates the conservation of mass in the thin-film limit. Such an approximation can have surprising consequences which will be explored in Chapter 4.

The model specifies the film's mean thickness *a priori* while the flux varies as the solution evolves; in the experiments the volume flux is prescribed and the thickness varies as the experiment progresses. Thus, as with the exact solution in Section 1.2, the thickness and flux must be compared between the model and experiments. As described in Section 1.2 the experiments progressed until a quasi-steady state was reached and the film thickness was calculated by weighing the wetted tube. The model was solved numerically (see Section 2.5 for a discussion of the solution technique) with some film thickness and allowed to progress until a quasi-steady state was reached. If the flux (averaged over the domain) was higher (lower) than that of the experiments, the mean thickness was decreased (increased) and the simulation run again. By iterating this procedure a thickness was found corresponding to each experimental flux.

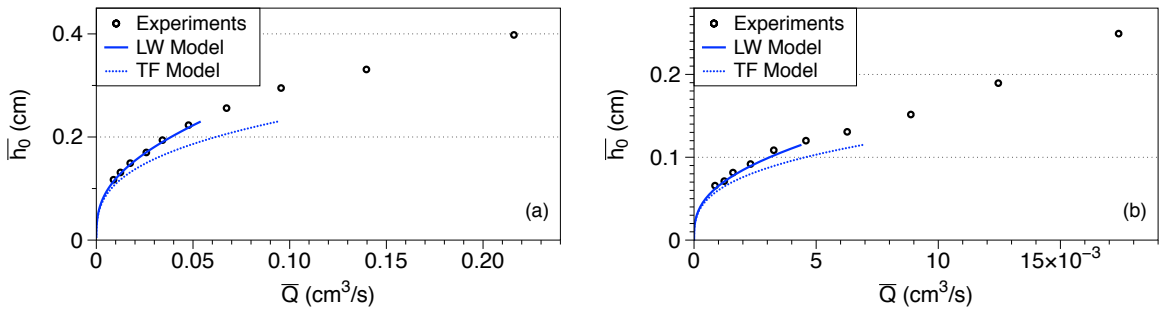

Figure 2.3.1: Comparison of volume flux and mean film thickness between long-wave model (2.2.12), thin-film model (2.3.4), and experiments for $\mu = 129$ P and (a) $\overline{a} = 0.5$ cm and (b) $\overline{a} = 0.295$ cm.

Figure 2.3.1 compares the flux-thickness dependence predicted by the model with that seen in the experiments. Excellent agreement is seen for $\bar{a} = 0.5$ cm and $\bar{a} = 0.295$ cm. Good agreement was also found for $\bar{a} = 0.17$ cm (not shown here). Discrepancies for this thinnest tube are likely due to errors in measuring the oil; while small, these errors are magnified as the tube radius decreases. Note that the model predictions cease to exist past some critical film thickness. For thick films, the model does not tend to a quasi-steady solution but experiences blow-up in finite time, thus there is no long-time flux limit to report. The tendency of the model to blow-up in finite time will be discussed in Section 2.5.

2.4. Linear stability analysis

Next, linear stability analysis is performed on the long-wave and thin-film models from two perspectives. First, temporal stability analysis is conducted, where the dispersion relations are studied with complex growth rates and real wavenumbers; second, spatial stability analysis is conducted, where the dispersion relations are studied with real growth rates and complex wavenumbers.

2.4.1. Temporal stability analysis. Linear temporal stability analysis is now conducted on the Frenkel model (2.3.4) and the long-wave models (2.2.12) and (2.2.20) by assuming that a flat interface is slightly perturbed, i.e.

$$R = (a - 1) + A \exp[i(kz - \omega t)], \tag{2.4.1}$$

where $A \ll a-1$ is the amplitude of the disturbance, k is its real wavenumber, $\mathrm{Re}[\omega]/k$ is its phase speed, and $\lambda = \mathrm{Im}[\omega]$ is its growth rate. Substituting (2.4.1) into (2.3.4), (2.2.12) and (2.2.20) and neglecting higher order terms in A gives the dispersion relation

$$\omega_F = k + iS_F\left(\frac{k^2}{a^2} - k^4\right), \tag{2.4.2}$$

$$\begin{aligned}\omega_1 = {} & \frac{1}{2}\left(a^2 - (a-1)^2 - 2(a-1)^2 \ln\frac{a}{a-1}\right)k \\ & + iS(a-1)^3\left[\left(\frac{a}{a-1}\right)^4 - 4\left(\frac{a}{a-1}\right)^2 + 3 + 4\ln\frac{a}{a-1}\right]\left[\frac{k^2}{(a-1)^2} - k^4\right],\end{aligned} \tag{2.4.3}$$

$$\begin{aligned}\omega_2 = {} & \frac{1}{2}\left(a^2 - (a-1)^2 - 2(a-1)^2 \ln\frac{a}{a-1}\right)k \\ & + \frac{k^3}{32}[-a^6 + a^2(9 + 12\ln a) - (8 + 24\ln a + 24\ln^2 a)] \\ & + iS(a-1)^3\left[\left(\frac{a}{a-1}\right)^4 - 4\left(\frac{a}{a-1}\right)^2 + 3 + 4\ln\frac{a}{a-1}\right]\left[\frac{k^2}{(a-1)^2} - k^4\right],\end{aligned} \tag{2.4.4}$$

where $S_F = \tilde{S}_F/3$. Note that the wavenumber of the instability that undergoes maximum growth in the Frenkel model is $k_m = 1/(a\sqrt{2})$, while in the long-wave models it is $k_m = 1/((a-1)\sqrt{2})$, i.e. in the Frenkel model the wavelength of maximum growth rate is determined by the tube radius, whereas in the long-wave models the average radius of the air-liquid interface plays the determining role. (In [11] the Frenkel model was rescaled in the axial direction by a/R, a choice asymptotically equivalent for large a to the aspect ratio studied here.)

The temporal growth rate for k_m for each model is

$$\lambda_F = \frac{S_F}{4a^4} \tag{2.4.5}$$

$$\lambda_{1,2} = \frac{S}{4(a-1)}\left[\left(\frac{a}{a-1}\right)^4 - 4\left(\frac{a}{a-1}\right)^2 + 3 + 4\ln\left(\frac{a}{a-1}\right)\right]. \tag{2.4.6}$$

Figure 2.4.1 shows the growth rate for the long-wave models (2.2.12) and (2.2.20), the Frenkel model (2.3.4), and that predicted by the full Stokes equations. The dispersion relation for the Stokes equations can be expressed in terms of Bessel functions (see, e.g., [11; 22] for details). As expected the growth rates of the long-wave models approach the Stokes equations asymptotically for small k. The maximum growth rate of the Frenkel model is significantly less than that of both the long-wave model and Stokes equations even for thin films (large a).

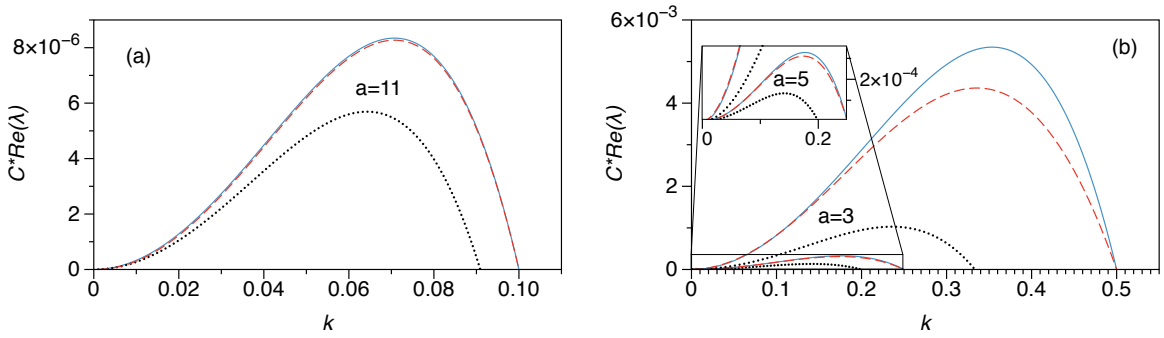

Figure 2.4.1: Non-dimensional growth rates $Re(\lambda)$ predicted by linear stability analysis of the long-wave models (solid lines), the Frenkel model (dotted lines), and the Stokes equations (dashed lines) as function of wavenumber k for three values of a.

Figure 2.4.2 shows the wavelength of maximum growth rate for $\bar{a} = 0.5$ cm. The Frenkel model selects a wavelength based on tube radius rather than mean film thickness, while the wavelength decreases with film thickness in the long-wave model and Stokes equations.

Figure 2.4.3 compares the linear disturbance speed in both long-wave models, the thin-film model, and the Stokes equations for various values of a. The first-order long-wave model has no dispersion, and the speed of a linear disturbance of any wavelength is exactly the speed of the Stokes equations in the limit $k \to 0$ as expected. The second-order long-wave model includes viscous dispersive effects, and this correction gives more accurate speed for the wavelength of maximum growth rate for moderately thin films. Note that the speed of a linear disturbance is always higher in the Frenkel model than in the long-wave models and Stokes equations.

2.4.2. Spatial stability analysis. The experiments reported here can be categorized by the location in the tube where the instabilities first visibly grow. For small film thicknesses, instability growth is first visible far away from the inlet, and the exact spatial location where instabilities are first visible varies significantly as the experiment progresses. For thicker films, instabilities are consistently visible very close to the inlet. Films which only exhibit visible instability growth far away from the inlet are said to be convectively unstable, while those which exhibit visible growth very near to the inlet are absolutely unstable (see [16; 15] for discussion of this in the case of an exterior coating). The film in Figure 1.2.4(a)-(c) is convectively unstable; the film in Figure 1.2.4(d) is absolutely unstable.

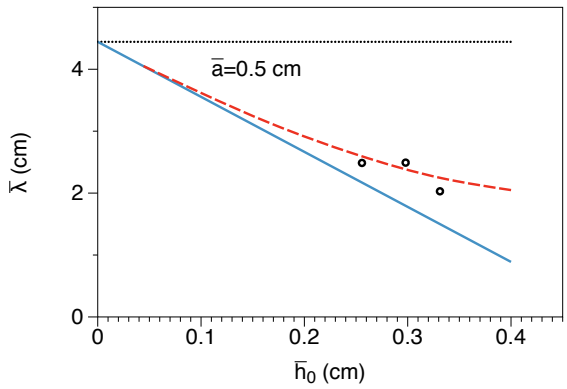

Figure 2.4.2: The wavelength of maximum growth rate predicted by linear stability analysis of the long-wave models (red solid lines), the Frenkel model (black dotted lines), and the Stokes equations (blue dashed lines) for $\bar{a} = 0.5$ cm.

Films which coat the exterior of a tube/fiber have been shown to be absolutely unstable for small enough tube radius and an intermediate film thickness; for tubes of large enough radius (as determined by the properties of the liquid), the exterior coating is always convectively unstable, regardless of the film thickness [16]. The same question is now explored for films coating the interior of a tube.

We examine the equations from the point of view of spatial instabilities, i.e. let ω be real and k be complex in the dispersion relations (2.4.2)-(2.4.3) in order to determine the regions of parameter space where the model predicts instabilities of each type (see [37] for the same initial approach with jets). Duprat found that there is a critical value S_{Fc} in the Frenkel model so that for $S_F > S_{Fc}$ the film is absolutely unstable, and for $S_F < S_{Fc}$ the film is convectively unstable [16]. This was done using the method described by Huerre & Monkewicz [28] where wavenumbers k_* with zero group velocity were found, i.e. $\frac{\partial \omega_F}{\partial k} = 0$, and their temporal growth rates $\omega(k_*)$ were evaluated. If $Im[\omega(k_*)] < 0$, the instabilities are convective, and if $Im[\omega(k_*)] > 0$, the instabilities are absolute. Since (2.4.2) is quartic in k, there are four solution branches; if the solution branches are plotted in complex k space, there is found to be a critical thickness at which two pinching points occur, i.e. two solution branches merge and pinch off creating a new topology [28] (see Figure 2.4.4). This thickness separates convectively unstable films from absolutely unstable ones.

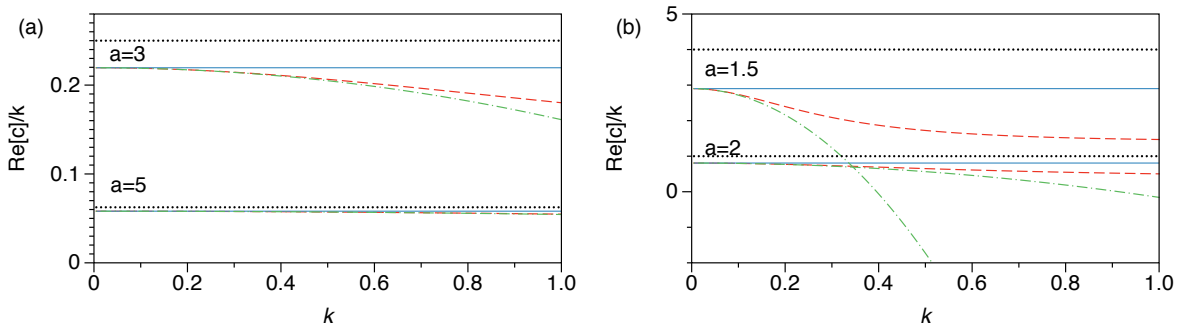

Figure 2.4.3: The speed of an infinitesimal disturbance predicted by linear stability analysis of the first-order long-wave model (solid lines), the second-order long-wave model (dot-dashed lines), the Frenkel model (dotted lines), and the Stokes equations (dashed lines) for four values of a.

The critical value is $S_{Fc} = \frac{a^3}{2}(-17 + 7\sqrt{7})^{1/2} \approx 0.617a^3$; this corresponds to the value β_{ca} found by Duprat etal where $S_{Fc} = a^3\beta_{ca}^{3/2}/3$ due to the choice of scalings. Recalling that $a = \bar{a}/\bar{h_0} = \bar{a}/(\bar{a} - \bar{R}_0)$, we find that the film is absolutely unstable if the following condition is met:

$$\bar{R}_0 < \bar{a} - \frac{3(-17 + 7\sqrt{7})^{1/2}\rho g\bar{a}^3}{2\gamma}. \tag{2.4.7}$$

As noted in [16], the first-order long-wave dispersion relation (2.4.3) can be found from the Frenkel dispersion relation (2.4.2) by the transformation

$$\omega = -\frac{a-1}{f_1(a-1;a)a}\omega', \quad k = \frac{a-1}{a}k', \quad S_F = \frac{a^3 f_2(a-1;a)}{(a-1)^2 f_1(a-1;a)}S'; \tag{2.4.8}$$

therefore the film is absolutely unstable in the long-wave model if the following condition is met:

$$\bar{R}_0^{-2}\frac{f_2(\frac{\bar{R}_0}{\bar{a}-\bar{R}_0};\frac{\bar{a}}{\bar{a}-\bar{R}_0})}{f_1(\frac{\bar{R}_0}{\bar{a}-\bar{R}_0};\frac{\bar{a}}{\bar{a}-\bar{R}_0})} > \frac{8\rho g(-17 + 7\sqrt{7})^{1/2}}{\gamma}. \tag{2.4.9}$$

Figure 2.4.5 shows the regions of absolute vs. convective instability for interior coatings as predicted by the Frenkel model and long-wave model compared with experimental results. The long-wave model shows excellent agreement with the experiments. The Frenkel model predicts that for tubes with radius greater than $\bar{a} \approx 0.11$ cm all films will be convectively unstable. (Note that this property of the Frenkel model to predict convective instabilities in a greater region of

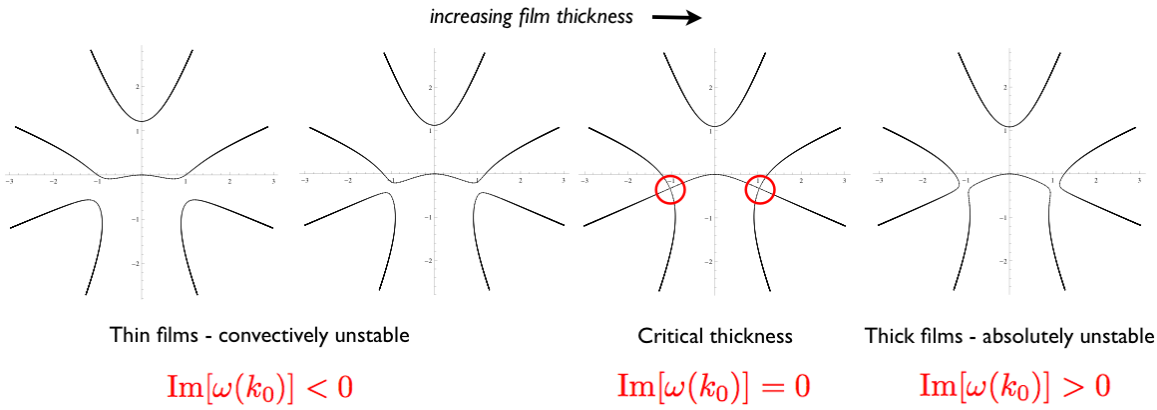

Figure 2.4.4: Solution branches for Frenkel model (2.3.4) in complex k space ($Re[k]$ varies along the horizontal axis; $Im[k]$ varies along the vertical axis). When the film thickness reaches a critical point there is a pinching of solution branches and a corresponding topological change. Films thicker than this critical thickness are absolutely unstable; see text for further discussion.

parameter space is consistent with the overestimate of the linear wave speed and underestimate of the maximum growth rate compared to the long-wave models and Stokes equations).

In [16] it was shown that the thin-film model predicts that if one only selects the film thickness large enough, absolute instabilities can be generated no matter the size of the tube; on the other hand, the long-wave CM model predicted a critical tube radius (as a function of liquid properties) beyond which instabilities could only be convective. This is just the opposite of the situation for interior coatings as just discussed, though in both cases the long-wave model accurately captures the stability of the film. Figure 2.4.5(b) shows these exterior coating results and are a rescaling of the results in Figure 4 in [16] to match the choice of scalings here.

2.5. Model solutions

We next solve the long-wave model (2.2.12) using the method of lines and a pseudospectral method (spatial derivatives are calculated in Fourier space and the nonlinearities are calculated in physical space). Time integration is done using a simple second-order predictor-corrector scheme. Throughout the simulations, the Fourier modes of the derivatives and nonlinear terms were carefully monitored to ensure conservation of volume. For initial conditions, we perturb the interface with multiple small-amplitude modes. See [4] and Section 4.1 for more details of the numerical procedure.

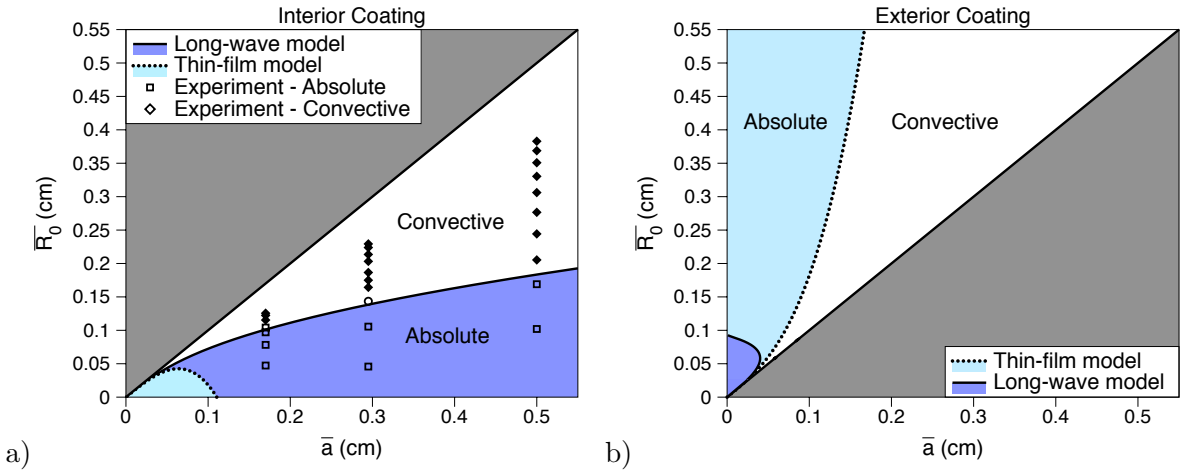

Figure 2.4.5: (a) Regions of absolute and convective instability for the long-wave model (solid lines) and the thin-film model (dotted lines). Shaded regions correspond to regions of absolute instability for the corresponding model. Liquid properties are $\gamma = 21.5$ dyn/cm and $\rho = 0.97$ g/cm^3 corresponding to experiments. (b) Same as (a) but for a film coating the exterior of the tube (identical to Figure 4 in [16] with different scaling).

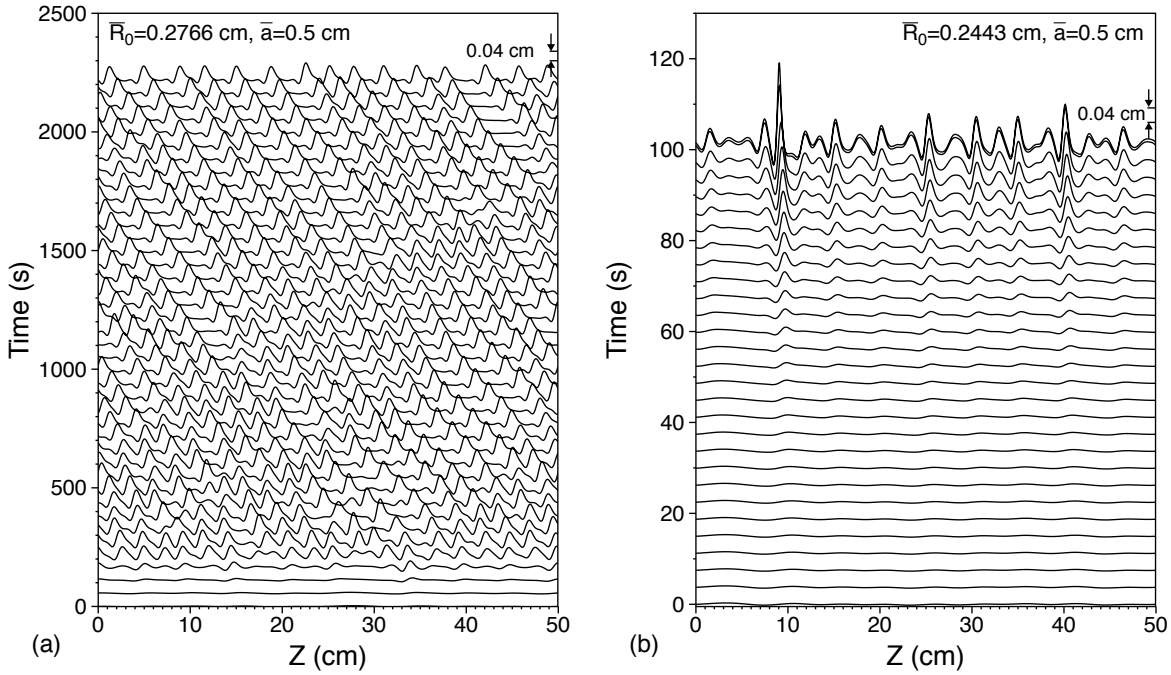

Figure 2.5.1: Time snapshots showing the evolution of solutions to equation (2.2.12) in a periodic domain. Interfacial profiles are shown successively shifted at time intervals Δt. Profiles are shown in the frame of reference moving with an undisturbed interface. (a) $\bar{R}_0 = 0.2813$ $\Delta t \approx 55$ s, (b) $\bar{R}_0 = 0.2642$, $\Delta_t \approx 3.75$ s.

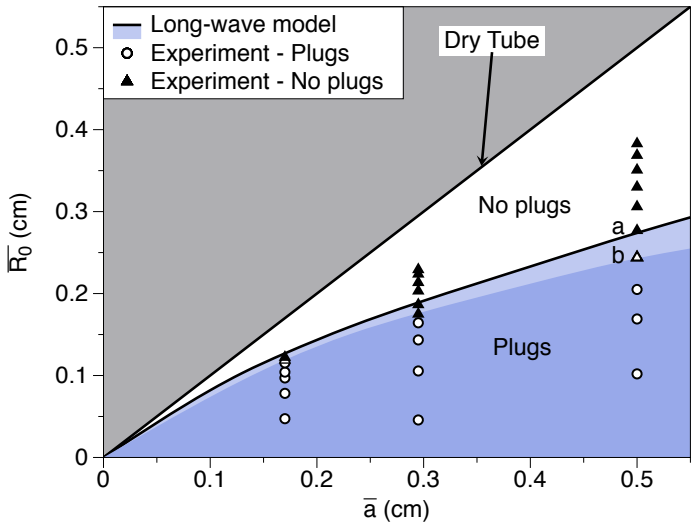

Figure 2.5.2: Shaded region shows combinations of mean interfacial thickness and tube radius which result in plug formation in the solutions to the long-wave model; experimental results are shown with diamonds (plugs form) and squares (no plugs). Points a and b correspond to the values used in Figure 2.5.1(a) and (b) respectively.

The solutions fall into one of two categories. For films with mean thickness smaller than some critical thickness depending on $\bar{a}$, i.e. $\bar{h}_0 < \bar{h}_c(\bar{a})$, the interface evolves into a series of small-amplitude waves. For thicker films with $\bar{h}_0 > \bar{h}_c(\bar{a})$, the solution suffers finite-time blow-up, a property which has been studied for models of flat films [66] and cylindrical thin films [31; 36]. Unlike with flat films and exterior coatings, finite-time blow-up is not inherently unphysical and is an indication of a tendency to form liquid plugs. Figure 2.5.1 shows an example of each situation using parameters corresponding to two of the experiments. Successive snapshots of the interface are shown; in Figure 2.5.1(a), the perturbed interface sees instability growth which saturates in small-amplitude waves. These waves undergo some limited nonlinear interaction before settling into a series of stable traveling waves. In Figure 2.5.1(b), the perturbed interface sees instability growth; the instability with largest amplitude undergoes rapid, accelerated growth, and eventually the solution blows up indicating the formation of a liquid plug.

Figure 2.5.2 shows which experiments and which model solutions resulted in the formation of liquid bridges or plugs. The lightly shaded region indicates a transition between the two regions where the model predicts that liquid bridges will form, but only after the instabilities

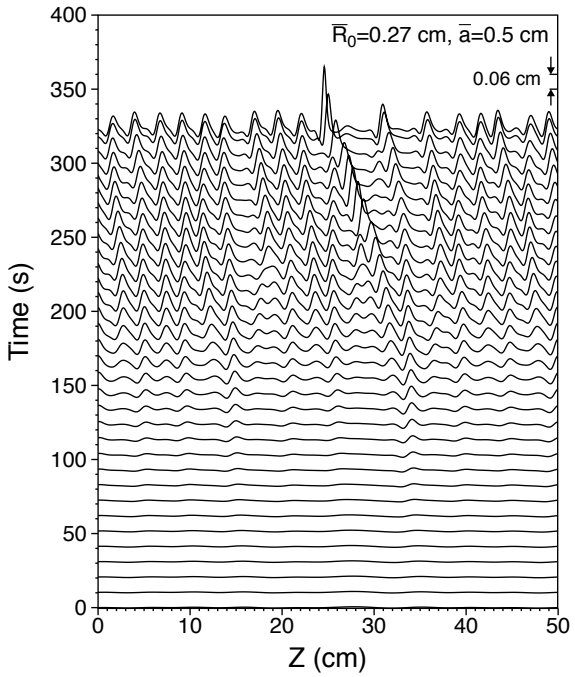

Figure 2.5.3: Same as Figure 2.5.1 but with $\bar{R}_0 = 0.27$ cm and $\Delta t \approx 10.3$ s.

have traversed a considerable distance. In the experiments, we are limited to observing bridge formation in the first 40 cm of distance traveled; it is quite possible that instabilities would form in the experiments if they had more room to grow and interact. In this transition region, the model solutions show that, unlike in Figure 2.5.1, bridge formation occurs as the result of nonlinear interactions between waves; see Figure 2.5.3 for an example with mean thickness between those found in Figure 2.5.1(a) and (b).

The experiments show that free surface instabilities form plugs at a somewhat constant location in the tube, i.e. their growth is spatial rather than temporal in nature. The model is solved using periodic boundary conditions since it is difficult to incorporate the experimental inlet/outlet boundary conditions directly into the model. In order to simulate the spatial growth of the instabilities, the model was solved again with periodic boundary conditions, this time on an extended domain ($\bar{L} = 150$ cm). The initial conditions were similar to those used in the previous section, but upstream from a chosen 'inlet point' the perturbed interface was damped exponentially by a factor corresponding to the growth rate of the fastest-growing wavelength. Thus for some period of time, the instabilities which reach the inlet point are

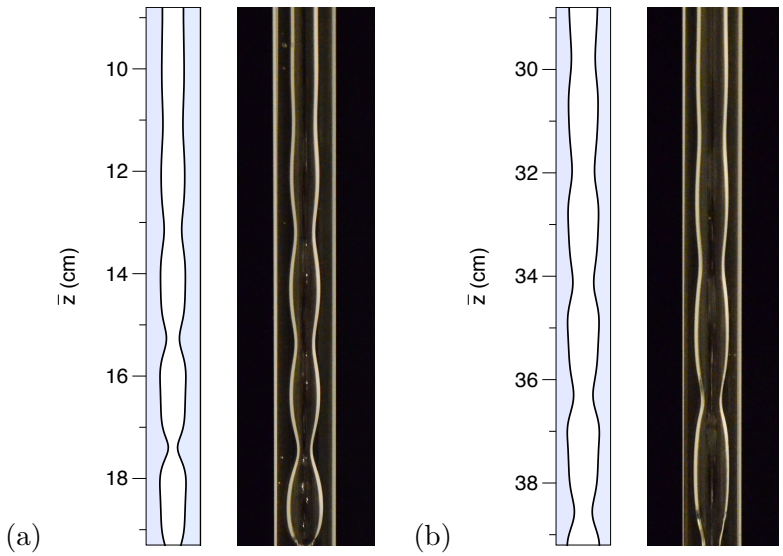

Figure 2.5.4: Model solutions (left) and experiments (right) for (a) $\bar{Q} = 9.56 \times 10^{-2}$ cm^3/s and(b) $\bar{Q} = 6.74 \times 10^{-2}$ cm^3/s. The initial condition for the model solution in (b) is shown in Figure 2.5.5(a).

of a consistent amplitude and provide some look at the spatial growth of the instabilities. Figure 2.5.4 compares solutions for two different thicknesses with corresponding experiments. Good qualitative agreement is found between the model and experiments, further suggesting the first-order model is capable of adequately describing the film flow.

2.6. Traveling wave solutions

The model solutions in which finite-time blow-up does not occur exhibit stable traveling waves. To study these waves, we switch to a frame of reference that travels with the wave, letting

$$Z = z - ct. \tag{2.6.1}$$

Substituting (2.6.1) into (2.2.12) yields a fourth-order ODE

$$R' = f_1(R;a)R' + \frac{S}{R}\frac{d}{dz}[f_2(R;a)(R' + R^2R''')]. \tag{2.6.2}$$

As (2.6.2) is not directly solvable, solutions are sought numerically in the following way. Equation (2.2.12) is solved as before and the solution is allowed to progress far enough in time so that the free surface settles to a steady series of traveling waves. One pulse of this solution

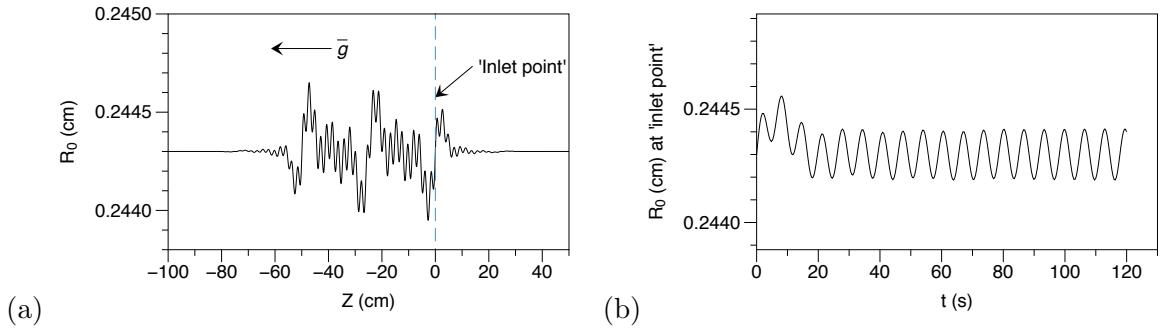

Figure 2.5.5: (a) Initial condition for model solutions shown in Figure 2.5.4(b). (b) The location of the interface at the 'inlet point' shown in (a) as a function of time.

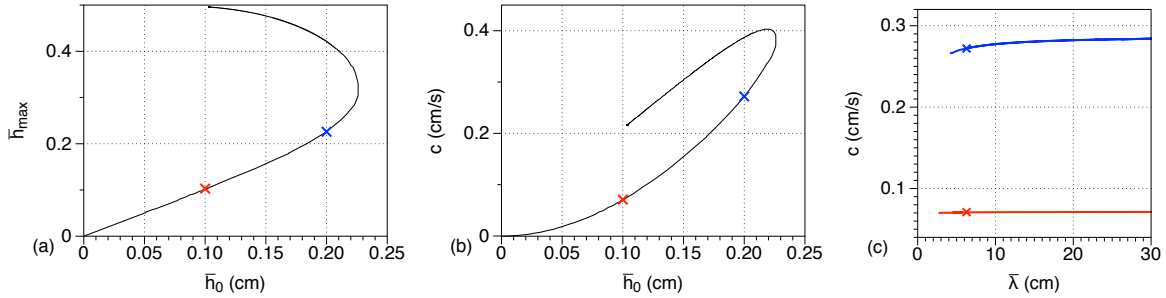

Figure 2.6.1: Properties of traveling wave solutions of the long-wave model (2.2.12) with experimental parameter values. (a) Maximum thickness as a function of mean thickness. (b) Speed as a function of mean thickness. (c) Speed as a function of domain length, using solutions shown in (a) and (b) with an 'x'.

with an appropriate domain length is used as an initial approximation and then refined by a collocation-method 2-point boundary value problem solver (the Matlab solver 'bvp4c').

For film flows down the exterior of a rigid cylinder, two primary classes of solitary waves are commonly reported in the literature: positive, or γ_1 waves where the crest is the dominant feature of the wave, and negative, or γ_2 waves where the trough is the dominant feature. As the waves observed in the experiments reported here are typically the γ_1 type, the following study is restricted to this class of waves. The continuation software AUTO07 is used to trace out solution branches and explore how the wave properties change as parameter values change [14].

One branch of solutions is shown in Figure 2.6.1 for $\mu = 129$ P and $\overline{a} = 0.5$ cm. Figure 2.6.1(a,b) shows that, for very thin films, the amplitude of the wave increases in an almost linear fashion while the speed increases approximately quadratically. As the thickness of the

film increases, the speed and amplitude begin to increase in a nonlinear way, until the film approaches the critical thickness, $\overline{h}_c \approx 0.227$ cm, at which point the branch of solutions continues to increase in amplitude and speed while decreasing in film thickness. Note that $\overline{h}_c$ is precisely the value $\overline{h}_c = \overline{a} - \overline{R}_0$ for $\overline{a} = 0.5$ cm which distinguishes plug formation from wavy interface as seen in Figure 2.5.2. Eventually the speed of the waves also decreases while the thickness at the crest approaches $\overline{a}$, approaching plug formation. Figure 2.6.1(c) shows that as the domain of the solutions increases, the speed of the waves approaches a constant speed c_∞.

As Figure 2.6.1(a,b) indicate, there are multiple γ_1 waves for the same set of experimental parameters and mean film thickness. In order to better understand how the fluid mass is flowing in each of these solutions, we reconstruct the stream function defined by the velocity field,

$$u = -\partial_z \Psi, \quad w - c = \frac{1}{r}\partial_r(r\Psi), \tag{2.6.3}$$

where in the first-order model, $w = w_0 + \epsilon w_1$, $u = u_0 + \epsilon u_1$. Integrating (2.6.3) gives

$$\begin{aligned}\Psi = &\left[-\frac{1}{4} + \frac{4S}{R^2}(R_z + R^2 R_{zzz})\right]\left[\frac{1}{4r}(a^2 - r^2)^2\right] \\ &+\left[\frac{R^2}{2} - 8S(R_z + R^2 R_{zzz})\right]\left[\frac{1}{4r}\{a^2 - r^2 + 2r^2\ln(r/a)\}\right].\end{aligned} \tag{2.6.4}$$

We then plot isolines of the stream function Ψ. Figure 2.6.2 shows streamlines for two of these solutions which have identical mean thickness. In Figure 2.6.2(b) a small region of closed streamlines near the wavecrest exists, indicating the presence of a recirculation zone, or trapped core of fluid which rolls over the rest of the substrate layer; in Figure 2.6.2(c) no such trapped core exists. Both of these solutions were used as initial conditions for (2.2.12) to verify that they are stable solutions; both retained their shape as they travel, though how sensitive these high-amplitude solutions are to perturbations was not extensively explored.

On a branch of traveling wave solutions such as Figure 2.6.1(a) there is one wave with amplitude $\bar{h}_{mc}$ that represents a streamline bifurcation. For waves with $\bar{h}_{max} < \bar{h}_{mc}$ only open streamlines exist. The wave with amplitude $\bar{h}_{mc}$ has one fixed point on the interface near the crest of the wave when viewed in a frame of reference traveling with the wave, i.e. the fluid velocity matches the wave velocity at exactly one point on the free surface. For

waves with $\bar{h}_{max} > \bar{h}_{mc}$ there are three fixed points: one elliptic point at the center of a recirculation zone in the fluid, and two hyperbolic points on the free surface that are endpoints of a separatrix between the recirculation zone and the underlying fluid layer. Recirculation zones were also found in the traveling reference frame in the integral model developed by Ruyer-Quil & Kalliadasis [70]; Malamataris & Balakotaiah studied numerical solutions to the full 2D Navier-Stokes equations and found analogous recirculation zones along the wall in the lab reference frame [52]. The significance of the recirculation zone in the traveling wave solutions will be explored further in Chapter 5.

For some parameter values this bifurcation point lies on the upper portion of the solution branch as depicted in Figure 2.6.1(a), while for others it lies on the lower portion. Thus two traveling wave solutions for the same parameters and film thickness may both have open streamlines, both have recirculation zones, or be one of each type. Figure 2.6.3 shows the type of traveling wave solutions that exist in $\bar{R}_0$-S parameter space. (As $\bar{R}_0 \to \bar{a} = 0.5$ cm, i.e. the thin-film limit, we find the lower-amplitude traveling wave solution converges to the corresponding traveling wave solution to the Frenkel equation; it has been checked that the streamline bifurcation in the Frenkel solutions occurs at $S \approx 1$ as Figure 2.6.3 suggests.)

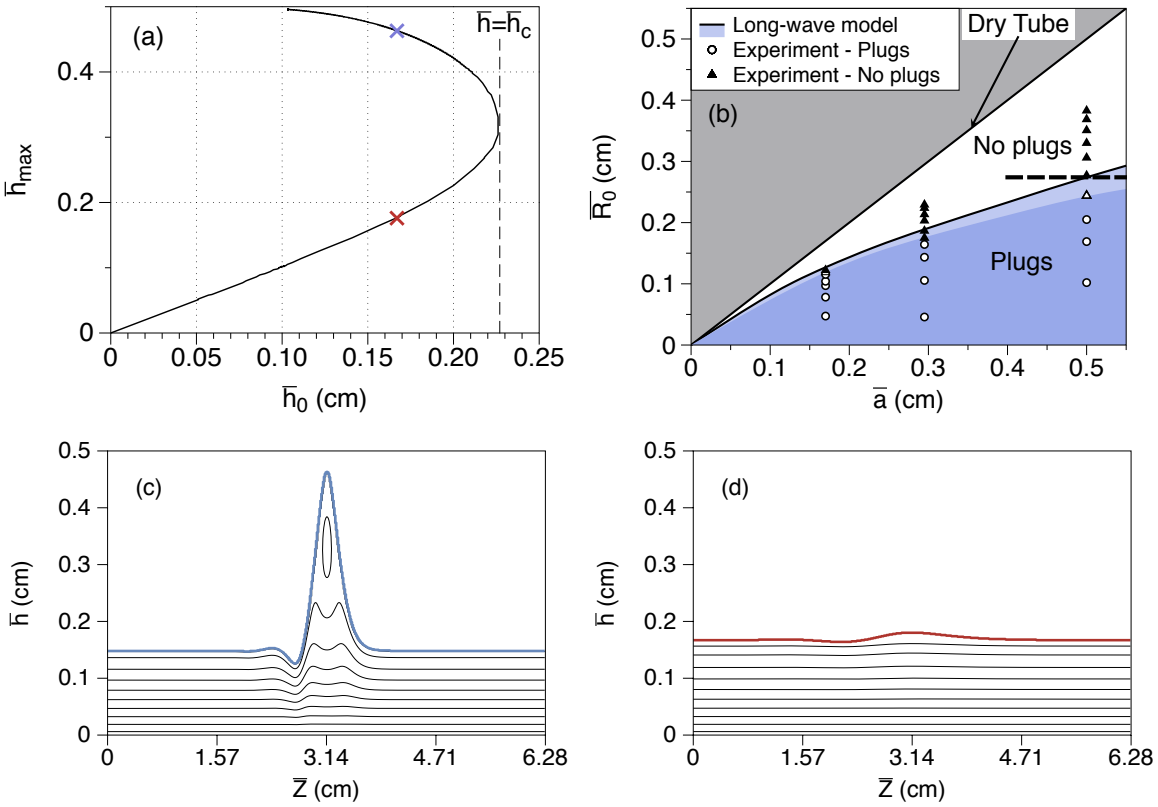

Figure 2.6.2: Traveling wave solutions for experimental parameter values. (a) Same as Figure 2.6.1(a); each 'x' corresponds to solutions with identical mean thickness. (b) Same as Figure 2.5.2; dashed line in (a) and (b) show existence bounds for TW solutions. (c) and (d) show streamlines plotted in a frame of reference moving with the wave. In (c), the closed streamlines indicate the presence of a trapped core; (d) contains only open streamlines.

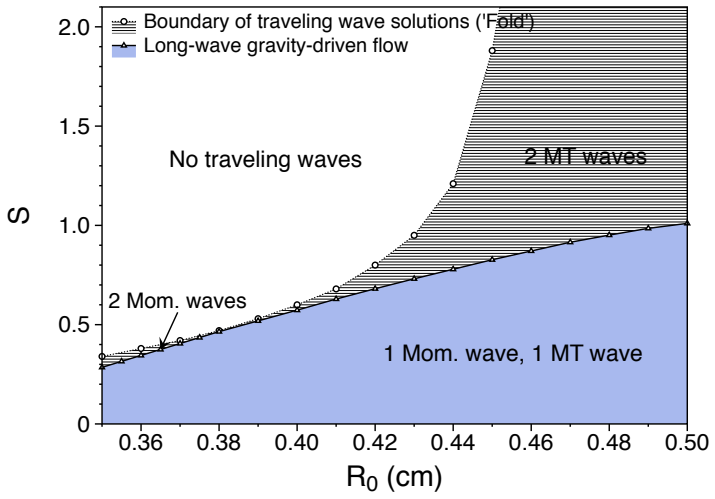

Figure 2.6.3: Plot of S-$\bar{R}_0$ parameter space for the long-wave model (2.2.12). Traveling wave solutions do not exist in white region. Two solutions, in some combination of mass transport and shear-enhancing waves, exist elsewhere.

CHAPTER 3

Air-driven film flow

In the previous chapter the flow of a fluid film falling down a tube driven by a balance of gravity, viscous, and capillary forces was studied. When the air in the core region of the tube is forced to flow due to an imposed pressure gradient the fluid film experiences stress at the free surface. Through this additional stress the air imparts some of its momentum to the fluid. If air is flowing down the tube, this additional stress causes the film to speed up; if the air is flowing up the tube, the film's downward flow is retarded and, if the airflow is strong enough, the film can reverse direction and travel up the tube. It is this latter case that is of interest here, i.e. we are interested in modeling axisymmetric disturbances in a two-phase vertical pressure-driven core-annular flow with the (much) more viscous fluid in the annulus. This case is of particular interest as the high contrast in viscosity between the air and liquid film makes direct numerical simulations difficult.

As mentioned in Section 1.3, the stability of core-annular flows has been well characterized (see, e.g. [25; 34; 33; 21; 35]). It should be mentioned that oil recovery has motivated much study of core-annular flow where both fluids have equal or similar density. Weakly nonlinear studies have been performed by Frenkel and Papageorgiou, Maldarelli & Rumschitzki who used Kuramoto-Sivashinsky-like equations to model small perturbations to a thin film and show the stabilizing effect of the primary flow preventing free surface rupture [19; 64]. Kerchman derived a thin-film model for equal densities and numerically studied the nonlinear behavior of its solutions [38]. Kouris & Tsamopoulos [44; 45] numerically studied the oil-water problem and compared their results favorably with experiments [1]. The specific case of pressure-driven flow with air as the core fluid has been studied experimentally by Clarke *et al.* [10] and Kim *et al.* [40; 41; 42] who studied the mean thickness and flow rates of an air-driven liquid film, and by Mouza *et al.* [56; 57] who studied air-driven annular flow of water and kerosene. The

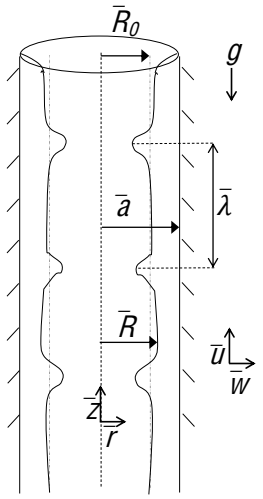

Figure 3.1.1: Definition sketch of the flow variables.

experiments by Kim *et al.*were reproduced in [4] for closer study of the axisymmetric instabilities they reported and the mechanisms of liquid transport. A comparison of long-wave modeling with the Kim experiments was also conducted by Camassa & Lee [5]; their model was updated [4] to include the effects of gravity due to the density difference between air and oil.

The model in [4] is derived in more detail in Section 3.1 and various thin-film models are recovered in the appropriate limits in Section 3.2. Linear stability analysis is performed in Section 3.3. A comparison with experiments is postponed until Section 5.1.

3.1. Locally Poiseuille airflow modeling

As our primary motivation is flow with a gas core and liquid annulus, we refer to the core variables with the superscript (g) and the annular variables with the superscript (l) throughout. The governing equations for the flow of both the gas and the liquid are the incompressible axisymmetric Navier-Stokes equations in cylindrical coordinates (1.3.1). As we will primarily be interested in the case where the film flows up the tube, the coordinate system is here oriented so that $\bar{z}$ increases moving up the tube, see Figure 3.1.1.

To non-dimensionalize (1.3.1), a typical wavelength $\bar{\lambda}$ is used as the axial lengthscale, and the mean radius of the gas core $\bar{R}_0 = \sqrt{\overline{R_0^2}}$ serves as the radial lengthscale (where $\overline{R_0^2}$ is the mean cross-sectional area of the gas core and is specified *a priori*). If $\epsilon = \bar{R}_0/\bar{\lambda} \ll 1$ the distortions to

the air-liquid interface are considered long-wave. Other scales are set by the gas core laminar axial velocity along the centerline $\bar{W}_0$ and a radial velocity $\bar{U}_0$. In the experiments reported here and in [4], the airflow is driven at a constant volume flux $\bar{Q}^{(g)}$ rather than by a constant pressure gradient in the core, and so we set $\bar{W}_0 = 2\bar{Q}^{(g)}/(\pi\bar{R}_0^2)$. The continuity equation requires that $\bar{U}_0 = \epsilon\bar{W}_0$. We then nondimensionalize (1.3.1) with the following variables:

$$r = \bar{r}/\bar{R}_0, \quad z = \bar{z}/\bar{\lambda}, \quad u = \bar{u}/\bar{U}_0, \quad w = \bar{w}/\bar{W}_0,$$

$$t = \bar{t}\bar{W}_0/\bar{\lambda}, \quad p = \epsilon\bar{p}\bar{R}_0/(\bar{\mu}^{(l)}\bar{W}_0), \quad \tau = \bar{\tau}\bar{R}_0/(\bar{\mu}^{(l)}\bar{W}_0), \tag{3.1.1}$$

where t is the dimensionless time, τ is the dimensionless tangential stress, and p is the dimensionless pressure. Substituting (3.1.1) into (1.3.1) the momentum and continuity equations for the liquid become:

$$\epsilon^3 Re^{(l)}(u_t + uu_r + wu_z) = -p_r + \epsilon^2\left(\frac{1}{r}\partial_r(ru_r) + \epsilon^2 u_{zz} - \frac{u}{r^2}\right), \tag{3.1.2}$$

$$\epsilon Re^{(l)}(w_t + uw_r + ww_z) = -p_z + \frac{1}{r}\partial_r(rw_r) + \epsilon^2 w_{zz} - \frac{Re}{Fr^2}, \tag{3.1.3}$$

$$\frac{1}{r}\partial_r(ru) + w_z = 0, \tag{3.1.4}$$

where $Re^{(l)} \equiv \bar{\rho}^{(l)}\bar{W}_0\bar{R}_0/\bar{\mu}^{(l)}$ is the liquid Reynolds number and $Fr \equiv \bar{W}_0/\sqrt{\bar{g}\bar{R}_0}$ is the Froude number. The boundary conditions at the inner wall of the pipe are no-slip,

$$w(a) = 0, \quad u(a) = 0. \tag{3.1.5}$$

As with gravity-driven flow, we assume that the surface tension of the liquid is constant, neglecting any variation in z. There are then three boundary conditions at the free surface, $r = R(z,t)$: (i) continuity of tangential stress

$$(w_r + \epsilon u_z)[1 - (\epsilon R_z)^2] + 2\epsilon^2(u_r - w_z) = \tau^{(g)}[1 + (\epsilon R_z)^2], \tag{3.1.6}$$

where $\tau^{(g)}$ is the dimensionless tangential stress of gas, (ii) jump of normal component of stress due to the free surface curvature, which is given by Laplace's formula

$$\begin{aligned}(-p^{(l)} + p^{(g)})(1 + (\epsilon R_z)^2) + 2\epsilon^2(u_r + w_z(\epsilon R_z)^2) + \epsilon^2(w_r + \epsilon u_z)R_z \\ = \left[-p^{(g)} + \epsilon C^{-1}\left(\frac{1}{R(1 + (\epsilon R_z)^2)^{1/2}} - \frac{\epsilon^2 R_{zz}}{(1 + (\epsilon R_z)^2)^{3/2}}\right)\right](1 + (\epsilon R_z)^2),\end{aligned} \tag{3.1.7}$$

where $p^{(g)}$ is the dimensionless normal stress of gas, and $C = \bar{W}_0\bar{\mu}^{(l)}/\bar{\gamma}$ is the capillary number, and (iii), the kinematic condition

$$u = R_t + wR_z. \tag{3.1.8}$$

The airflow's presence is felt by the liquid through the first two free surface boundary conditions; note that the right-hand side of (3.1.6) is nonzero, and we no longer set $p^{(g)}$ equal to zero in (3.1.7) (compare to (2.1.6) and (2.1.7)).

As in gravity-driven flow, integrating the continuity equation (3.1.4) across the annulus and using (3.1.8) with Leibniz's integral rule yields the layer-mean equation

$$R_t - \frac{1}{R}\frac{\partial}{\partial z}\int_R^a wr dr = 0, \tag{3.1.9}$$

for the location of the free surface. Once again we seek an approximate solution for w so that the system can be closed and reduced to a single evolution equation for the interface location. This will require obtaining approximate expressions for our two new unknowns, $p_z^{(g)}$ and $\tau^{(g)}$.

The leading order approximation of w can be obtained by taking the limit $\epsilon \to 0$ in the equations above. For fixed mean radius $\bar{R}_0$, the liquid has fixed Reynolds number and hence $\epsilon Re^{(l)} \to 0$. While the higher-order terms vanish in the system of equations, it is again essential to retain the surface tension terms at the leading order, for which one term is of $O(\epsilon)$, and the other is of $O(\epsilon^3)$.

At leading order in ϵ, the momentum and continuity equations become

$$0 = p_r, \tag{3.1.10}$$

$$\frac{1}{r}\partial(rw_r) = p_z + \frac{Re^{(l)}}{Fr^2}, \tag{3.1.11}$$

$$R_t - \frac{1}{R}\frac{\partial}{\partial z}\int_R^a wrdr = 0. \tag{3.1.12}$$

The boundary condition at the wall $r = a$ is

$$w = 0. \tag{3.1.13}$$

At the interface $r = R$ we have

$$w_r = \tau^{(g)}, \tag{3.1.14}$$

$$-p^{(l)} = -p^{(g)} + \frac{\epsilon}{C^{-1}}(R^{-1} - \epsilon^2 R_{zz}). \tag{3.1.15}$$

Returning the problem to the original aspect ratio allows (3.1.15) to be written as

$$-p^{(l)} = -p^{(g)} + \frac{1}{C}(R^{-1} - R_{zz}). \tag{3.1.16}$$

This boundary value problem (3.1.10)-(3.1.14) and (3.1.16) has a solution of the form

$$w(r) = \frac{1}{4}\left(p_z^{(l)} + \frac{Re^{(l)}}{Fr^2}\right)(r^2 - a^2) + \left[R\tau^{(g)} - \frac{R^2}{2}\left(p_z^{(l)} + \frac{Re^{(l)}}{Fr^2}\right)\right]\ln\left(\frac{r}{a}\right), \tag{3.1.17}$$

where $p_z^{(g)}$ and $\tau^{(g)}$ are still to be determined.

To estimate these terms, we model the gas flow using a zero equation turbulence closure as found in [81]. The mean airflow can be computed using a locally-Poiseuille solution, so that the Poiseuille solution is modulated to take into account the slow variation in z of the free surface. This is an admittedly rather unsophisticated approach, and more refined turbulence closure models could certainly be used (another approach will also be considered in Chapter 5). The solution w for Poiseuille flow is of the form

$$w^{(g)}(r) = \frac{m}{4}\left(p_z + \frac{\rho^{(g)}Re^{(l)}}{\rho^{(l)}Fr^2}\right)r^2 + C(z), \tag{3.1.18}$$

where the ratio of viscosities is

$$m = \frac{\mu^{(l)}}{\mu^{(g)}}. \tag{3.1.19}$$

In order to determine the value of the constant of integration $C(z)$ a free surface boundary condition is needed. Since the dynamic viscosity ratio of the liquid to gas is $m = O(10^6)$, the velocity of the gas at the free surface is assumed to be $O(\epsilon)$ or smaller, and so a no-slip boundary condition is enforced at the free surface which the air essentially sees as a rigid wall. The mean axial component of the gas velocity is then

$$w^{(g)}(r) = \frac{m}{4}\left(p_z^{(g)} + \frac{\rho^{(g)} Re^{(l)}}{\rho^{(l)} Fr^2}\right)(r^2 - R^2). \tag{3.1.20}$$

With this velocity, the fixed gas flux can be written as

$$\begin{aligned} Q^{(g)} = \frac{\pi}{2} &= \int_0^{R(z)} 2\pi r w^{(g)} dr \\ &= -\frac{\pi m}{8}\left(p_z^{(g)} + \frac{\bar{\rho}^{(g)} Re^{(l)}}{\bar{\rho}^{(l)} Fr^2}\right) R(z)^4. \end{aligned} \tag{3.1.21}$$

The z-component of the gas pressure gradient can be expressed in terms of the flux:

$$p_z^{(g)} = -\frac{4}{mR(z)^4} - \frac{\bar{\rho}^{(g)} Re^{(l)}}{\bar{\rho}^{(l)} Fr^2}. \tag{3.1.22}$$

Similarly, the tangential stress at the free surface is

$$\begin{aligned} \tau^{(g)}(z) &= \mu^{(g)} w_r^{(g)}|_{r=R(z)} \\ &= -\frac{2}{mR(z)^3}. \end{aligned} \tag{3.1.23}$$

Substituting these terms (3.1.22) and (3.1.23) into (3.1.17) gives an approximate expression for w:

$$\begin{aligned} w = &\left[-\frac{1}{mR^4} + (l-1)\frac{Re^{(l)}}{4lFr^2} + \frac{1}{4C}\left(\frac{R_z}{R^2} + R_{zzz}\right)\right](r^2 - a^2) \\ &-\left(\frac{R^2(l-1)Re^{(l)}}{2lFr^2} + \frac{1}{2C}(R_z + R^2 R_{zzz})\right)\ln\left(\frac{r}{a}\right). \end{aligned} \tag{3.1.24}$$

Substituting (3.1.24) into (3.1.9) yields the nondimensional evolution equation studied in [4]:

$$R_t + [S_1 f_1(R;a) + S_2(a) f_2(R;a)]R_z + \frac{S_3(a)}{R}[f_3(R;a)(R_z + R^2 R_{zzz})]_z = 0, \tag{3.1.25}$$

where the f_i are given by

$$\begin{aligned} f_1(R;a) &= \frac{a^2}{R^4}\left(\frac{a^2}{R^2}-1\right), \\ f_2(R;a) &= R^2 - a^2 + 2R^2\ln\left(\frac{a}{R}\right), \\ f_3(R;a) &= \frac{a^4}{R^2} - 4a^2 + 3R^2 + 4R^2\ln\left(\frac{a}{R}\right), \end{aligned} \tag{3.1.26}$$

and the S_i by

$$S_1 = \frac{1}{m}, \qquad S_2(a) = \frac{(\rho^{(l)}-\rho^{(g)})Re^{(l)}}{2\rho^{(l)}Fr^2}, \qquad S_3(a) = \frac{1}{16C}. \tag{3.1.27}$$

S_2 and S_3 depend on a, the ratio of tube radius to mean radius of the core; S_1 does not depend on a. Note that like (2.2.12), (3.1.25) does not depend on the thickness of the annulus being small; the full cylindrical geometry of the problem is retained in the highly nonlinear functions f_i. The significance of retaining the cylindrical geometry will be studied in Chapter 4.

While the airflow has been modeled above as laminar flow, we estimate that the airflow is at high enough Reynolds number to be fully turbulent in all our experiments; in most experiments, $4\times10^3 < Re < 1.2\times10^4$. As a crude way to capture the effects of the turbulence on the stress at the free surface, the viscosity is replaced with an effective viscosity in the model. This effective viscosity is based on the Blasius formula and is

$$\mu(g)_{eff} = 0.0791\frac{(Re^{(g)})^{3/4}\mu^{(g)}}{16}. \tag{3.1.28}$$

Unless otherwise noted, this effective air viscosity is used in calculations in the following sections.

Equation (3.1.25) can be rescaled in time by the speed of an infinitesimal disturbance ($t' = S_1 f_1(1;a) = t(a^4-a^2)/m$, dropping primes from here) to give

$$R_t + \left[\frac{f_1(R;a)}{f_1(1;a)} + \frac{f_2(R;a)}{f_2(1;a)}F(a)\right]R_z + \frac{S(a)}{R}[f_3(R;a)(R_z + R^2R_{zzz})]_z = 0, \tag{3.1.29}$$

where

$$\begin{aligned} F &= -\frac{S_2 f_2(1;a)}{S_1 f_1(1;a)} = \frac{\pi g(\rho^{(l)}-\rho^{(g)})}{4\bar{Q}^{(g)}\mu^{(g)}}\frac{(a^2-1-2\ln a)}{(a^4-a^2)}\bar{R}_0^4, \\ S &= \frac{S_3}{S_1 f_1(1;a)} = \frac{\pi\gamma}{32\bar{Q}^{(g)}\mu^{(g)}(a^4-a^2)}\bar{R}_0^2. \end{aligned} \tag{3.1.30}$$

The flow dynamics are now seen to be completely determined by three parameters: S, a surface tension/airflow ratio; F, a gravity/airflow ratio; and a, the film thickness parameter. Both S and F are dependent on the radius of the gas core. Roughly speaking, for small values of S, when $F < 1$, we expect disturbances to travel up the tube, i.e. the pressure gradient dominates gravity; when $F > 1$, we expect disturbances to flow down the tube, i.e. the pressure gradient is not strong enough to overcome the effects of gravity. In the case of equal densities, i.e. $F = 0$, (3.1.25) reduces to the model equation derived in [5] up to a choice of scalings.

Note that for small-amplitude waves the two hyperbolic terms will roughly cancel one another if the gas flow rate/viscosity are set to an appropriate value. This cancellation implies that small-amplitude waves would be motionless, i.e. the stress from the upward airflow exactly cancels the downward pull of gravity. This balance does not guarantee a mean flux of zero, only that the waves would appear to remain at the same point in the tube. The gas viscosity needed to balance the gravity term is dependent on the mean thickness of the gas core; for very thin films, the airflow asymptotically dominates the gravity terms, and a small viscosity will suffice to balance the terms.

Next it will be shown that (3.1.25) reduces to various thin-film models from the literature in the appropriate limits.

3.2. Thin-film limits

3.2.1. Pressure-driven flow. If the annular film is thin, equation (3.1.25) can be further simplified by letting

$$\eta = 1 - \frac{R}{a}; \tag{3.2.1}$$

$\eta \ll 1$ represents the thickness of the thin annular film. Each of the functions $f_i(R; a)$ in (3.1.26) can be expanded about $\eta = 0$:

$$f_1(\eta) = \left(\frac{2}{a^2}\right)\eta + \left(\frac{11}{a^2}\right)\eta^2 + \left(\frac{36}{a^2}\right)\eta^3 + O(\eta^4), \tag{3.2.2}$$

$$f_2(\eta) = (-2a^2)\eta^2 + \left(\frac{2a^2}{3}\right)\eta^3 + O(\eta^4), \tag{3.2.3}$$

$$f_3(\eta) = \left(\frac{16a^2}{3}\right)\eta^3 + O(\eta^4). \tag{3.2.4}$$

Notice the gravity term f_2 vanishes at leading order; the effects of tangential stress at the interface dominate the effects of gravity in the thin-film limit. Retaining the leading-order of f_2 and, as before, retaining $f_3 = O(\eta^3)$ to keep the effects of surface tension and substituting (3.2.1)-(3.2.4) into (3.1.25) gives

$$\eta_t + \frac{2}{ma^2}\eta\eta_z + \left[\frac{11}{ma^2} - \frac{a^2(\rho^{(l)} - \rho^{(g)})Re^{(l)}}{\rho^{(l)}Fr^2}\right]\eta^2\eta_z + \frac{a^3}{3C}[\eta^3(\eta_z + a^2\eta_{zzz})]_z = 0. \tag{3.2.5}$$

In [38] the radial coordinate is stretched across the annular fluid, defining the thickness of the fluid by $h = \frac{a}{\beta}\eta$ where $\beta = a - 1 \ll 1$. Applying this stretch to (3.2.5) and rescaling in time by $t' = \frac{2\beta}{m}t$ gives the 'standard' form (to leading order in β)

$$h_t + hh_z + F^*h^2h_z + S^*[h^3(h_z + h_{zzz})]_z = 0, \tag{3.2.6}$$

where

$$\begin{aligned} F^* &= \frac{\beta}{1-3\beta}\left[\frac{11}{2} - \frac{m(\rho^{(l)} - \rho^{(g)})Re^{(l)}}{2\rho^{(l)}Fr^2}\right], \\ S^* &= \frac{m}{6C(1-3\beta)}\beta^2 = \frac{\pi\gamma\bar{R}_0^2}{12\bar{Q}^{(g)}\mu^{(g)}(1-3\beta)}\beta^2. \end{aligned} \tag{3.2.7}$$

If we neglect the effects of gravity, only retaining hyperbolic terms of $O(\epsilon)$, (3.2.6) reduces to

$$h_t + hh_z + S^*[h^3(h_z + h_{zzz})]_z = 0, \tag{3.2.8}$$

where

$$S^* = \frac{m}{6C}\beta^2 = \frac{\pi\bar{\gamma}\bar{R}_0^2}{12\bar{Q}^{(g)}\bar{\mu}^{(g)}}\beta^2. \tag{3.2.9}$$

Equation (3.2.8) was studied numerically by Kerchman [38] and will be henceforth be referred to as the Kerchman model. Like the long-wave model, the Kerchman model is a conservation law. The conserved quantity, however, is not the mass but h, i.e. mass is only conserved in an approximate, flattened-geometry sense. In contrast the long-wave model (3.1.25) has conserved quantity R^2 representing the mass in the full cylindrical geometry. The fact that mass is not conserved can be clearly seen in [38] where the continuity equation is only satisfied up to $O(\beta)$.

Note also that if the perturbations to the free surface remain small throughout the evolution, (3.2.8) can be approximated by the Kuramoto-Sivashinsky equation which is known to have spatio-temporal chaotic solutions (see, e.g. [29]); such behavior was shown to also exist for small values of S^* in [38].

3.2.2. Gravity-driven flow. The long-wave model (3.1.25) was derived using the air core's constant volume flux. If the core flux is set to zero so that only the gravity and capillary forces act on the fluids, i.e. $S_1 = 0$, then the leading order term of $f_2(\eta)$ becomes the leading order hyperbolic term in the thin-film limit. Substituting (3.2.1), (3.2.3), and (3.2.4) into (3.1.25) gives

$$\eta_t - \frac{(l-1)a^2}{l}\frac{Re^{(l)}}{Fr^2}\eta^2\eta_z + \frac{a^3}{3C}[\eta^3(\eta_z + a^2\eta_{zzz})]_z = 0. \tag{3.2.10}$$

Stretching the radial coordinates across the thin annular film as before, and then rescaling in time gives (to leading order in β) the thin-film Frenkel model discussed in Chapter 2,

$$h_t + \frac{1}{3}\frac{\partial}{\partial z}\left[h^3\left(1 + \frac{\tilde{S}_F h_z}{a^2} + \tilde{S}_F h_{zzz}\right)\right] = 0. \tag{3.2.11}$$

3.2.3. No imposed flow. Finally, if there is no imposed flow due to pressure or gravity, i.e. $S_1 = S_2 = 0$, the capillary forces dominate the evolution of the interface, and with a rescaling in time (3.2.6) simplifies to the evolution equation studied by Hammond [24],

$$h_t + \frac{1}{3}[h^3(h_z + h_{zzz})]_z = 0. \tag{3.2.12}$$

Kerchman [38] demonstrated that the long-time behavior of (3.2.12) differs from the $S \gg 1$ behavior of (3.2.6).

The relationship between the long-wave model (3.1.25) and Kerchman (3.2.8), Frenkel (3.2.11), and Hammond (3.2.12) models, as well as the Kerchman-Frenkel hybrid model (3.2.6) is sketched in $S - F - a$ parameter space in Figure 3.2.1. $S = 0$ corresponding to the linear limit is represented by the vertical (blue) plane boundary on the left; $F = 0$ corresponding to the absence of gravity corresponds to the horizontal (green) plane boundary on the bottom; $a = 1$ corresponding to the thin-film limit and Kerchman-Frenkel hybrid model is represented

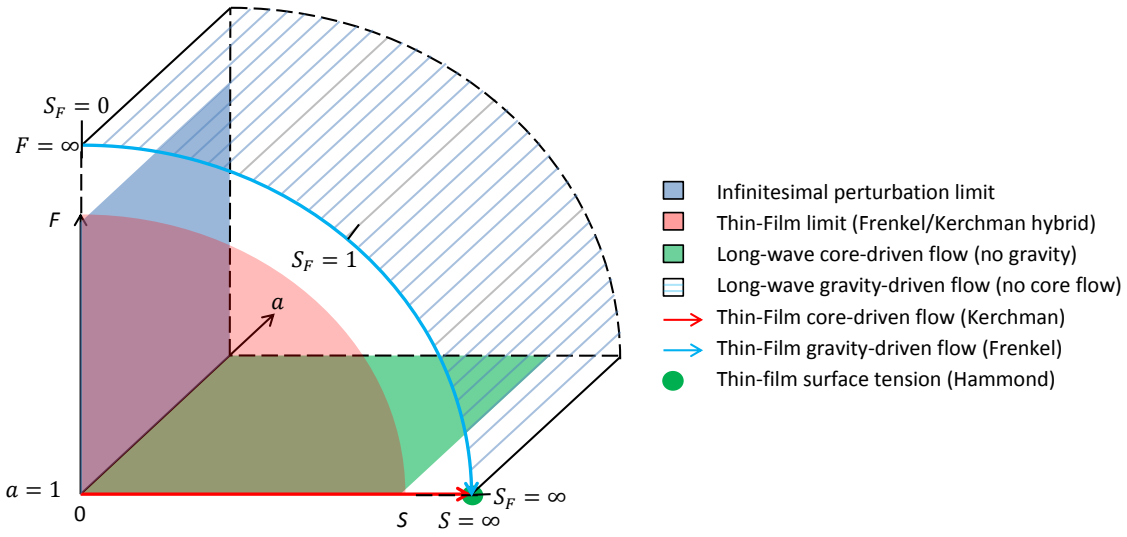

Figure 3.2.1: Visualization of the relationship between the long-wave and thin-film models in parameter space; see text for discussion.

by the vertical (pink) plane boundary in the front of the region (lying in the same plane as the paper). The Kerchman model then corresponds to the intersection of the $F = 0$ and $a = 1$ planes denoted by the solid red line. If the core flow speed is reduced while holding all other variables constant, both S and F increase with constant ratio $r = F/S$. Thus taking $\bar{Q}^{(g)} \to 0$ sends $S \to \infty$ and $F \to \infty$ along a plane defined by $F = rS$. The no core flow limit $\bar{Q}^{(g)} \to 0$ is pictured as a curved (striped) 'roof' on the parameter space. Thus the Frenkel model corresponds to the intersection of the $a = 1$ plane and the curved roof, denoted by the solid blue line. Finally, in the limit $\bar{Q}^{(g)} \to 0$ and $F \to 0$, the Hammond model is recovered; this is represented by the intersections of the Kerchman and Frenkel model, denoted by the green dot.

3.3. Linear stability analysis

The linear stability of the long-wave model (3.1.25) and thin-film models (3.2.6) and (3.2.8) are now examined by introducing an infinitesimal perturbation to the free surface:

$$R = 1 + A\exp[i(kz - \omega t)], \tag{3.3.1}$$

where $A \ll 1$ is the amplitude of the disturbance, k is its real wavenumber, $\Re[\omega]/k$ is its phase speed, and $\lambda = \Im[\omega]$ is its growth rate. Substituting (3.3.1) into (3.1.25), (3.2.6) and (3.2.8) and neglecting higher order terms in A gives the dispersion relations

$$\omega_{LW} = [S_1 a^2(a^2-1) + S_2(a)(1-a^2+2\ln a)]k \tag{3.3.2}$$

$$+iS_3(a^4-4a^2+3+4\ln a)(k^2-k^4)$$

$$= [1+F(a)]k + iS(a)(a^4-4a^2+3+4\ln a)(k^2-k^4), \tag{3.3.3}$$

$$\omega_{KF} = (1+F^*)k + iS^*(k^2-k^4), \tag{3.3.4}$$

$$\omega_K = k + iS^*(k^2-k^4), \tag{3.3.5}$$

where the long-wave dispersion relations (3.3.2) and (3.3.3) correspond to the scalings in (3.1.25) and (3.1.29), respectively.

Equation (3.3.3) is consistent with the analysis of the full equations by Hickox [25]. For example, in the case of no density stratification ($F = 0$) Hickox found the speed of an infinitesimal long-wave disturbance to be

$$c_0 = \frac{a^2(a^2-1)}{a^4+m-1}, \tag{3.3.6}$$

where $m = \mu^{(l)}/\mu^{(g)}$ is the viscosity ratio; compare with the speed of such a disturbance in the long-wave model

$$c_{LW} = \frac{a^2(a^2-1)}{m}; \tag{3.3.7}$$

in the asymptotic limit of large viscosity ratio $m \gg a$, these speeds agree.

In the thin-film model (3.2.6) the speed of characteristics is

$$c_K = \frac{2(a-1)}{m+2(a-1)}. \tag{3.3.8}$$

In the thin film limit $a-1 \ll 1$, $c_K \sim c_0$; as expected, retaining the full curvature allows the long-wave model to capture small perturbation behavior for a much wider range of a, provided m is large. Note that the disturbance speed (3.3.8) is also the speed of fluid parcels at the free surface; this point will be discussed further in Section 4.4.

In the case of density stratification, the long-wave limit of the propagation speed of a linear disturbance was found by Hickox to be

$$c_0 = \frac{(a^2-1)[a^4k + a^2(m+2k-3) + (k-1)(2m-3)] - 4(k-1)(m+a^4-1)\ln a}{(m+a^4-1)[k(a^2-1) + m - 2(k-1)\ln a]} \tag{3.3.9}$$

where $k = (p_z + \rho^{(l)}g)/(p_z + \rho^{(g)}g)$; in the case of large m (3.3.9) simplifies to

$$c_0 \sim \frac{1}{m}[a^4 - a^2 - 2(k-1)(1 - a^2 + 2\ln a)], \tag{3.3.10}$$

which is exactly the speed of infinitesimal free surface disturbances in the long-wave model (3.1.25).

CHAPTER 4

Comparison of locally Poiseuille and thin-film models with equal densities

Before proceeding to a comparison of the models derived in Chapter 3 with experiments, several key differences between the long-wave and thin-film models are highlighted using the equal-density case to illustrate the consequences of relying on the thin-film assumption. The main advantage of the thin-film models is the simplicity of their nonlinearities relative to those in the long-wave model; this makes them particularly amenable to analysis. This simplicity comes from effectively 'flattening the tube', or removing the cylindrical geometry from the problem. Note that the thin-film model is *not* equivalent, however, to flat-film models. This is easily seen by observing that the main source for instability growth in the thin-film models considered here is the first surface-tension term, a term which is not present in the flat-film models (compare, e.g., the Frenkel model [18] with the Benney model [3]). In some sense then, the thin-film model 'remembers' that it is in a cylindrical setting but 'forgets' that there is a centerline in the tube.

4.1. Temporal solutions

A thorough comparison of numerical solutions to the long-wave (3.1.25) and Kerchman (3.2.8) models is now given. Each equation is integrated using the method of lines. Two approaches were used and compared. In the first approach, identical to that used to generate the numerical solutions in Chapter 2, a pseudospectral method was used where the spatial derivatives were calculated in Fourier space and the nonlinearities calculated in physical space. A simple second-order predictor-corrector scheme for time integration was used. Since conservation of volume is embedded in (3.1.25), and h is conserved in (3.2.8), the conserved quantity for each model was carefully monitored during each simulation.

Due to the highly nonlinear nature of both models, the Fourier coefficients were dealiased. The dealiasing process is described for the long-wave model (3.1.25); the process for dealiasing (3.2.8) is analagous. The highest degree nonlinearities are present in the hyperbolic term, i.e. $R^{-6}R_z$. After each time step, modes of R, R^{-1} and $\log R$ with $k > N/2$ were set equal to zero. Quadratic nonlinearities were then calculated in physical space, and the resulting vector was dealiased again as before. Cubic nonlinearities were computed from the linear and quadratic terms and subsequently dealiased, and this process was continued until all the nonlinear coefficient terms in (3.1.25) had been calculated. In order to find accurate solutions, all suppressed modes must be insignificant in the evolution. To ensure this was the case, the spectrum of R, R^{-1} and $\log R$ were monitored during simulations along with the mass of the liquid. If the suppressed modes became significant (or the total volume of liquid varied), more points were added to the simulation. Each simulation was initially run with $2N = 128$ points per $L = 2\pi$ cm; only the case of very high surface tension parameter ($S > 3$) required increasing the number of points.

Due to the high-degree of nonlinearity, the needed time step in order to achieve stability is quite small. In dimensional form, the hyperbolic term requires that

$$\Delta\bar{t} < \frac{2\bar{a}^2\bar{Q}^{(g)}}{\pi m}\left(\frac{\bar{a}^2}{\bar{R}_{min}^6} - \frac{1}{\bar{R}_{min}^4}\right)\Delta\bar{z}, \tag{4.1.1}$$

while the capillary terms dictate that

$$\Delta\bar{t} < -\frac{\gamma}{16\mu^{(l)}\bar{R}_{min}}\left(-\frac{\bar{a}^4}{\bar{R}_{min}^4} + 4\bar{a}^2 - 3\bar{R}_{min}^2 + 4\bar{R}_{min}^2\ln\frac{\bar{R}}{\bar{a}}\right)(\Delta\bar{z})^4, \tag{4.1.2}$$

where $\Delta\bar{z}$ is the spatial discretization. For most simulations $\Delta\bar{t} = 10^{-4}$; $\Delta\bar{t}$ was decreased if $\bar{R}_{min}$ became small enough to threaten the conservation of volume. (The Fourier modes of the derivatives and nonlinear terms were carefully monitored to ensure they decayed appropriately). For low values of S this time step proved sufficient for stability and volume conservation. For high S, the time-step required once the initial instability saturated decreased to $\Delta\bar{t} = O(10^{-5})$ or even smaller. This dependence on surface tension parameter reflects the larger instabilities promoted by higher surface tension leading to smaller values of $\bar{R}_{min}$.

For initial conditions, the flat free surface was perturbed with either a single mode or multiple modes, i.e. $\bar{R}(\bar{z},0) = \bar{R}_0 - \sum_{k=1}^{n} \beta \cos(2\pi k\bar{z} + \alpha_k)$ where α_k is a random phase shift for each mode and typically $\beta = 0.2$ for the amplitude. Anywhere from 1 to 100 modes were used in the initial condition. The long-time behavior of the solution was not found to depend strongly on α_i, β or n.

The second approach taken also used the method of lines and is the approach used in [5]; it is briefly summarized here. Second-order centered differences were used to approximate the derivatives, and an implicit ODE solver was used to march in time. Gears method, as implemented in the ODE solver DLSODE from Netlib was used for solving our system of ODEs. Both methods were compared and were found to give results in good agreement with each other. For most simulations below, the first method was used for both the long-wave and thin-film models (with appropriate modifications to the dealiasing above for the thin-film model).

Figure 4.1.1(a)-(b) show the evolution of a slightly perturbed interface in the long-wave model for $S^* = 0.3$ for two different film thicknesses. Snapshots are taken at equal time intervals and plotted in a frame of reference moving with the undisturbed interface. In Figure 4.1.1(a) the interface exhibits spatio-temporal chaotic behavior reminiscent of solutions to the Kuramoto-Sivashinsky equation (see, e.g., [29]) while in (b) the interface has settled into a series of well-defined traveling waves. While there continue to be interactions between the waves as additional time passes, the coalescence of waves through mergers ceases beyond that shown in the figure. The presence of dispersive terms in KS-like equations has been shown to be regularizing leading to the formation of traveling waves, see e.g. [60; 8; 32]; hence it is not surprising that solutions to the fully nonlinear models (3.1.25) and (3.2.8) exhibit traveling wave behavior.

Note that unlike gravity-driven flow described by (2.2.12), in no simulations of (3.1.25) was blow-up observed. This highlights the coupling between the core flow and annular flow through the stress at the free surface; the effect of a growing instability on the hyperbolic term (through the increase in free surface stress) prevents blow-up. This is in line with behavior seen in the experiments. At high volume flow rates $\bar{Q}^{(g)}$ the rapid increase in airspeed which is

required to allow air to pass through a constricted opening prevents plug formation. Also note that the waves now travel up the tube, i.e. from left to right, and that the slight depression that was in front of traveling wave solutions found for the gravity-driven long-wave model (2.2.12) in Chapter 2 has moved to the right of the wave and is still in front of the waves (see Figure 4.1.1(b)). This fore-aft asymmetry is commonly seen in long-wave, thin-film, flat-film and integral models, and is even observed in simulations of propagating liquid plugs [6; 80]. It is interesting to speculate that some features of the free surface in [6; 80] somehow survive through many orders of magnitude scalings of surface shear stress and Reynolds number of the gas phase; further analysis of this phenomenon is left for future work.

Figure 4.1.1(c) shows the evolution of a perturbed interface in the Kerchman model, also for $S^* = 0.3$. After the initial growth of the waves, there is a period of wave mergers and coalescence until only the largest wave survives, consuming all the others. Kerchman found this to be the case for $0.15 < S^* < 1.0$ [38]. This qualitative difference in behavior can be attributed to the thin-film model's lack of memory of the centerline of the tube. In the long-wave model the core gas moves faster as the annular fluid waves grow, impinging on the core fluid. The additional stress caused by the increased core velocity behaves as an additional stabilizing term, thus preventing unlimited instability growth. In the thin-film model there is no memory of the centerline of the tube, and so the instabilities can grow unchecked until they exhaust the supply of fluid in the rest of the domain. Only then, due to conservation of mass, do the instabilities saturate. Note that, unless otherwise specified, $\bar{a} = 0.5$ cm throughout the figures in Chapter 4.

4.2. Traveling wave solutions

To further explore this difference we look for traveling wave solutions to both models by moving to a frame of reference traveling with the wave, i.e. let

$$Z = z - ct. \tag{4.2.1}$$

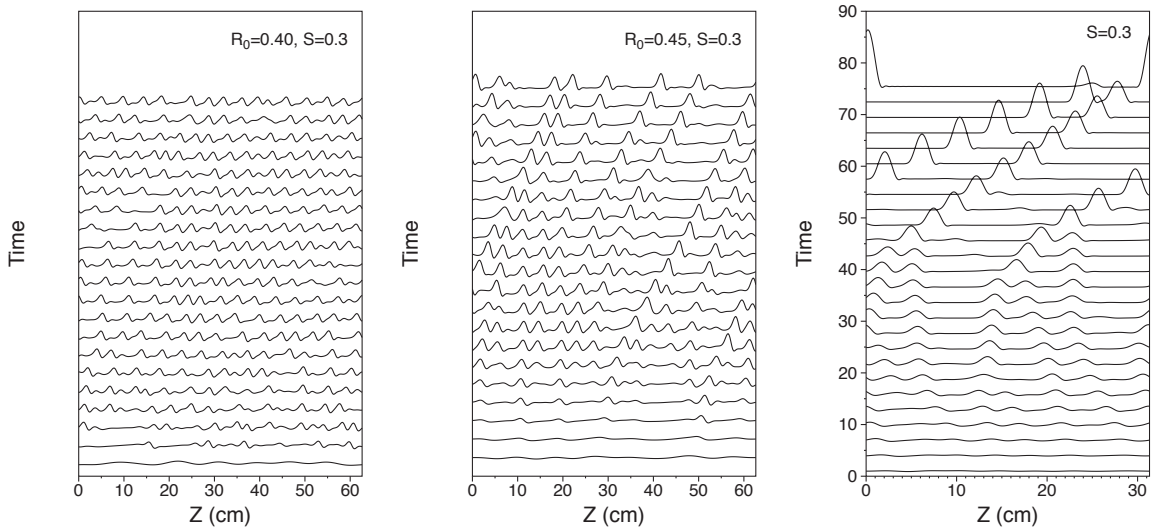

Figure 4.1.1: (a) Time snapshots showing the evolution of solutions to equation (3.1.25) in a periodic domain for $S^* \approx 0.3$, $a \approx 1.25$ and $\bar{a} = 0.5$ cm. (Unless otherwise specified, $\bar{a} = 0.5$ cm throughout Chapter 4.) Interfacial profiles are shown successively shifted at equal time intervals. Profiles are shown in the frame of reference moving with an undisturbed interface. (b) Same as (a) but with $a \approx 1.1$. (c) Solutions to (3.2.8) are shown for $S^* = 0.3$.

Substituting (4.2.1) into the long-wave (3.1.25) and Kerchman (3.2.8) models respectively yield fourth-order ODEs

$$cR' = S_1 f_1(R)R' + \frac{S_3}{R}\frac{d}{dZ}[f_3(R)R' + f_3(R)R'''], \tag{4.2.2}$$

$$ch' = hh' + S^*\frac{d}{dZ}[h^3(h' + h''')]. \tag{4.2.3}$$

As neither (4.2.2) or (4.2.3) are directly solvable, we seek solutions numerically as in Chapter 2. Solving the model PDEs and letting the solutions settle to a steady series of traveling waves, we use one wave of this solution as an initial approximation with an appropriate domain, and then refine using a collocation-method 2-point boundary value problem solver.

Figure 4.2.1(a) shows traveling wave solutions to the long-wave model for various values of surface tension with all other experimental parameters held constant. The wave width is almost independent of surface tension, similar to solutions to the Kerchman model [38]. Figure 4.2.1(b) shows the wave profile for two different cell lengths; again the wave amplitude grows while there is little change in the width of the wave. Figure 4.2.1(c) shows the wave profile for various mean film thicknesses. As the mean thickness decreases, the width of the waves

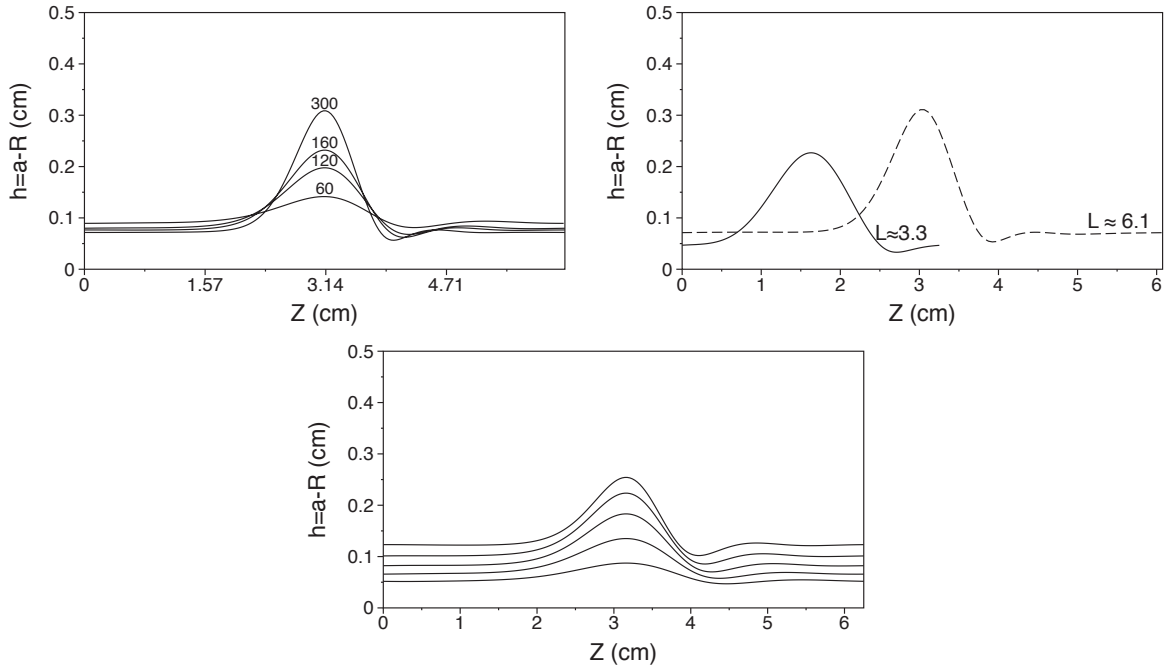

Figure 4.2.1: (a) Pulse profile for various values of surface tension ($\bar{R}_0 = .40$ cm, $\bar{\lambda} = 2\pi$ cm); (b) pulse profile for various wavelengths ($\bar{R}_0 = .40$ cm, $\gamma = 120$ dyn/cm); (c) pulse profile for various mean liquid thicknesses ($\gamma = 100$ dyn/cm, $\bar{\lambda} = 2\pi$ cm.) In all figures $\bar{a} = 0.5$ cm.

increases slightly; this feature is of course not seen by the Kerchman model which does not see the mean film thickness.

Figure 4.2.2 shows traveling waves for five different domain lengths for the (a) long-wave model and (b) Kerchman model. As the cell length increases in the long-wave model, the geometry of the tube restricts growth of the pulse height. In the Kerchman model the pulse height grows roughly proportionally to the cell length. This is consistent with the model solutions' behavior described above, where the Kerchman model's growth is only bounded by mass conservation while the long-wave model's growth is bounded primarily by mass conservation only for very thin films and primarily by the core fluid's increased velocity for moderate to thick films. This difference has implications for the thickness of the substrate layer outside the wave crest as well; in the long-wave model, as the cell length increases and the geometry restricts growth of the wave, the substrate layer increases in thickness to accomodate the additional liquid that the increasing cell length introduces. This effect is not seen in the small amplitude

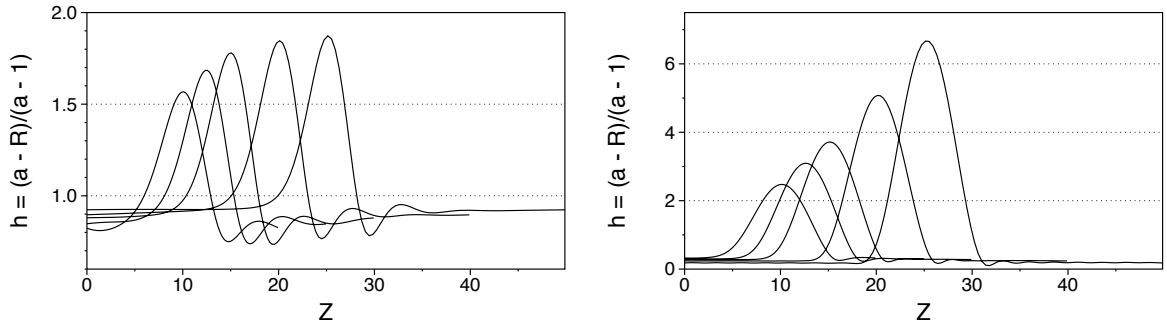

Figure 4.2.2: (a) Long-wave model pulse profiles for various wavelengths and $\bar{a} = 0.5$ cm. The geometry of the tube hampers instability growth; the substrate layer away from the crests becomes thicker for longer wavelengths. (b) Kerchman model pulse profiles for various wavelengths; the 'flattened geometry' does not hamper instability growth and the substrate layer becomes thinner for longer wavelengths.

model where the waves are allowed to grow unbounded in amplitude and the substrate layer actually decreases slightly in thickness with increasing cell length.

Figure 4.2.3(a) shows traveling wave solutions to both models for fixed S and domain length $\bar{L}$. Note that the amplitude of the waves has been normalized so that the mean thickness of each solution is 1. The long-wave solutions tend to the Kerchman solution as one would expect as the thickness of the film decreases, i.e. $\bar{R}_0 \to \bar{a} = 0.5$ cm. Figure 4.2.3(b) shows the dependence of amplitude on film thickness. For thick films (small $\bar{R}_0$), the long-wave model's normalized amplitude decays as expected, reflecting the restricted growth as determined by the cylindrical geometry. Interestingly, for high values of S and very thin films ($\bar{R}_0 \to \bar{a} = 0.5$ cm), the thin-film model actually understates the normalized amplitude. This may be attributable to issues of mass conservation (rather than numerical error) as the thin-film model does not conserve mass, but rather the quantity h; this effect is subdominant to the first effect of restricted amplitude growth for all but the thinnest films and high values of S. The thin-film model with second-order hyperbolic terms (3.2.6) and $F = 0$ is also shown for comparison. Figure 4.2.4 shows the speed of traveling wave solutions for fixed S as $\bar{R}_0$ varies. The thin-film model underestimates the wave speed relative to the long-wave model.

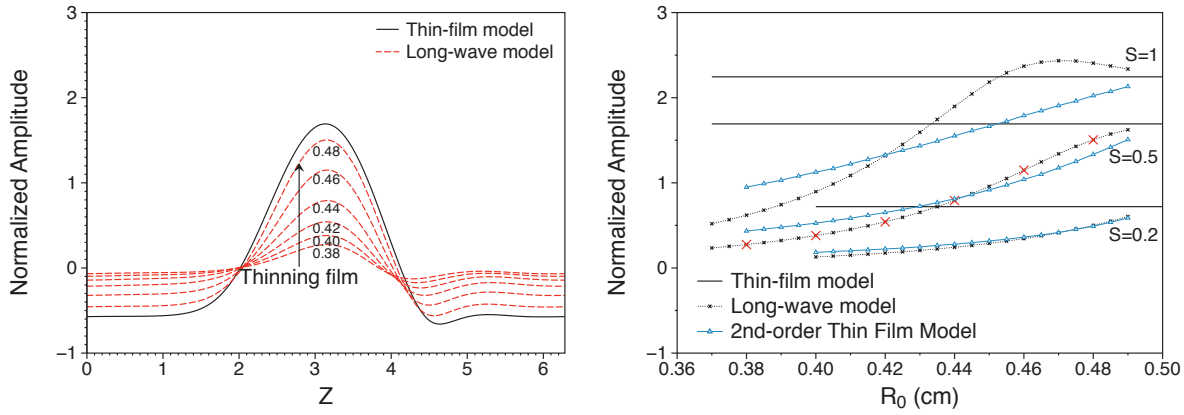

Figure 4.2.3: (a): Solutions to the long-wave model for $S = 0.5$ are plotted (dotted red) for various values of $\bar{R}_0$ approaching a dry tube ($\bar{a} = \bar{R}_0 = 0.5$ cm). The solution to the Kerchman thin-film model for $S = 0.5$ is plotted (solid black). (b) Normalized amplitude of long-wave and thin-film solutions are shown for various values of S and $\bar{R}_0$.

4.3. Mass transport

In Chapter 2, traveling wave solutions to the gravity-driven model (2.2.12) were analyzed using the stream function to study the flow of the fluid layer. In solutions like the one shown in Figure 2.6.2(b), the flow is quasi-laminar, where the streamlines are simply fanned or constricted with variations in the free surface. In solutions like that shown in Figure 2.6.2(a), however, some portion of the fluid is contained within a trapped core or recirculation zone which rolls over the substrate layer.

In order to determine whether the airflow long-wave model (3.1.25) and Kerchman model (3.2.8) exhibit the existence of mass transport waves, the stream function in a frame of reference moving with the wave is calculated. For the long-wave model the stream function is defined as before by the velocity field:

$$u_2 - c = \frac{1}{r}\partial_r(r\Psi_2), \quad w_2 = -\partial_z\Psi_2. \tag{4.3.1}$$

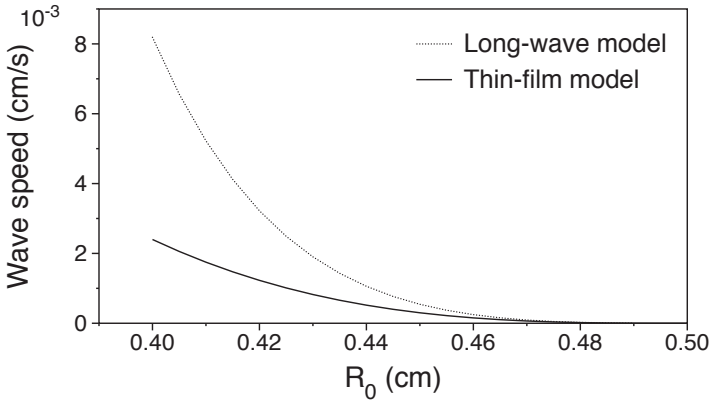

Figure 4.2.4: Wave speed as a function of $\bar{R}_0$ for long-wave vs. Kerchman model. $\bar{a} = 0.5$ cm.

Finding w via the continuity equation and then integrating (4.3.1), the stream function is given (in dimensional form) by

$$\Psi_2 = \left[-\frac{2\bar{Q}^{(g)}\mu^{(g)}}{\pi\mu^{(l)}\bar{R}^4} + \frac{\gamma}{4\mu^{(l)}\bar{R}^2}(\bar{R}_{\bar{z}} + \bar{R}^2\bar{R}_{\bar{z}\bar{z}\bar{z}})\right]\left(\frac{\bar{r}^3}{4} - \frac{\bar{a}^2\bar{r}}{2} + \frac{\bar{a}^4}{4\bar{r}}\right)$$
$$- \frac{\gamma}{2\mu^{(l)}}(\bar{R}_{\bar{z}} + \bar{R}^2\bar{R}_{\bar{z}\bar{z}\bar{z}})\left(-\frac{\bar{r}}{4} + \frac{\bar{a}^2}{4\bar{r}} + \frac{\bar{r}}{2}\ln\frac{\bar{r}}{\bar{a}}\right) - \frac{\bar{c}\bar{r}}{2}. \tag{4.3.2}$$

Both mass transport waves and shear-enhancing waves are found for the long-wave model. Figure 4.3.1 shows the streamlines for various values of surface tension parameter S with all other parameters being held constant. As S increases, the waves undergo a transition from shear-enhancing waves to mass transport waves. Three stationary points develop in the traveling reference frame, two at the liquid-air interface which are endpoints of a separatrix separating the closed streamlines from the open ones, and a third at the center of the closed streamlines.

Figure 4.3.2 shows the streamlines for $S = 1$ and varying film thickness. As the film thins, the waves transition from shear-enhancing waves to mass transport waves. Figure 4.3.2 shows the dependence of wave volume on film thickness. It is interesting to note that there is some film thickness for which the wave volume is maximized. Films thinner than this critical thickness do not have enough liquid in the domain to maximize their volume, while thicker films have damped amplitude from the centerline effects, restricting, and eventually eliminating, the size of the trapped core.

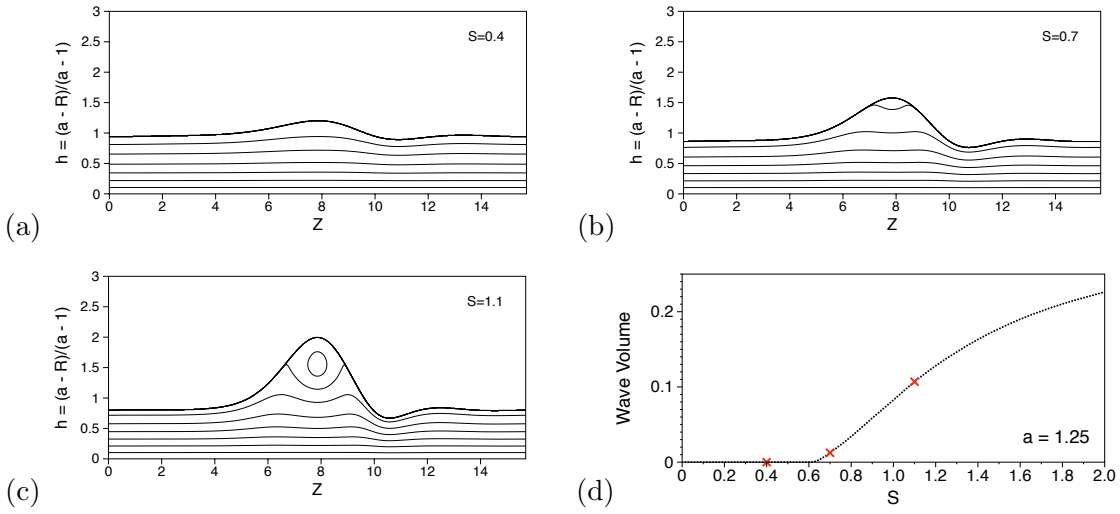

Figure 4.3.1: (a)-(c): Streamlines plotted in traveling reference frame for solutions to the long-wave model (3.1.25) for varying values of S and $a = 1.25$ ($\bar{a} = 0.5$ cm). (d): Volume of the trapped core as a function of S. For $a = 1.25$, $S < 0.6$, no trapped core exists.

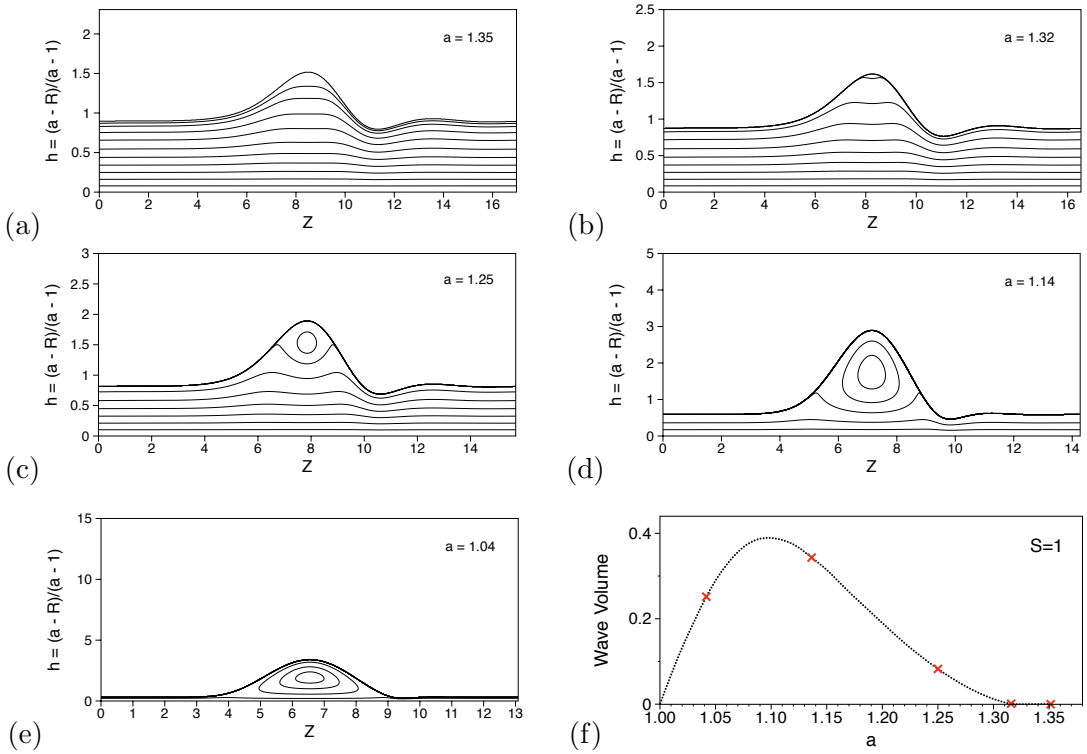

Figure 4.3.2: (a)-(e): Same as Figure 4.3.1(a)-(c) but for fixed $S = 1$ and varying a. (f): Volume of the trapped core as a function of a. For thick films ($a > 1.32$ when $S = 1$) no trapped core exists.

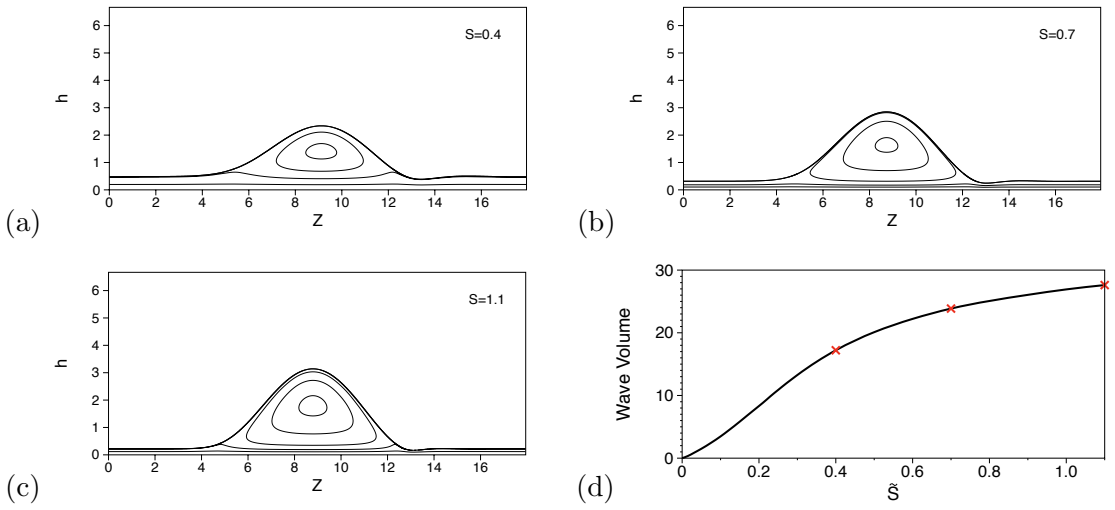

Figure 4.3.3: (a)-(c): Same as Figure 4.3.1(a)-(c) but for the Kerchman thin-film model (3.2.8). Streamlines plotted in traveling reference frame for solutions to the Kerchman thin-film model for varying values of S. (d): Volume of the trapped core as a function of S. Every traveling wave has a non-zero volume of fluid inside a trapped core.

Kerchman derives the streamfunction for the thin-film model and is given here using the notation from [38] with several apparent typos corrected. The streamfunction is defined by

$$W_2 + w_2 - W_{if}(V-1) = \frac{\partial_y \Psi_2}{\beta}, \quad u_2 = -\partial_z \Psi_2, \tag{4.3.3}$$

and is found to be

$$\frac{\Psi_2}{\beta W_{if}} = \frac{1}{2}(1-y^2) + (1-V)(y-1) - \frac{S(\eta_z + \eta_{zzz})}{2}[y^3 - 3y + 2 + 3\eta(1-y)^2]. \tag{4.3.4}$$

FIgure 4.3.3 shows the streamlines for corresponding values of surface tension parameter S for the Kerchman model. Unlike in the long-wave model, there is no transition from shear-enhancing waves to mass transport waves, but rather all waves are found to be mass transport waves. Three fixed points exist in all wave solutions; two on the free surface and one in the recirculation zone as described above. The volume of the trapped core tends to 0 as $S \to 0$.

As the surface tension parameter has dependence on film thickness $S = S(a)$, the bifurcation described above is briefly considered in dimensional form. Figure 4.3.4 shows the wave volume for varying surface tension and film thickness for solutions to the long-wave model. Figure 4.3.4(a) shows the trend of increasing the surface tension increasing the wave volume.

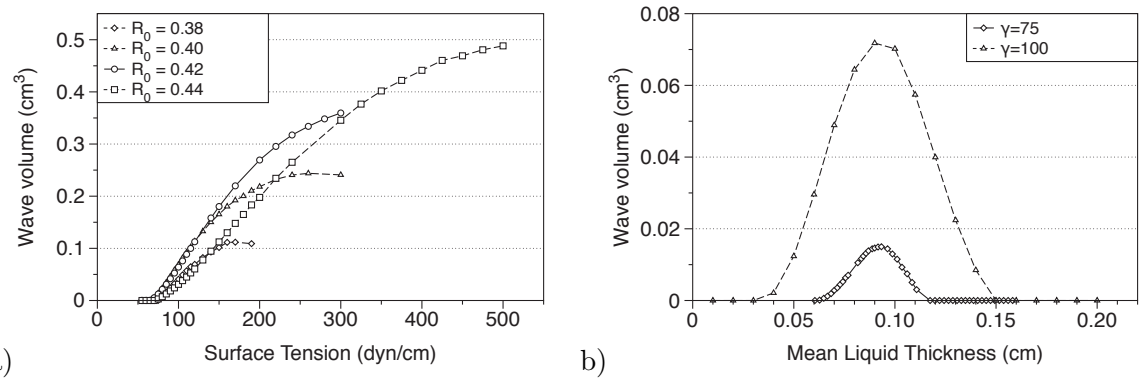

Figure 4.3.4: Volume of trapped core as a function of (a) surface tension ($\bar{R}_0 = .40$), and (b) mean film thickness $\bar{h}$ ($\gamma = 100$ dyn/cm). In both figures $\bar{a} = 0.5$ cm.

As the surface tension parameter increases the trapped core forms and grows (at first quite rapidly); this volume growth tapers off as the instability growth is eventually hampered by the geometry of the tube, i.e. as the liquid approaches clogging, the model fights further instability growth with more vigor. The greater the mean liquid thickness, the sooner this tapering occurs as S increases, i.e. the instabilities have more room to grow before the geometry seriously restricts their growth. This behavior is markedly different than the Kerchman model in which instabilies are permitted to grow essentially without bound. Figure 4.3.4(b) shows that, provided the surface tension is high enough, there is a range of film thicknesses for which a trapped core can exist.

In shear-enhancing traveling waves all of the liquid flux comes from the substrate layer moving up the tube. In mass transport traveling waves both the trapped core in the wave and the substrate layer contribute to the total liquid flux. Figure 4.3.5(a) shows the total liquid volume flux and the proportion of liquid flux due to the substrate layer and the trapped wave core for one set of parameter values. Figure 4.3.5(b) shows the percentage of the liquid flux that the trapped core contributes for four different film thicknesses as a function of surface tension. Note that the percentage of flux settles down to a higher value for high surface tension when the film is thinnest.

The regions of mass-transport vs. shear-enhancing waves are summarized for the case of equal densities in Figure 4.3.6. The vertical boundary on the left represents the thin-film limit

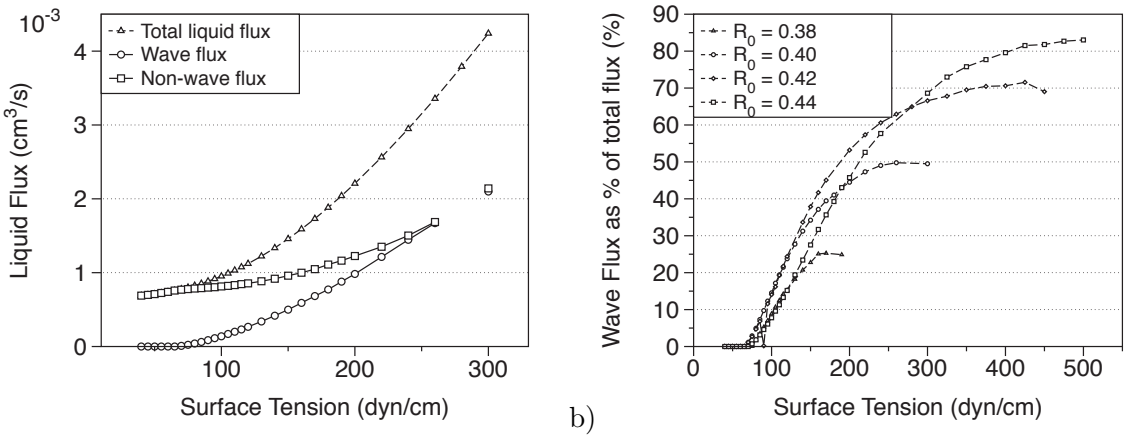

Figure 4.3.5: (a) Total liquid volume flux and the portions contributed by trapped core vs. substrate layer ($\gamma = 100$ dyn/cm, $\bar{R}_0 = 0.40$ cm, $\bar{a} = 0.5$ cm). (b) Flux due to trapped core as a percentage of the total liquid flux for various values of $\bar{R}_0$.

(Kerchman model). Combining Figures 3.2.1, 4.3.6 and 2.6.3 allows further visualization of the regions of mass transport and shear-enhancing waves along the boundaries of $F - S - a$ parameter space in Figure 4.3.7. We briefly discuss the corresponding regions in the interior of this parameter space in Chapter 5, though a full study is left to future work.

4.4. Streamline bifurcation

As shown in the preceding section, both the long-wave model and the Kerchman model exhibit trapped core traveling wave solutions for large-amplitude waves. As the amplitude of the waves decrease, the Kerchman model continues to exhibit a trapped core, with volume decreasing to zero as the amplitude decreases to zero. On the other hand, the long-wave model exhibits a sharp change in behavior, where the trapped core disappears altogether, and the waves become shear-enhancing waves at small amplitude. This happens through the merging of the two stagnation points on the free surface with the stagnation point at the center of the trapped core, i.e. as the wave amplitude decreases, the trapped core becomes smaller and smaller until it finally collapses onto a single stagnation point on the interface near the crest of the wave (and immediately disappears as the amplitude continues to decrease).

Before returning to the case of unequal densities, some explanation of the presence (absence) of this streamline bifurcation in the long-wave (thin-film) model is given. As mentioned in

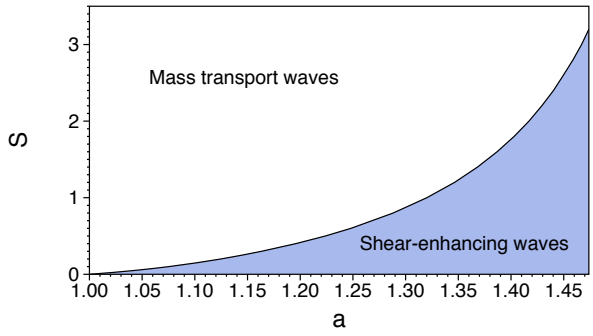

Figure 4.3.6: Regions in $S - a$ parameter space of mass transport waves and shear-enhancing waves for the long-wave model.

Section 3.3 the speed of an infinitesimal free surface perturbation in the Kerchman model is identical to the speed of a fluid parcel at the free surface, i.e. the fluid travels with the wave.

On the other hand, the axial film velocity in the long-wave model is (in dimensional form)

$$\begin{aligned}\bar{w} =& \left[-\frac{2\bar{Q}^{(g)}\mu^{(g)}}{\pi\mu^{(l)}\bar{R}^4} + \frac{\gamma}{4\mu^{(l)}\bar{R}^2}(\bar{R}_{\bar{z}} + \bar{R}^2\bar{R}_{\bar{z}\bar{z}\bar{z}})\right](\bar{r}^2 - \bar{a}^2) \\ & -\frac{\gamma}{2\mu^{(l)}}(\bar{R}_{\bar{z}} + \bar{R}^2\bar{R}_{\bar{z}\bar{z}\bar{z}})\ln\frac{\bar{r}}{\bar{a}}. \end{aligned} \tag{4.4.1}$$

Neglecting all derivatives of $\bar{R}$ and approximating $\bar{R}$ by $\bar{R}_0$ for an infinitesimal perturbation reduces (4.4.1) to

$$\bar{w}(\bar{r}) = \left(\frac{2\bar{Q}^{(g)}\mu^{(g)}}{\pi\mu^{(l)}\bar{R}_0^4}\right)(\bar{a}^2 - \bar{r}^2). \tag{4.4.2}$$

As $\bar{R} \to \bar{R}_0$ uniformly, we find that the velocity at the interface tends to

$$\bar{w}_i = \bar{w}(\bar{R}_0) = \left(\frac{2\bar{Q}^{(g)}\mu^{(g)}}{\pi\mu^{(l)}\bar{R}_0^4}\right)(\bar{a}^2 - \bar{R}_0^2). \tag{4.4.3}$$

The speed of an infinitesimal perturbation is given by

$$\bar{c} = \left(\frac{2\bar{Q}^{(g)}\mu^{(g)}}{\pi\mu^{(l)}\bar{R}_0^4}\right)\left(\frac{\bar{a}^4}{\bar{R}_0^2} - \bar{a}^2\right). \tag{4.4.4}$$

A quick comparison of $\bar{w}_i$ and $\bar{c}$ shows that the difference in interface velocity and wave velocity in the linear limit is due to the difference in the two functions

$$f_i(\bar{R}_0) = \bar{a}^2 - \bar{R}_0^2, \quad f_w(\bar{R}_0) = \frac{\bar{a}^4}{\bar{R}_0^2} - \bar{a}^2. \tag{4.4.5}$$

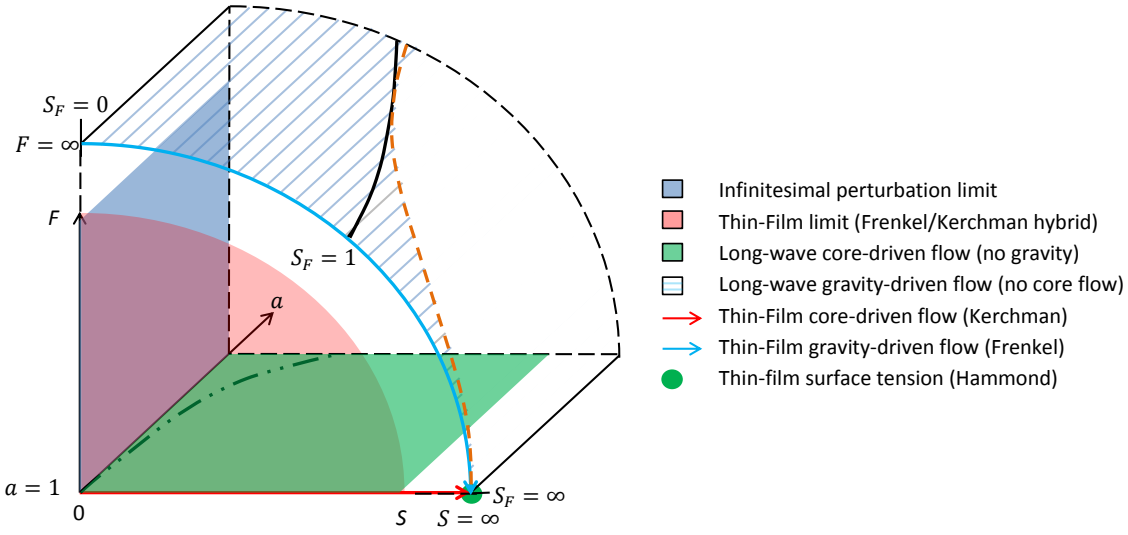

Figure 4.3.7: Parameter space containing long-wave and thin-film models. Same as Figure 3.2.1 but with streamline bifurcation lines for no gravity (dot-dashed black line) and no airflow (solid black line) and with traveling-wave existence boundary (dashed orange line).

Figure 4.4.1 shows a plot of these two functions. As $\bar{R}_0 \to \bar{a}$, i.e. the fluid layer becomes thinner, the thin-film approximation becomes valid and the two functions become asymptotically close.

A natural question to ask is, for a given film thickness in the long-wave model, how large must the amplitude of a wave be to allow a trapped core to form? A crude estimate of the answer can be found by considering the limit of an infinitesimal interfacial perturbation. The existence of trapped cores is guaranteed by the presence of a point on the interface (say at the wave crest) having greater horizontal velocity than the wave, i.e. $\bar{w}_i > \bar{c}$. If we are interested in a wave with small amplitude given by $\bar{\alpha}$, we want the interface velocity at the wave crest to be greater than the wave velocity:

$$f_2(\bar{R}_0) = f_1(\bar{R}_0 - \bar{\alpha}), \tag{4.4.6}$$

i.e.

$$\frac{\bar{a}^4}{\bar{R}_0^2} - \bar{a}^2 - [\bar{a}^2 - (\bar{R}_0 - \bar{\alpha})^2] = 0. \tag{4.4.7}$$

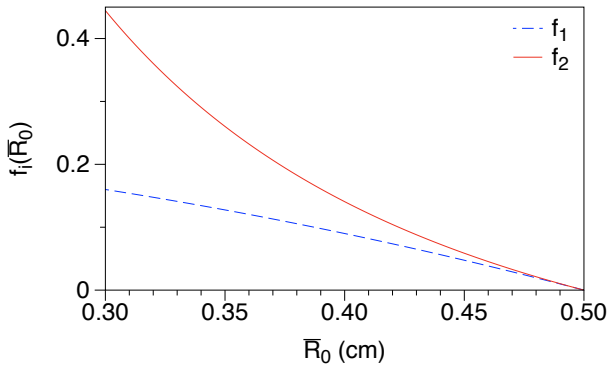

Figure 4.4.1: Wave speed and interface velocity for various $\bar{R}_0$ in the linear limit $\bar{R}(\bar{z},\bar{t}) \to \bar{R}_0$. As $\bar{R}_0 \to \bar{a} = 0.5$ cm, the two speeds converge. The wave speed is greater than the interface speed as expected for the existence of shear-enhancing waves in the linear limit.

This becomes a quadratic equation in $\bar{\alpha}$ with two solutions, the meaningful one being:

$$\bar{\alpha} = \bar{R}_0 - \frac{1}{\bar{R}_0}(2\bar{a}^2\bar{R}_0^2 - \bar{a}^4)^{1/2}. \tag{4.4.8}$$

This solution is plotted in Figure 4.4.2.

Note that this wave amplitude is only real when

$$\bar{R}_0 > \frac{\bar{a}}{\sqrt{2}}, \tag{4.4.9}$$

indicating that for $\bar{R}_0$ smaller than this value (e.g. $\bar{R}_0 < 0.3525$ cm when $\bar{a} = 0.5$ cm), there *cannot* exist mass transport waves according to the linear analysis. Of course by this point we are well outside the range of infinitesimal perturbations, and so it is not surprising that this prediction does not match the nonlinear behavior (see Figure 4.4.2).

The source of this difference between wave speed and interface speed in the long-wave model is the cylindrical form of the continuity equation. If we were to ignore the cylindrical geometry while integrating across the fluid layer, i.e. replace the continuity equation

$$R_t - \frac{1}{R}\frac{\partial}{\partial z}\int_R^a urdr = 0, \tag{4.4.10}$$

with

$$R_t - \frac{\partial}{\partial z}\int_R^a udr = 0, \tag{4.4.11}$$

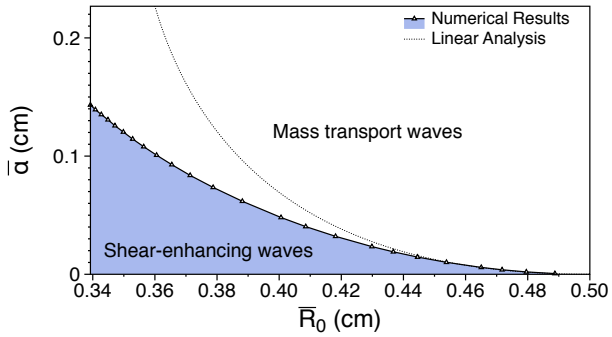

Figure 4.4.2: The amplitude of the wave at which waves transition from being shear-enhancing waves to mass waves as predicted by (4.4.8) and by the nonlinear results in Figure 4.3.6. For waves with greater amplitude, mass transport occurs; for waves of less amplitude, no trapped cores exist ($\bar{a} = 0.5$ cm).

the wave speed and interface velocity are identical. Incorporating the geometry thus includes this bifurcation effect that the thin-film assumption artificially removes.

Before returning to the general case of unequal core and annular densities, one further comment is made about the models. As will be discussed in Chapter 5, while the long-wave model is applicable for a wider range of film thickness and captures qualitative behavior missed by the thin-film model, it underestimates the free surface stress caused by the core flow. As a result, for a given film thickness the liquid flux is underestimated by the model. There are at least two methods by which this can be remedied artificially in the model: by boosting either (1) the viscosity of the core fluid or (2) the surface tension. Boosting the air viscosity alone decreases S but speeds up the evolution of the entire system and causes shear-enhancing waves to form; see [5] for a more detailed look at boosting the viscosity. On the other hand, increasing only the surface tension increases S (and does not directly affect the timescale through S_1) and causes mass transport waves to form. In other words, for a given mean liquid thickness, both methods boost the liquid flux and allow the liquid thickness to fall in line with the experimental predictions, albeit by different mechanisms. In principle an appropriate combination of these two remedies would also help the model predict the correct thickness for a given flux. Figure

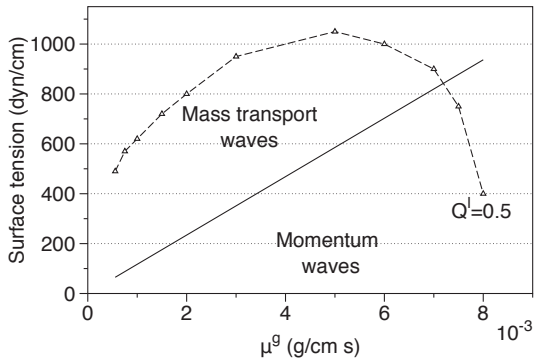

Figure 4.4.3: Plot of values of surface tension and air viscosity that produce experimentally valid thicknesses for $\bar{Q}^{(l)} = 0.5$ cm^3/min.

4.4.3 plots different combinations of surface tension and air viscosity which lead to correct predictions of the experimental thicknesses for $\bar{Q}^{(l)} = 0.5$ mL/s, and whether the waves produced by the model are shear-enhancing waves or mass transport waves.

It is somewhat interesting that for combinations of parameters relevant to our experiments, the wave speed remains approximately constant regardless of what combination of surface tension boost and viscosity boost is used, i.e. it appears that the wave speed is approximately a function of mean thickness and the liquid volume flux only. Since the model wave speed appears to be roughly determined by the mean thickness and the liquid volume flux, it does not appear possible to match all three characteristics between the current model and the experiments. This inability of the current model to adjust to experimental data offers a preview of the need for modeling improvements. In Chapter 5 we return to the case of unequal densities, conduct a thorough comparison of experiments and the long-wave model, and suggest possible modeling improvements.

CHAPTER 5

Further airflow modeling

We now return to the general case of the core and annular fluids having unequal densities. In order to determine how well the model performs, two sets of experiments were again performed in the UNC Joint Fluids Lab. Results are presented in Section 5.1 that indicate the model is able to qualitatively capture trends in the data and is an improvement over the exact solution, but is unable to quantitatively match the film's behavior in the experiments reported here.

Given the excellent agreement of the long-wave model with gravity-driven experiments, the discrepancy in the case of airflow between model and experiments appears to be due to the model underestimating and incorrectly assessing the free surface stress created by the wavy free surface. To study this stress, the liquid flow is, for the moment, neglected and airflow over a wavy rigid wall in (i) flat channel geometry and (ii) cylindrical pipe geometry is considered in Sections 5.2 and 5.3, respectively. A new modeling approach is developed which compares favorably with experiments conducted in wavy channels and pipes as well as models in the literature.

This improved assessment of the free surface stress is then incorporated into the liquid model in Section 5.4. Linear stability analysis is conducted in Section 5.5 and solutions to the model are presented in Section 5.6. A full comparison with experiments is left for future work.

5.1. Comparison of locally Poiseuille airflow model with experiments

The first set of experiments was described in Section 1.3. As with gravity-driven flow considered in Chapter 2, the model specifies the film's mean thickness *a priori* while the flux varies as the solution evolves; in the experiments the volume flux is prescribed and the thickness varies as the experiment progresses. Thus a comparison between model and experiment is again needed to verify that film thicknesses corresponding to values of the liquid flux are in agreement.

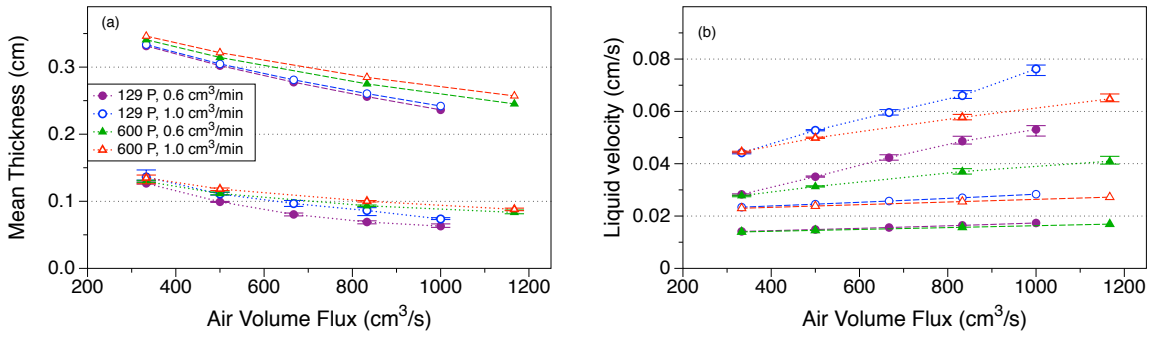

Figure 5.1.1: (a) Mean film thickness for various viscosities $\mu^{(l)}$, liquid fluxes $\bar{Q}^{(l)}$ and air fluxes $\bar{Q}^{(g)}$. Bars indicate range of values over several trials of each experiment. Dotted lines indicate trends in experimental data; dashed lines represent model predictions. (b) Mean liquid cross-sectional average velocities calculated using data in (a). Experiments conducted by Jeff Olander *et al.*.

This is achieved by the same means as in Chapter 2: the experiments progressed until a quasi-steady state was reached and the film thickness was calculated by weighing the wetted tube. The model was solved with some film thickness and allowed to progress until a quasi-steady state was reached. If the flux (averaged over the domain) was higher (lower) than that of the experiments, the mean thickness was decreased (increased) and the simulation run again. By repeating this procedure, a thickness was found that matched the experimental flux.

A comparison of the mean thicknesses predicted by the model with those of the experiments in Section 1.3 is displayed in Figure 5.1.1(a). The data show how exchange of momentum between air and liquid flow is qualitatively captured by the model. However, while there is some improvement over the exact solution's predictions (compare to Figure 1.3.3), the model still consistently overpredicts the film thickness. One explanation for this deficiency is that the turbulent closure assumes the free surface (seen as a rigid wall by the airflow) is flat, hence its value may be too low for these experiments with a wavy air-liquid interface.

As discussed near the end of Chapter 4 one remedy for this issue is to boost the viscosity. We briefly examine how increasing the viscosity may improve the quantitative agreement between the model and experiments. Data from a previous study [5] suggest using a phenomenologically

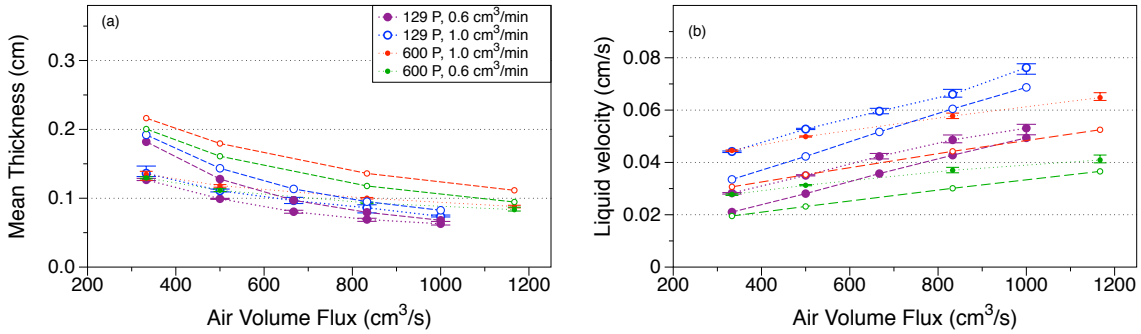

Figure 5.1.2: (a) Comparison of mean thickness predicted by the model with modified effective viscosity (dashed lines) with those of the experiments (dotted lines) described in Section 1.3. (b) Mean liquid cross-sectional average velocities calculated using data in (a). Experiments conducted by Jeff Olander *et al.*

modified effective viscosity

$$\mu_{eff}^{(g)} = \left(\frac{\mu^{(l)}}{\mu^{(g)}}\right)^{1/5} 0.0791 \frac{(Re_D)^{3/4}\mu^{(g)}}{16}. \tag{5.1.1}$$

This relationship is suggested purely by comparison with a subset of three points of the experimental data in Figure 5.1.1(a). All other points in the data set also closely follow this law, see [5] for further details. When the model simulations are repeated using this modified effective viscosity, the model predicts thicknesses and mean liquid speeds much closer to those seen in the experiments. Figure 5.1.2 shows results for $\mu^{(l)} = 129$ P; results were similar for $\mu^{(l)} = 600$ P. Comparing these results with Figure 5.1.1 shows the improvement in quantitative agreement is significant. Unfortunately, while this agreement shows the model can offer predictive insight, the improvement in mean thickness is offset by less accurate quantification of other properties, as the discussion at the end of Chapter 4 alluded to. Specifically it will be shown that the model's ability to predict mass transport by the waves is further eroded by this modified effective viscosity.

The mean speed and wavelength of the waves that develop in each simulation and experiment are tracked, see [4] for more information on the procedure. A comparison between model predictions and experiments is shown in Figure 5.1.3 using the modified effective viscosity. The trend in wave speed is qualitatively captured, while the wavelength is not particularly well captured by the model.

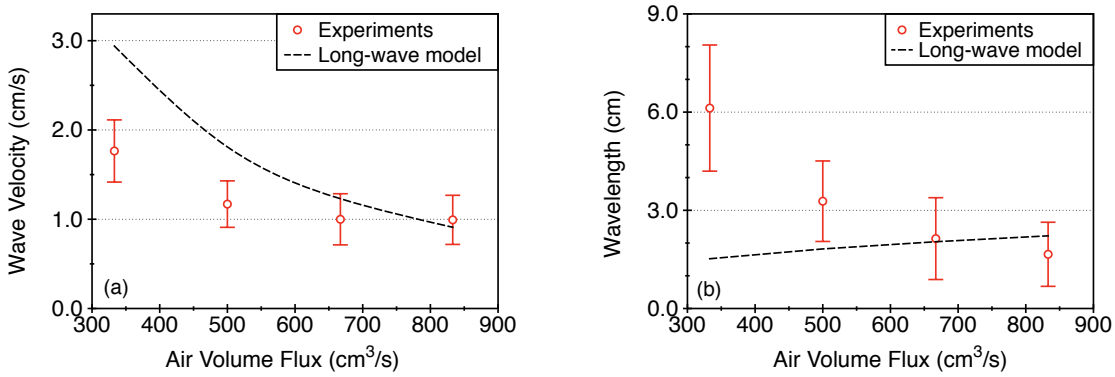

Figure 5.1.3: Mean values of wave (a) velocity and (b) wavelength with bars indicating one standard deviation. Dashed lines represent model predictions. $\bar{Q}^{(l)} = 1.0$ cm^3/min, $\mu^{(l)} = 129$ P. Experiments conducted by Jeff Olander *et al.*

In order to study the flow within the fluid film we once again move to a traveling reference frame, $Z = z - ct$, and seek traveling wave solutions. As before, there is now an ODE that must be satisfied:

$$[-c + S_1 f_1(R;a) + S_2(a) f_2(R;a)]R' + \frac{S_3}{R}\frac{d}{dZ}[f_3(R;a)(R' + R^2 R''')] = 0. \tag{5.1.2}$$

Solutions to (5.1.2) were found by letting solutions to (3.1.25) settle into a quasi-steady state. Using one pulse of these PDE solutions as an initial guess, the ODE solution was refined as described in Chapter 2.

The stream function is defined by the velocity gradients as in (4.3.1). Using the approximate expressions for u and w gives

$$\begin{aligned}\Psi = &\left[-\frac{S_1}{R^4} + \frac{S_2}{2} + \frac{4S_3}{R^2}(R_z + R^2 R_{zzz})\right]\left[\frac{1}{4r}(a^2 - r^2)^2\right] \\ &-[S_2 R^2 + 8S_3(R_z + R^2 R_{zzz})]\left[\frac{1}{4r}\left(a^2 - r^2 + 2r^2 \ln\frac{r}{a}\right)\right].\end{aligned} \tag{5.1.3}$$

Streamlines are plotted as before as isolines of Ψ within the annular fluid for a variety of parameter values. In the following comparisons, the experimental parameters and mean film thickness are changed in such a way that the liquid volume flux is held constant.

Two examples with identical liquid flux but differing capillary number and film thickness are shown in Figures 5.1.4 and 5.1.5. The parameter values for these solutions do not correspond

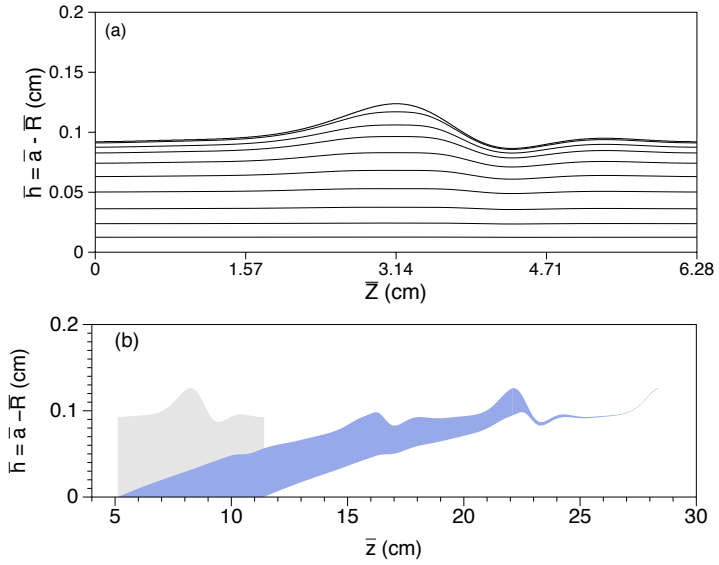

Figure 5.1.4: (a) Streamlines in the annular fluid phase for a traveling wave solution of model (3.1.25) with parameters $F = 3.39$, $S = 1.5$, $\bar{a} = 0.5$ cm, $a = 1.25$, $\bar{Q}^{(l)} = 3.2 \times 10^{-4}$cm/s. (b) Evolution of one wavelength of fluid during the interval $\bar{t} = (0, 5000)$ s.

to those in the experiment; these model results only show qualitative agreement with the experimental data. Further discussion of this quantitative discrepancy will be pursued below.

The fluid for the wave in Figure 5.1.4(a) flows along open streamlines only, while the wave in Figure 5.1.5(a) displays the presence of a trapped core; the red dashed line is the approximate location of a separatrix which connects two fixed points on the free surface and separates the trapped core from the underlying film flow. Figures 5.1.4(b) and 5.1.5(b) show the evolution of the fluid film in each flow. The lightly shaded area represents a region of the fluid film along one wavelength at an initial time. Particle trajectories were calculated for particles lying on the boundary of this region using the velocity field, and the location of the fluid area after a fixed elapsed time is shown by the darker, blue-shaded region. The very fastest particles in the shear wave flow (Figure 5.1.4(b)) have traveled almost exactly the same axial distance as the particles in the trapped core in Figure 5.1.5(b). However, any parcel of fluid in the shear wave regime is continuously thinning while stretching in the axial direction, so that the percentage of the fluid parcels reaching a certain location at a given time is much smaller than its trapped core counterpart, where the whole core keeps its volume and shape intact.

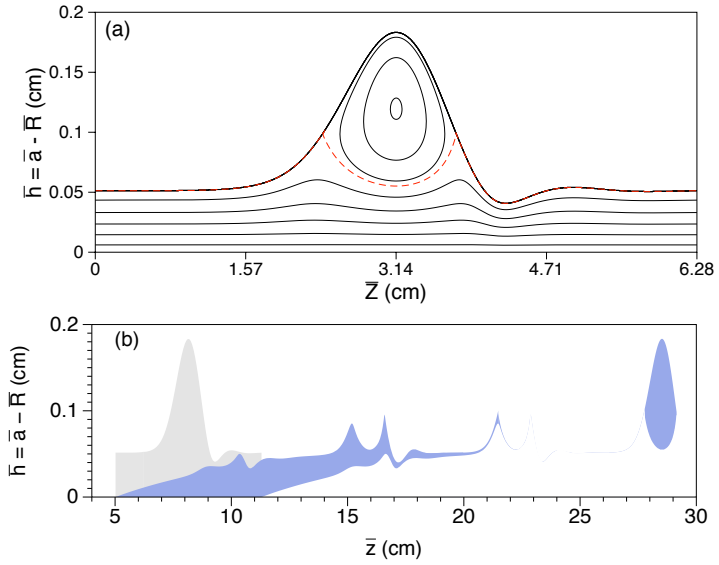

Figure 5.1.5: Same as Figure 5.1.4 but with $F = 4.36$, $S = 8.96$, $\bar{a} = 0.5$ cm, $a = 1.17$, $\bar{Q}^{(l)} = 3.2 \times 10^{-4}$cm/s. The dashed (red) streamline in (a) is close to a separating streamline.

This point is further illustrated in Figures 5.1.6 and 5.1.7. Here a sampling of fluid parcels throughout the fluid domain in Figures 5.1.4 and 5.1.5 were tracked over time, and their mean velocities with respect to time calculated. These mean velocities were then sorted, giving an equivalent shear velocity profile, i.e. a flat-interface shear flow with the plotted axial velocity profiles would be equivalent to the two traveling wave flows. In Figure 5.1.6(b) note the significant portion of fluid, corresponding to trapped cores, moving at a uniform speed faster than any particle for the shear wave case in Figure 5.1.6(a). Figure 5.1.7 displays the corresponding distribution as a histogram for the velocities shown in Figure 5.1.6. Note the presence of a trapped core is clearly revealed by the spike in velocity at exactly the speed of the wave in Figure 5.1.7(b), while no fluid parcels travel at the speed of the wave in Figure 5.1.7(a). The spike corresponds to the significant volume of fluid in the trapped core in Figure 5.1.5.

In order to be certain that waves like Figure 5.1.4(a) do not trap a core which is masked by under-resolution in the streamlines, the axial velocity of the fluid (relative to the wave velocity) is plotted as a function of r along one radial slice through the wave crest of Figures 5.1.4(a) and 5.1.5(a). Figure 5.1.8 shows the velocity profile corresponding to Figures 5.1.4(a) and 5.1.5(a). For the shear wave in Figure 5.1.4(a), the velocity is negative throughout the fluid

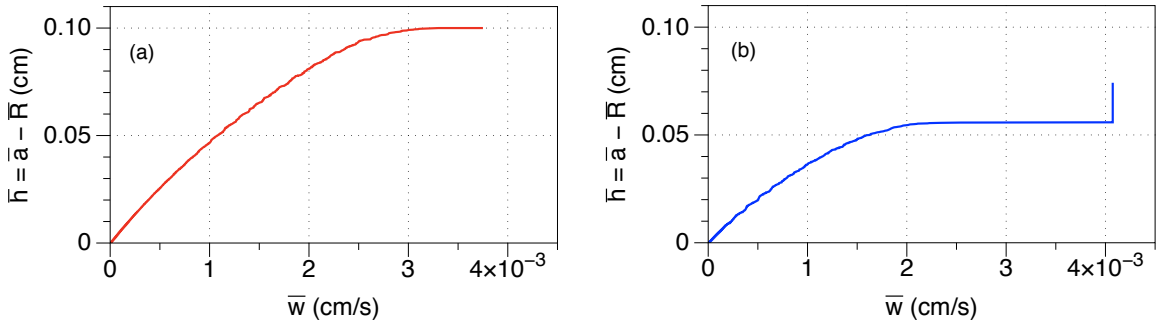

Figure 5.1.6: The flat-interface shear velocity profile equivalent to that of (a) Figure 5.1.4(a) and (b) Figure 5.1.5(a).

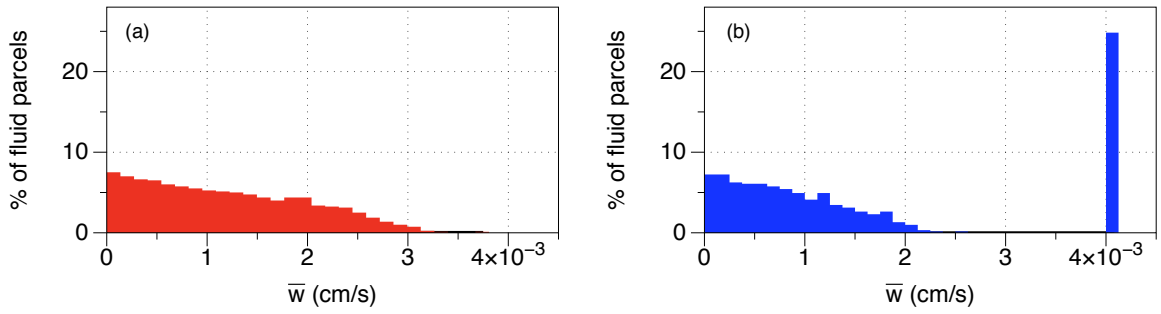

Figure 5.1.7: The distribution of velocities used to construct the shear profiles depicted in Figure 5.1.6.

layer, indicating that a trapped core cannot exist as discussed in Chapter 4. For the mass transport wave in Figure 5.1.5(a), the velocity changes signs at the stagnation point, clearly indicating the existence of a trapped core. See [51] for further discussion of dynamical systems and bifurcations relevant to the topological change of streamline patterns seen here. Note that the shear wave's velocity profile close to the interface very nearly approaches the speed of the wave, so that a very small change in capillary number would result in the formation of a trapped core.

In order to determine whether the mass transport behavior occurs in the experiments, a second series of experiments was designed and implemented by Jeff Olander in the Joint UNC Fluids Lab. A thorough description of the experimental setup and results can be found in [4]; a brief synopsis is given here. The air-oil experiment was repeated, but once the oil had wetted

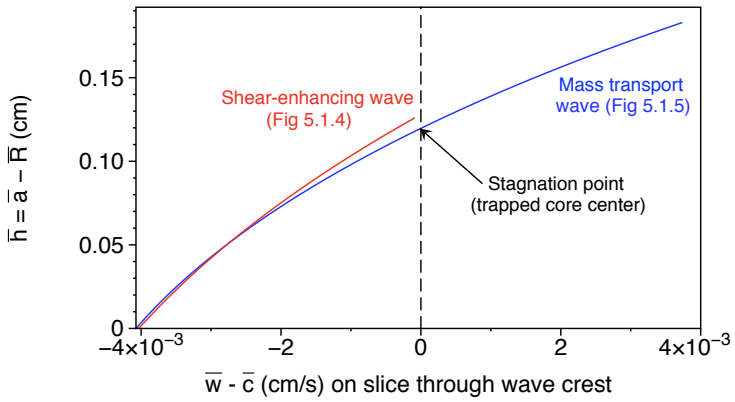

Figure 5.1.8: Liquid parcel axial velocities (measured in the traveling wave reference frame) along radial slices through the wave crest of Figures 5.1.4(a) and 5.1.5(a).

half the tube, the tube was removed from the clear oil chamber and placed on top of a chamber containing oil dyed blue. The blue oil was then fed into the tube. If most of the waves are mass-transport waves which trap a significant core, some blue oil should be transported directly to the wetting front. If, on the other hand, most of the waves are shear-enhancing waves, the blue oil should simply displace the clear oil upwards (with some mixing).

Figure 5.1.9 shows the location of each regime in parameter space for a sample fixed thickness and wavelength. As S or F decreases, the amplitude of a traveling wave solution decreases, and solutions trap a smaller core and eventually none at all. It was found that the experiments show the same trend as the model, i.e. for increasing S (which was achieved by decreasing the air volume flux) the waves trap more fluid. Quantitative agreement between experiments and model was found lacking, however. Parameter values corresponding to a sample experiment with various air viscosities, including the modified effective viscosity, are shown; parameters corresponding to Figure 5.1.4 are also shown. For this experiment (and all experiments conducted) the model predicts waves which are well inside the shear wave regime. It should also be noted that for large values of F, larger than those shown here, gravity dominates effects from the airflow and upward-moving traveling wave solutions give way to downward-moving solutions. These solutions exhibit the same type of bifurcation, where some combinations of parameter values result in mass transport waves while others result in shear waves.

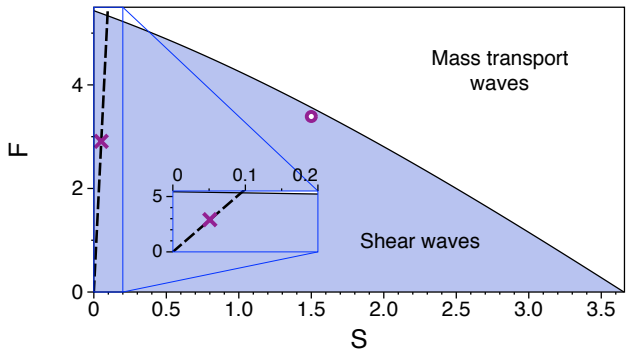

Figure 5.1.9: Mass transport and shear wave regimes for traveling wave solutions with fixed $\bar{a} = 0.5$ cm, $a = 1.25$ and $\bar{\lambda} = 2\pi$ cm. Values of S and F which correspond to the experimental parameters $\mu^{(l)} = 129$ P, $\bar{Q}^{(l)} = 0.6$ cm^3/min, $\bar{Q}^{(g)} = 667$ cm^3/s and various air viscosities are indicated by the dashed line; the modified effective viscosity is indicated by the purple 'x'. Parameter values corresponding to Figure 5.1.4 are indicated by the purple 'o'.

5.2. Wavy channel flow

As described in the previous section, the cause of the long-wave model's inability to quantitatively match experiments appears to be due to incorrect modeling of the free surface stress. In the long-wave model (3.1.25) the free surface stress rises and falls with the free surface itself, i.e. the stress is highest where the core is most constricted. This behavior of the stress being in phase with the free surface is not seen in experiments of air flowing through a wavy channel or pipe; rather, there is a phase shift so that the stress is highest prior to the point of maximal constriction, in regions where the airflow is becoming more constricted [27; 26; 76; 85]. In this section and the next, improvements to the free surface stress modeling are sought; the flat geometry of a wavy channel is considered here and the cylindrical geometry of a wavy pipe is considered in the next section.

As discussed in Chapter 3, the flow of air is fast enough that it is expected the air essentially sees the free surface as a rigid wall. The flow of a fluid over a wavy wall has been well studied in the flat geometry both experimentally and theoretically. Miles and Benjamin both modeled the flow of air over a rigid wavy wall using small-amplitude asymptotics and assuming the primary flow is quasi-laminar [54; 2]. Benjamin utilized curvilinear coordinates to transform streamlines into flat lines; his analysis found a phase shift of $\pi/6$ for the wall stress.

Thorsness *et al.*incorporated the leading order Reynolds stress into the quasi-laminar model of Benjamin, using a different set of curvilinear coordinates [76]. Several experiments [85; 76] were conducted during the 1970's to which these models were compared. The modeling was re-examined recently by Tseluiko & Kalliadasis who combined the curvilinear coordinates of Benjamin with the Reynolds stress modeling of Thorsness [79]; their analysis was compared to the experiments from the 1970's as well.

Experiments and modeling of flow of a fluid through a rigid wavy pipe appear to be fewer in number. Hsu & Kennedy performed experiments with airflow at high Reynolds numbers ($Re \approx 10^5$) through a wavy pipe [27; 26]. These experiments, like their flat-geometry counterparts, show a phase shift in the wall stress. They derive a model dependent on the free surface and its first two derivatives empirically using the results of their experiments.

None of these modeling approaches is entirely satisfactory for the problem considered here. As we are interested in the flow over an order of magnitude of Reynolds numbers, all lower than those of Hsu & Kennedy's experiments, an empirical model as in [26] seems less than ideal. The small-amplitude asymptotic approach relies on the amplitude of the wall (free surface) modulations being small relative to the mean core radius. This is not the case for our experiments described below, where the perturbations to the free-surface "wall" begin very small but can grow to have amplitude comparable to the mean radius of the core region. For such situations experiments show that the small-amplitude model is unable to quantitatively capture the phase shift in the tangential stress; this will be further discussed below.

The free surface waves seen in our experiments are not of small amplitude but they are relatively long-wave. This suggests that, while the air is flowing through large-amplitude constrictions, they may be long-wave constrictions. Thus a new approach is described here utilizing a long-wave modeling approach. The new model is first developed in the flat geometry of airflow through a wavy channel and is compared with existing models and experiments in the literature.

Consider the flow of a single liquid through a wavy channel with mean channel half-width $\bar{L}_0$ and local half-width $\bar{L}(\bar{z})$. The governing equations are the steady incompressible Reynolds-averaged Navier-Stokes (RANS) equations

$$\begin{aligned}
\rho(\bar{u}\bar{u}_{\bar{x}} + \bar{w}\bar{u}_{\bar{z}}) &= -\bar{p}_{\bar{x}} + \mu^{(g)}\bar{u}_{\bar{x}\bar{x}} + \mu^{(g)}\bar{u}_{\bar{z}\bar{z}} + \bar{\tau}_{11x} + \bar{\tau}_{12z}, \\
\rho(\bar{u}\bar{w}_{\bar{x}} + \bar{w}\bar{w}_{\bar{z}}) &= -\bar{p}_{\bar{z}} + \mu^{(g)}\bar{w}_{\bar{x}\bar{x}} + \mu^{(g)}\bar{w}_{\bar{z}\bar{z}} + \bar{\tau}_{12x} + \bar{\tau}_{22z}, \\
\bar{u}_{\bar{x}} + \bar{w}_{\bar{z}} &= 0.
\end{aligned} \tag{5.2.1}$$

where $(\bar{u}, \bar{v}, \bar{w})$ are the time-averaged velocity components in the $(\bar{x}, \bar{y}, \bar{z})$ directions, $\bar{p}$ is the time-averaged pressure, and $\bar{\tau}_{ij}$ are the components of the Reynolds stress tensor. The channel flow is assumed to be 2D, i.e. $\bar{v} = \partial_{\bar{y}} = 0$. Here $\bar{z}$ points downstream along the channel wall and $\bar{x}$ points towards the wall from the center of the channel, i.e. $\bar{x} = 0$ corresponds to the center of the channel and $\bar{x} = -\bar{L}$ corresponds to the lower wall.

We assume that the normal Reynolds stresses are negligible, i.e. $\bar{\tau}_{11} = \bar{\tau}_{22} = 0$. We also adopt a turbulent viscosity model for the Reynolds shear stress $\bar{\tau}_{12}$, i.e.

$$\bar{\tau}_{12} = \bar{\mu}^*(\bar{x})\bar{w}_{\bar{x}}. \tag{5.2.2}$$

Next, the wall perturbations are assumed to be long-wave and the problem is nondimensionalized by a long-wave turbulent scale:

$$\begin{aligned}
x = \bar{x}/\bar{L}_c, \quad z = \epsilon\bar{z}/\bar{L}_c, \quad u = \epsilon\bar{u}/w^*, \\
w = \bar{w}/w^*, \quad p = \epsilon\bar{p}/|T_w|, \quad \tau = \bar{\tau}/|T_w|,
\end{aligned} \tag{5.2.3}$$

where $\bar{L}_c = \mu^{(g)}/\rho w^*$ is the radial lengthscale, $w^* = \sqrt{|T_w|/\rho} = (\sqrt{C_f/2})\bar{Q}^{(g)}/2\bar{L}$ is the friction velocity ($C_f = 0.073Re_b^{-0.25}$ is the empirically determined skin friction coefficient by Dean's formula) and T_w is the wall stress through a flat channel with $|T_w| = \rho(w^*)^2 = \rho C_f(\bar{Q}^{(g)})^2/8\bar{L}^2$,

where $Re_b = \rho \bar{L} W_b / \mu^{(g)} = \rho \bar{Q}^{(g)} / 2\mu^{(g)}$. Substituting (5.2.3) and (5.2.2) into (5.2.1) gives

$$\begin{aligned} \epsilon^3(uu_x + wu_z) &= -p_x + \epsilon^2[u_{xx} + \epsilon^2 u_{zz} + (\mu^* w_x)_z], \\ \epsilon(uw_x + ww_z) &= -p_z + ([1 + \mu^*(x)]w_x)_x + \epsilon^2 w_{zz}, \\ u_x + w_z &= 0. \end{aligned} \tag{5.2.4}$$

The variables u, w, p and μ^* are expressed in a regular perturbation expansion

$$\begin{aligned} u &= u_0 + \epsilon u_1 + O(\epsilon^2), \\ w &= w_0 + \epsilon w_1 + O(\epsilon^2), \\ p &= p_0 + \epsilon p_1 + O(\epsilon^2), \\ \mu^* &= \mu_0^* + \epsilon \mu_1^* + O(\epsilon^2) \end{aligned} \tag{5.2.5}$$

and it is assumed that the turbulent viscosity can be modeled by the mixing-length model,

$$\begin{aligned} \mu^*(x) &= \mu_0^* + \epsilon \mu_1^* \\ &= l^2(w_{0x} + \epsilon w_{1x}), \end{aligned} \tag{5.2.6}$$

where the mixing length l is modeled by the van Driest equation

$$l = \kappa(L + x)[1 - \exp(-(L + x)/A)], \tag{5.2.7}$$

where $\kappa \approx 0.41$ is von Karman's constant, and $A = 26$ is an empirically determined constant. Typically the absolute value of the velocity gradient in (5.2.6) is taken; here w_{0x} is taken to be positive along the bottom wavy wall, and the first-order corrections to this gradient are assumed to be smaller than the leading-order gradient, thus no absolute value bars are needed. It is understood that if $\epsilon w_{1x} > w_{0x}$ we are outside the range of the model's validity.

Substituting (5.2.5) into (5.2.4) gives at leading order

$$\begin{aligned} p_{0x} &= 0, \\ p_{0z} &= ([1 + \mu_0^*(x)]w_{0x})_x, \\ u_{0x} + w_{0z} &= 0. \end{aligned} \tag{5.2.8}$$

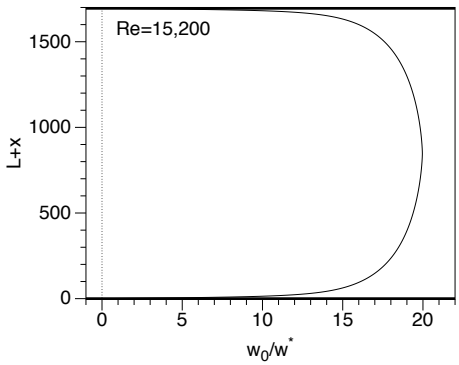

Figure 5.2.1: Leading-order axial velocity profile for air in channel flow for $Re = 15,200$.

For a given Reynolds number the leading-order nondimensional axial velocity profile w_0 is easily computed; Figure 5.2.1 shows the velocity profile for $Re = 15,200$.

Note that in flow through a wavy channel the Reynolds number, and hence the skin friction coefficient, remain fixed. Thus the channel half-width $\bar{L}$ varies with $\bar{z}$, but the nondimensional channel half-width remains constant $L = \bar{L}/\bar{L}_c = (\sqrt{C_f/2})\rho\bar{Q}^{(g)}/2\mu^{(g)}$. The nondimensional leading-order axial velocity profile and its transverse gradient thus do not vary with $L(z)$, but the dimensional velocity $\bar{w}_0$ depends on $\bar{L}(\bar{z})$:

$$\begin{aligned}\bar{w}_0(\bar{x},\bar{z}) &= w_0(\bar{x}/\bar{L}_c)w^*(\bar{z}) \\ &= w_0(x)\left(\sqrt{\frac{C_f}{2}}\right)\frac{\bar{Q}^{(g)}}{2\bar{L}(\bar{z})}, \qquad (5.2.9)\\ \bar{w}_{0\bar{x}}(\bar{x},\bar{z}) &= w_{0x}(\bar{x}/\bar{L}_c)\frac{w^*(\bar{z})}{\bar{L}_c} \\ &= w_{0x}(x)\frac{\rho C_f(\bar{Q}^{(g)})^2}{8\mu^{(g)}\bar{L}^2(\bar{z})}. \qquad (5.2.10)\end{aligned}$$

Likewise the streamwise velocity's streamwise gradient and cross-stream velocity are, in dimensional form,

$$\begin{aligned}\bar{w}_{0\bar{z}}(\bar{x},\bar{z}) &= [w_0(\bar{x}/\bar{L}_c)w^*(\bar{z})]_{\bar{z}} \\ &= \left(w_{0x}(x)\frac{C_f\rho(\bar{Q}^{(g)})^2(-x)}{8\mu^{(g)}L} - w_0(x)\sqrt{\frac{C_f}{2}}\frac{\bar{Q}^{(g)}}{2}\right)\frac{\bar{L}_{\bar{z}}}{\bar{L}^2}, \qquad (5.2.11)\\ \bar{u}_0 &= -\int_0^{\bar{x}} \bar{w}_{0\bar{z}}d\bar{x} \\ &= -\frac{\bar{L}_{\bar{z}}}{\bar{L}}\int_0^x \left(w_{0x}(x)\frac{\bar{Q}^{(g)}}{2}\sqrt{\frac{C_f}{2}}\left(\frac{-x}{L}\right) - w_0(x)\frac{\mu}{\rho}\right)dx. \qquad (5.2.12)\end{aligned}$$

At first-order the governing equations become

$$\begin{aligned} p_{1x} &= 0, \\ u_0w_{0x} + w_0w_{0z} + p_{1z} &= ([1+\mu_0^*(x)]w_{1x} + \mu_1^*(x)w_{0x})_x, \qquad (5.2.13)\\ u_{1x} + w_{1z} &= 0. \end{aligned}$$

The first-order correction $\bar{w}_1$ to the axial velocity profile is then computed numerically, again enforcing the zero-flux condition

$$0 = \int_0^{\bar{L}} \bar{w}_1 d\bar{x}, \qquad (5.2.14)$$

which determines the value of $\bar{p}_1$. With these values calculated, the wall stress to first-order is then

$$\begin{aligned}\bar{\tau} &= T_w + \mu^{(g)}\bar{w}_{1\bar{x}}|_{\bar{x}=-L} \\ &= \frac{0.073\rho(\bar{Q}^{(g)})^2}{8\bar{L}^2}\left(\frac{2\mu^{(g)}}{\rho\bar{Q}^{(g)}}\right)^{1/4} + \frac{C_1}{\bar{L}^2}\bar{L}_{\bar{z}}, \qquad (5.2.15)\end{aligned}$$

where C_1 is a numerically determined constant dependent on the flow and fluid parameters. Note that the stress depends on both the local radius and local wall gradient, in contrast to the stress as predicted in the locally Poiseuille model which depends only on the local radius.

A sketch of the streamwise velocity profile with first-order corrections for a small amplitude wavy wall is shown in Figure 5.2.2. In regions where the channel is constricting, i.e. $\bar{L}_{\bar{z}} < 0$, the air flows faster near the walls and slower at the center of the channel; where the channel widens,

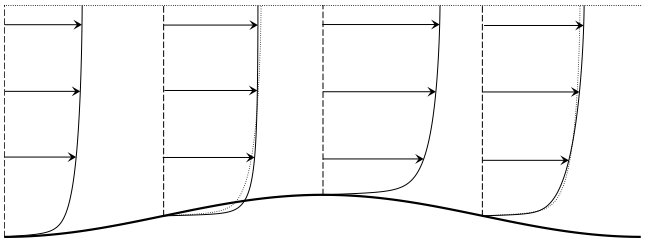

Figure 5.2.2: (a) Streamwise velocity profile for first-order long-wave (solid lines) and leading-order (dotted lines) models along one wavelength of a wavy channel (lower half of channel depicted, figure not to scale).

i.e. $\bar{L}_{\bar{z}} > 0$, the air flows faster near the walls. Thus as may be expected constriction results in larger wall stress while widening results in smaller wall stress. For larger amplitude walls, in the regions where the airflow is being constricted, i.e. $\bar{L}_{\bar{z}} < 0$, the maximum axial velocity occurs at a point close to the wall (not shown in Figure 5.2.2; this behavior is likely unphysical and was not seen in pipe and channel flow experiments; see, e.g., [27]). We note that the same behavior occurs in the small amplitude model, though the small amplitude model only exhibits this behavior for much larger wave amplitudes. Nevertheless, the interest here is whether the model accurately captures the near-wall behavior, in particular the wall stress; this behavior is now considered.

We now compare the resulting stress (5.2.15) with the small-amplitude model as in [79] and experiments reported in [85; 76]. Figure 5.2.3 shows results for increasing Reynolds number with fixed wall wave amplitude of 0.07 cm in a channel with half-width 2.54 cm. Both models match the experimental trend of smaller corrections relative to the magnitude of the leading-order stress for increasing Reynolds number. For the highest Reynolds number $Re = 31,000$ the long-wave model captures both the phase shift and amplitude of the waviness-induced wall stress better than the small-amplitude model and locally-Poiseuille model. For the lowest Reynolds number $Re = 7850$, the small-amplitude model appears to slightly underestimate the phase shift; the long-wave model slightly overestimates the phase shift. Both underestimate the amplitude of the waviness-induced stress; both models give much better agreement than the locally Poiseuille model.

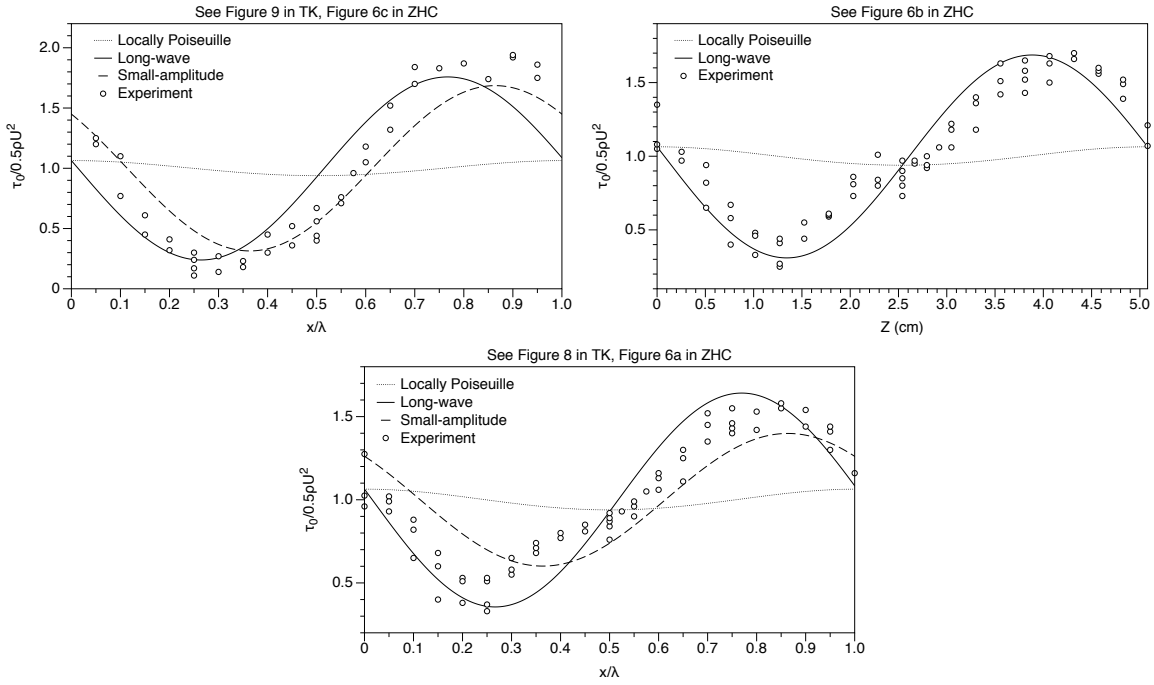

Figure 5.2.3: Wall stress along one wavelength predicted by the long-wave (solid lines), locally Poiseuille (dotted lines), and small-amplitude (dashed lines) models through a channel with half-width $\bar{L}_0 = 2.54$ cm and sinusoidally wavy wall with amplitude 0.079 cm. (a) $Re = 7850$, (b) $Re = 15,200$, (c) $Re = 31,000$; compare to Figures 8 & 9 in [79] and Figure 6 in [85].

Figure 5.2.4 shows results for increasing Reynolds number with higher fixed wall wave amplitude of 0.127 cm. Both models (small-amplitude not shown here) again exhibit the experimental trend of higher corrections relative to the magnitude of the leading-order stress for increased wave amplitude. The small-amplitude model, however, exhibits no phase shift for increased amplitude, while the long-wave model exhibits a small phase shift. For the smaller Reynolds number, the long-wave model estimates the amplitude of the corrections well; for the higher Reynolds number, the long-wave model appears to overestimate the amplitude while not capturing the phase shift.

The experiments in Figure 5.2.4 also indicate that the wall stress is nonlinear; notice the steeper sloped data points near $x/\lambda = 0$ and less steep data near $x/\lambda = 0.5$. This effect is of course not captured in the small-amplitude model which ignores nonlinear interactions in velocity perturbations. The long-wave model, through the dependence of $\tau^{(g)}$ on $1/\bar{L}^2$,

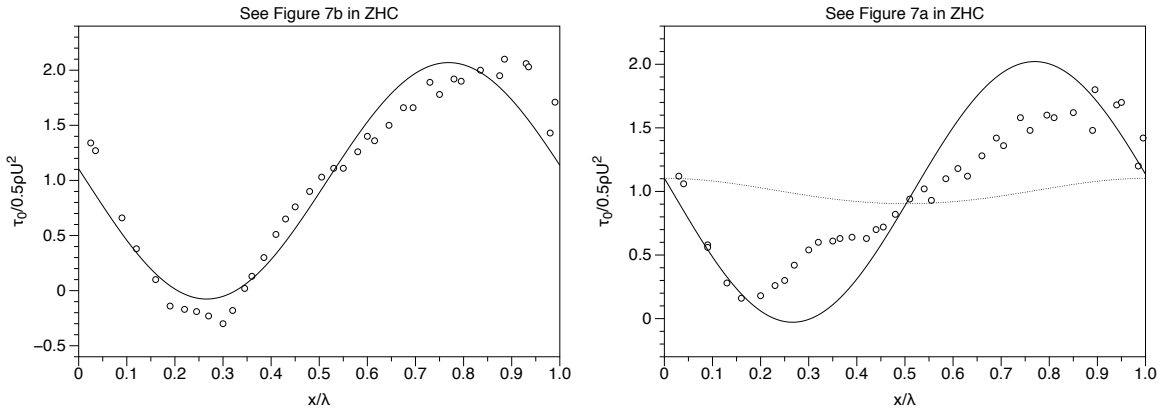

Figure 5.2.4: Same as Figure 5.2.3 but with wave amplitude 0.15 cm. (a) $Re = 19260$, (b) $Re = 31850$. Compare to Figure 7 in [85].

displays this nonlinear behavior in qualitative agreement with experiments, i.e. the first-order corrections are not strictly sinusoidal despite the sinusoidal wall.

It is also notable that in the experiments seen in Figure 5.2.4(a) a region of negative wall stress was observed; the long-wave model does not capture this behavior in these Figures, but does display this behavior for smaller Reynolds number (not shown). It is important to note that the long-wave model was derived under the assumption that the ratio of the characteristic velocity scales in the transverse and axial directions was small, $\bar{u}_c = \epsilon \bar{w}_c$. In these regions of negative stress, this assumption is violated.

Before proceeding to wavy pipe flow, a very brief description will be given of other modeling approaches which were considered by the author. The small-amplitude model in [79] was considered under the long-wave asymptotic limit, i.e. their equation (3.34) was truncated at $O(\alpha)$. The results varied significantly even for moderately small α, say $\alpha = O(10^{-3})$ from those of the full equation; the term $2i\alpha^2\psi_0' e^{-\alpha\xi_2}\psi_0''$ plays a significant role. This term arises from the use of curvilinear coordinates, and inclusion of this term allows the simplified equation to give good agreement with the full equation (3.34). However, due to the questionable validity of applying the small-amplitude assumption to our experiments and the improved agreement with wavy-channel flow experiments offered by the long-wave model, the small-amplitude model will not be pursued further here.

Another model considered is derived in Appendix B. There the locally-Poiseuille approach is extended to get first-order corrections. Overall, reasonable agreement with experiments is seen, though not as good as the model derived above. The model has an interesting shortcoming in that the ratio of the amplitude of first-order stress corrections to the magnitude of the leading-order stress has no dependence on the Reynolds number. These limitations, in addition to the questionable assumptions used in the derivation, ultimately lead us to primarily consider the approach developed above.

5.3. Wavy pipe flow

Having seen that the first-order long-wave model offers dramatic improvement over the locally Poiseuille model and minor improvement over the small-amplitude model in predicting the shear stress along a wavy channel wall, this model is now adapted to the cylindrical geometry of a wavy pipe with mean radius $\bar{R}_0$ and local radius $\bar{R}(\bar{z})$. The governing equations are the RANS in cylindrical coordinates (neglecting the Reynolds normal stresses and assuming a turbulent viscosity model for the Reynolds shear stresses as in the previous section):

$$\begin{aligned}
\rho(\bar{u}\bar{u}_{\bar{r}} + \bar{w}\bar{u}_{\bar{z}}) &= -\bar{p}_{\bar{r}} + \mu^{(g)}\left(\frac{1}{\bar{r}}\partial_{\bar{r}}(\bar{r}\bar{u}_{\bar{r}}) + \bar{u}_{\bar{z}\bar{z}} - \frac{\bar{u}^2}{\bar{r}}\right) + (\mu^*\bar{w}_{\bar{r}})_{\bar{z}}, \\
\rho(\bar{u}\bar{w}_{\bar{r}} + \bar{w}\bar{w}_{\bar{z}}) &= -\bar{p}_{\bar{z}} + \mu^{(g)}\left(\frac{1}{\bar{r}}\partial_{\bar{r}}(\bar{r}\bar{w}_{\bar{r}}) + \bar{w}_{\bar{z}\bar{z}}\frac{1}{\bar{r}}\right) + \frac{1}{\bar{r}}\partial_{\bar{r}}(\mu^*\bar{r}\bar{w}_{\bar{r}}), \\
\frac{1}{\bar{r}}\partial_{\bar{r}}(\bar{r}\bar{u}) + \bar{w}_{\bar{z}} &= 0.
\end{aligned} \tag{5.3.1}$$

Once again we nondimensionalize and expand the flow variables as in (5.2.5), and it is again assumed that the turbulent viscosity can be modeled by the mixing-length model,

$$\mu^* = \mu_0^* + \epsilon\mu_1^* \tag{5.3.2}$$

$$= l^2(w_{0r} + \epsilon w_{1r}), \tag{5.3.3}$$

where the mixing length l is again modeled by the van Driest equation

$$l = \kappa(R - r)[1 - \exp(-(R - r)/A)]. \tag{5.3.4}$$

Taking $\epsilon \to 0$ gives the leading order equations:

$$p_{0r} = 0, \tag{5.3.5}$$

$$p_{0z} = \frac{1}{r}([1 + \mu_0^*(r)]rw_{0r})_r, \tag{5.3.6}$$

$$\frac{1}{r}\partial_r(ru_0) + w_{0z} = 0. \tag{5.3.7}$$

These can be solved numerically to find the leading-order velocity profile as in Section 5.2 for channel flow. Note that unlike flow through a wavy channel, the flow now has Reynolds number that varies with pipe radius, $Re = \rho\bar{Q}^{(g)}/\pi\mu^{(g)}\bar{R}$; as a result, the leading-order axial velocity profile varies as well. Also note that the skin-friction coefficient for pipe flow is given by $C_f = 0.079Re^{-0.25}$ from which the leading-order wall stress can be approximated, $\bar{T}_w = C_f\rho\bar{w}_b^2/2 = \frac{0.079\rho(\bar{Q}^{(g)})^2}{2\pi^2\bar{R}^4}(\frac{\rho\bar{Q}^{(g)}}{\pi\mu\bar{R}})^{-1/4}$.

At $O(\epsilon)$ the governing equations are

$$p_{1r} = 0, \tag{5.3.8}$$

$$u_0w_{0r} + w_0w_{0z} + p_{1z} = \frac{1}{r}([1 + \mu_0^*(r)]rw_{1r} + \mu_1^*(r)rw_{0r})_r, \tag{5.3.9}$$

$$\frac{1}{r}\partial_r(ru_1) + w_{1z} = 0. \tag{5.3.10}$$

The leading order axial velocity w_0 and its radial gradient w_{0r} were found above; these allow calculation of w_{0z} and u_0 as in Section 5.2. With these values computed, $\bar{w}_1$ can be solved for numerically assuming for the moment that $\bar{R}$ can be approximated by the mean pipe radius $\bar{R}_0$ and enforcing the zero-flux condition

$$0 = \int_0^{\bar{R}} \bar{r}\bar{w}_1 d\bar{r}, \tag{5.3.11}$$

which again determines the value of $\bar{p}_1$. An iterative approach is used to find the values of $\bar{w}_1$ and μ_1^* and the wall stress is

$$\begin{aligned}\bar{\tau} &= \bar{T}_w + \mu^{(g)}\bar{w}_{1\bar{r}}|_{\bar{R}} \\ &= \frac{\bar{C}_0}{\bar{R}^{15/4}} + \frac{\bar{C}_1}{\bar{R}^{19/4}}\bar{R}_{\bar{z}}.\end{aligned} \tag{5.3.12}$$

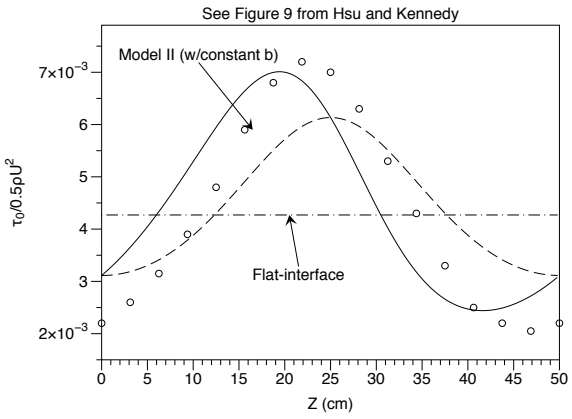

Figure 5.3.1: Comparison of locally-Poiseuille (dashed line) and long-wave (solid line) model predictions of wall shear stress with experiments in [27]. $Re = 90,000$, $\bar{a} = 0.552$ cm.

Once again we compare the model predictions for the wall stress with experiments. Two sinusoidally-varying pipes were used in [27] with different amplitudes, and air was forced to flow at two different Reynolds numbers. Figure 5.3.1 shows a comparison of the model with two of the parameter settings from [27]. The long-wave model captures well the amplitude of the stress corrections, though overstates the phase shift by a considerable amount. The reasons why the model accurately captures the behavior of wavy channel flow experiments in Section 5.2 but not those here are not immediately clear, but could be due to a number of factors. Note, for example, that both the Reynolds number and wave amplitude of the wavy pipe flow experiments are considerably higher than those of the channel flow experiments. Nevertheless, the model appears to be an improvement over the locally-Poiseuille model in all cases, and it will next be incorporated into the liquid model.

5.4. Liquid modeling

Having derived an approximate expression for the free surface stress, we return to modeling the film flow. The governing equations are again the axisymmetric Navier-Stokes equations in cylindrical coordinates (1.2.1) which are non-dimensionalized using the scalings

$$r = \bar{r}/\bar{h}_0, \quad z = \bar{z}/\bar{\lambda}, \quad u = \bar{u}/\bar{U}_0, \quad w = \bar{w}/\bar{W}_0,$$

$$t = \bar{t}\bar{W}_0/\bar{\lambda}, \quad p^{(l),(g)} = \epsilon\bar{p}^{(l),(g)}\bar{h}_0/(\mu^{(l)}\bar{W}_0), \quad \tau = \bar{\tau}^{(g)}\bar{h}_0/(\mu^{(l)}\bar{W}_0), \tag{5.4.1}$$

where $\bar{h}_0$ is the film's mean thickness, $\bar{W}_0 = g\bar{h}_0^2\rho^{(l)}/\mu^{(l)}$ is the axial velocity scale, and $\bar{U}_0 = \epsilon\bar{W}_0$ is the radial velocity scale as determined by the continuity equation. We again consider the long-wave case where $\epsilon = \bar{h}_0/\bar{\lambda} \ll 1$. This yields

$$\epsilon^3 Re^{(l)}(u_t + uu_r + wu_z) = -p_r + \epsilon^2\left(\frac{1}{r}\partial_r(ru_r) + \epsilon^2 u_{zz} - \frac{u}{r^2}\right), \tag{5.4.2}$$

$$\epsilon Re^{(l)}(w_t + uw_r + ww_z) = -p_z + \frac{1}{r}\partial_r(rw_r) + \epsilon^2 w_{zz} + 1, \tag{5.4.3}$$

$$\frac{1}{r}\partial_r(ru) + w_z = 0, \tag{5.4.4}$$

where $Re^{(l)} \equiv \bar{\rho}^{(l)}\bar{W}_0\bar{h}_0/\bar{\mu}^{(l)}$ is the liquid Reynolds number.

Boundary conditions at the wall ($r = a$) are given by

$$u = w = 0, \tag{5.4.5}$$

and at the interface ($r = R(z,t)$) by

$$w_r + O(\epsilon^2) = \tau^{(g)}, \tag{5.4.6}$$

$$-p^{(l)} + O(\epsilon^2) = -p^{(g)} + \frac{\epsilon}{C}\left(\frac{1}{R} - \epsilon^2 R_{zz}\right), \tag{5.4.7}$$

$$w = R_t + uR_z. \tag{5.4.8}$$

As in Chapters 2 & 3, integrating the continuity equation across the annular-sectional area of the liquid and using (5.4.8) yields the layer-mean equation

$$R_t - \frac{1}{R}\frac{\partial}{\partial z}\int_R^a wr dr = 0, \tag{5.4.9}$$

for the interface location. Once again we seek an approximate solution for w so that the system can be closed and reduced to a single evolution equation for the interface location.

Let $u, w, p^{(l)}$ and $\tau^{(g)}$ be expanded as

$$u = u_0 + \epsilon u_1 + ...,$$

$$w = w_0 + \epsilon w_1 + ..., \tag{5.4.10}$$

$$p^{(l)} = p_0^{(l)} + \epsilon p_1^{(l)} + ..., \tag{5.4.11}$$

$$\tau^{(g)} = \tau_0^{(g)} + \epsilon\tau_1^{(g)} + ...$$

Then the leading order equations are given by

$$\frac{1}{r}\partial_r(r\partial_r w_0) = 1 + \partial_z p_0^{(l)}, \quad \partial_r p_0^{(l)} = 0, \quad \partial_r(ru_0) = -r\partial_z w_0. \tag{5.4.12}$$

Boundary conditions at the wall ($r = a$) are given by

$$u_0 = w_0 = 0, \tag{5.4.13}$$

and at the interface ($r = R(z,t)$) by

$$\partial_r w_0 = \tau_0^{(g)}, \tag{5.4.14}$$

$$p_0^{(l)} = p_0^{(g)}. \tag{5.4.15}$$

This gives a leading-order solution for the axial velocity

$$w_0 = (r^2 - a^2)\left(\frac{1 + p_{0z}^{(g)}}{4}\right) + \left(R\tau_0^{(g)} - \frac{R^2}{2}(1 + p_{0z}^{(g)})\right)\ln\frac{r}{a}. \tag{5.4.16}$$

At this point, we approximate the leading-order stress $\tau_0^{(g)}$ imparted by the gas flow at the interface using $\bar{\tau}_0^{(g)}$ found in the previous section (here nondimensionalized by the liquid scalings):

$$\tau_0^{(g)} = -\frac{C_0}{R^{15/4}}, \tag{5.4.17}$$

where

$$C_0 = -\frac{0.0791\rho^{(g)}(\bar{Q}^{(g)})^2}{2\pi^2\rho^{(l)}g\bar{h}_0}\left(\frac{2\rho^{(g)}\bar{Q}^{(g)}}{\pi\mu^{(g)}}\right)^{-1/4}. \tag{5.4.18}$$

Note that the leading order pressure gradient is given by

$$p_{0z}^{(g)} = \frac{2\tau_0^{(g)}}{R} = \frac{2C_0}{R^{19/4}}. \tag{5.4.19}$$

The leading order solution is given by:

$$w_0 = \frac{1}{4}\left[(r^2 - a^2)\left(1 - \frac{2C_0}{R^{19/4}}\right) - 2R^2\ln\frac{r}{a}\right], \tag{5.4.20}$$

$$u_0 = \left[\left(\frac{r^3}{4} - \frac{a^2 r}{2}\right)\left(\frac{19C_0}{2R^{23/4}}\right) - R\left(\frac{r}{2}\ln\frac{r}{a} - \frac{r}{4}\right)\right]R_z. \tag{5.4.21}$$

The leading-order flux at any point is found to be

$$q_0 = \int_R^a w_0 r dr \tag{5.4.22}$$

$$= \left(\frac{r^4}{16} - \frac{a^2 r^2}{8}\right)\left(1 - \frac{2C_0}{R^{19/4}}\right) - \frac{R^2}{2}\left(\frac{r^2}{2}\ln\frac{r}{a} - \frac{r^2}{4}\right)\Bigg|_R^a \tag{5.4.23}$$

$$= -\frac{1}{16}(R^2 - a^2)^2\left(1 - \frac{2C_0}{R^{19/4}}\right) - \frac{R^2}{8}\left(R^2 - a^2 - 2R^2\ln\frac{R}{a}\right). \tag{5.4.24}$$

The leading-order model (5.4.9) is then:

$$R_t = \frac{1}{R}\partial_z q_0 \tag{5.4.25}$$

$$= \frac{1}{2}\left[a^2 - R^2 + 2R^2\ln\frac{R}{a} + \frac{C_0}{16}\left(-\frac{3}{R^{7/4}} + \frac{22a^2}{R^{15/4}} - \frac{19a^4}{R^{23/4}}\right)\right]R_z. \tag{5.4.26}$$

The $O(\epsilon)$ equations are

$$\frac{1}{r}\partial_r(r\partial_r w_1) = Re^{(l)}(\partial_t w_0 + u_0\partial_r w_0 + w_0\partial_z w_0) + \partial_z p_1^{(l)}, \tag{5.4.27}$$

$$\partial_r p_1^{(l)} = 0, \tag{5.4.28}$$

$$\frac{1}{r}\partial_r(r u_1) + \partial_z w_1 = 0. \tag{5.4.29}$$

Since the liquid is highly viscous and $Re^{(l)} = O(10^{-2})$ at most, we are primarily interested in the case where we neglect the inertial terms in (5.4.27); see Appendix A for the case where these terms are not neglected (where only leading-order free surface stress is included for simplicity). Our first-order equation for w_1 then becomes

$$\frac{1}{r}\partial_r(r\partial_r w_1) = \partial_z p_1^{(l)}. \tag{5.4.30}$$

Boundary conditions at the wall ($r = a$) are given by

$$u_1 = w_1 = 0, \tag{5.4.31}$$

and at the interface ($r = R(z,t)$) by

$$\partial_r w_1 = \tau_1^{(g)}, \tag{5.4.32}$$

$$p_1^{(l)} = p_1^{(g)} - \frac{1}{C}\left(\frac{1}{R} - \epsilon^2 R_{zz}\right). \tag{5.4.33}$$

We use the approximation of $\tau_1^{(g)}$ and $p_{1z}^{(g)}$ from above (nondimensionalized by the new scalings):

$$\tau_1^{(g)} = \frac{C_1}{R^{19/4}} R_z, \quad p_{1z}^{(g)} = \frac{C_2}{R^{23/4}} R_z, \tag{5.4.34}$$

where $\bar{C}_1$ and $\bar{C}_2$ were found numerically in the previous section and have been rescaled here to match the fluid scalings.

The solution to (5.4.30) - (5.4.33) is

$$\begin{aligned} w_1 = &\frac{1}{4}\left[\frac{C_2}{R^{23/4}} R_z + \frac{1}{C}\left(\frac{R_z}{R^2} + \epsilon^2 R_{zzz}\right)\right](r^2 - a^2) \\ &+\left[\frac{C_1}{R^{15/4}} R_z - \frac{1}{2}\left(\frac{C_2}{R^{15/4}} R_z + \frac{1}{C}(R_z + \epsilon^2 R^2 R_{zzz})\right)\right] \ln \frac{r}{a}. \end{aligned} \tag{5.4.35}$$

The first-order long-wave model can then be written as:

$$\begin{aligned} R_t = &\frac{1}{2}\left[a^2 - R^2 + 2R^2 \ln \frac{R}{a} + \frac{C_0}{16}\left(-\frac{3}{R^{7/4}} + \frac{22a^2}{R^{15/4}} - \frac{19a^4}{R^{23/4}}\right)\right] R_z \\ &+\frac{\epsilon}{R}\frac{\partial}{\partial z}\left[\left(\frac{C_2}{R^{23/4}} R_z + \frac{1}{C}\left(\frac{R_z}{R^2} + \epsilon^2 R_{zzz}\right)\right)\left(-\frac{3}{16}R^4 + \frac{1}{4}a^2 R^2 - \frac{1}{16}a^4 + \frac{1}{4}R^4 \ln \frac{R}{a}\right)\right. \\ &\left.+\frac{C_1}{R^{15/4}} R_z \left(\frac{R^2}{4} - \frac{a^2}{4} - \frac{R^2}{2} \ln \frac{R}{a}\right)\right]. \end{aligned}$$

Expressed in the original aspect ratio and more succinctly, the model is

$$\begin{aligned} R_t = &[\tilde{S}_0 \tilde{f}_0(R;a) + \tilde{f}_1(R;a)] R_z \\ &+\frac{1}{R}[\tilde{S}_2 \tilde{f}_2(R;a)(R_z + R^2 R_{zzz}) + \tilde{S}_6 R^{-15/4} \tilde{f}_1(R;a) R_z + \tilde{S}_7 R^{-23/4} \tilde{f}_2(R;a) R_z]_z, \end{aligned} \tag{5.4.36}$$

where

$$\begin{aligned} \tilde{f}_0(R;a) &= -\frac{3}{R^{7/4}} + \frac{22a^2}{R^{15/4}} - \frac{19a^4}{R^{23/4}}, \\ \tilde{f}_1(R;a) &= \frac{1}{2}[R^2 - a^2 - 2R^2 \ln(R/a)], \\ \tilde{f}_2(R;a) &= -\frac{a^4}{R^2} + 4a^2 - 3R^2 + 4R^2 \ln \frac{R}{a}, \end{aligned} \tag{5.4.37}$$

and the $\tilde{S}_i$ are given by

$$\tilde{S}_0 = \frac{C_0}{32}, \quad \tilde{S}_2 = \frac{1}{16C}, \quad \tilde{S}_6 = \frac{C_1}{2}, \quad \tilde{S}_7 = C_2. \tag{5.4.38}$$

Note that unlike in [79] no assumption of large pipe radius (analogous to large channel half-width) was made in the derivation of (5.4.36). Note also that the long-wave model depends

only on the local tube radius and its gradients in contrast to the small-amplitude model which relies on a Fourier decomposition of the free surface.

5.5. Linear stability analysis

We now study the new model equation by introducing an infinitesimal perturbation to the interface,

$$R = (a-1) + A\exp[i(kz - \omega t)], \tag{5.5.1}$$

where $A \ll a-1$ is the amplitude of the disturbance, k is its real wavenumber, $\mathrm{Re}[\omega]/k$ is its phase speed, and $\lambda = \mathrm{Im}[\omega]$ is its growth rate. Substituting (5.5.1) into (5.4.36) and neglecting higher order terms in A gives the dispersion relations

$$\begin{aligned}\omega_L = &\left[\frac{1}{2}\left(a^2 - (a-1)^2 - 2(a-1)^2\ln\frac{a}{a-1}\right)\right.\\ &\left.+S_0\left(-\frac{3}{(a-1)^{7/4}} + \frac{22a^2}{(a-1)^{15/4}} - \frac{19a^4}{(a-1)^{23/4}}\right)\right]k\\ &+i\left\{S_2(a-1)^3\left[\left(\frac{a}{a-1}\right)^4 - 4\left(\frac{a}{a-1}\right)^2 + 3 + 4\ln\frac{a}{a-1}\right]\left[\frac{k^2}{(a-1)^2} - k^4\right]\right.\\ &-\frac{S_6}{2(a-1)^{15/4}}\left[(a-1)^2 - a^2 - 2(a-1)^2\ln\frac{a-1}{a}\right]k^2\\ &\left.-\frac{S_7}{(a-1)^{15/4}}\left[\left(-\frac{a}{a-1}\right)^4 + 4\left(\frac{a}{a-1}\right)^2 - 3 + 4\ln\frac{a-1}{a}\right]k^2\right\}\end{aligned} \tag{5.5.2}$$

The effect of the airflow is now felt in both the real and imaginary components of the dispersion relation (5.5.2); in the locally Poiseuille model the airflow only affected the real part. The first-order stress corrections contribute to long-wave instability growth and alter the wavelength of maximum growth rate. This wavelength now depends on the airflow properties as captured by S_6 and S_7:

$$k_m = \sqrt{\frac{1}{2(a-1)^2} - \frac{S_6(a-1)^2\tilde{f}_1(a-1;a) + S_7\tilde{f}_2(a-1;a)}{2S_2(a-1)^{35/4}\tilde{f}_2(a-1;a)}}, \tag{5.5.3}$$

where if $S_6 = S_7 = 0$ the gravity-driven and locally Poiseuille result is recovered. If S_6 and S_7 are nonzero k_m is less than its value in gravity-driven flow, i.e. the wavelength of maximum growth rate is shortened by the presence of the airflow. The perturbation speed however is

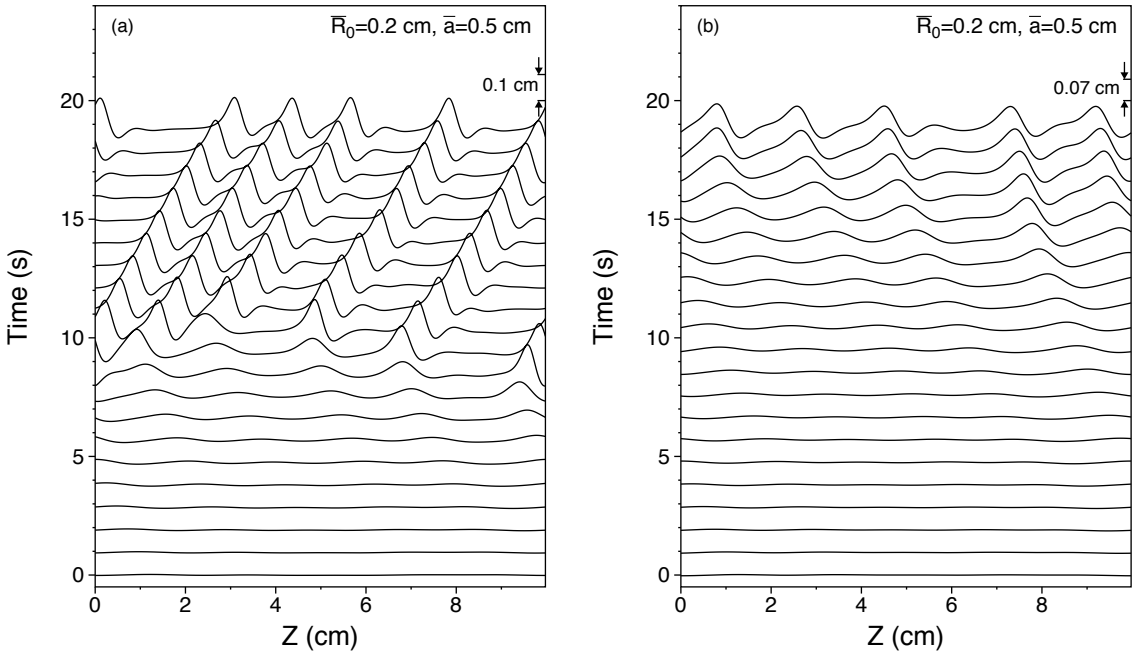

Figure 5.6.1: (a) Time snapshots showing the evolution of solutions to the long-wave model (5.4.36) in a periodic domain for $\bar{a} = 0.5$ cm, $\bar{R}_0 = 0.2$ cm, $Q^{(g)} = 330$ cm^3/s, $\mu^{(l)} = 129$ P. Interfacial profiles are shown successively shifted at equal time intervals. Profiles are shown in the lab frame of reference. (b) Time snapshots of solutions to the locally Poiseuille model (3.1.25) for same parameter values.

identical to that of the locally Poiseuille model; the additional stress terms only promote instability growth in the linear regime. Note also that as the airflow rate increases, the wavelength of maximum growth rate is shortened in a trend that qualitatively matches that of the experimental findings, as in Figure 5.1.3(b).

5.6. Model solutions

The linear analysis suggests that the long-wave model derived in Section 5.4 may better be able to capture certain features of the waves seen in the experiments, i.e. the wavelength dependence on airflow rate and the presence of large-amplitude waves. Solutions to (5.4.36) are now found by the same method as that outlined in Chapters 2 & 4. Figure 5.6.1(a) shows the evolution of the free surface as governed by the long-wave model. The instabilities begin falling down the tube as the effects of gravity are felt stronger than those of the airflow. The

airflow, however, contributes to larger instability growth, and the instabilities saturate at a higher amplitude than those seen in the locally Poiseuille model. These higher amplitude waves travel up the tube. Figure 5.6.1(b) shows the evolution of the free surface as governed by the locally Poiseuille model using the same parameters. The instabilities do not grow sufficiently large to move up the tube.

This updated long-wave model is thus also an improvement over the locally Poiseuille model in predicting the thickness of a film for a given liquid flux. Recall that the locally Poiseuille model grossly overestimates the film thickness (see Figure 5.1.1). In contrast, the presence of large-amplitude waves in the long-wave model allows thinner films to travel up the tube. Quantifying this improvement achieved by the long-wave model is an area of current study for the author; a thorough comparison between the model and experiments is underway.

CHAPTER 6

Summary

The goal of this thesis has been to model the flow of a liquid film coating the inside of a rigid vertical tube. Using long-wave, or lubrication, theory, several models were developed to study the film flow in different settings. In Chapter 2, a systematic procedure for deriving successive models for gravity-driven flow was discussed and first- and second-order models were derived and studied. The corresponding thin-film, or Frenkel, model was recovered in the appropriate limits, and comparisons were made between the two. It is shown that the long-wave model accurately captures the dynamics seen in the experiment in several ways. For both thin and moderately thick films, the combination of mean thickness and volume flux is in excellent agreement with those observed in the experiments. Temporal linear stability analysis gives a propagation speed for infinitesimal disturbances and wavelength of maximum growth rate; these speeds and wavelengths are in good agreement with experiments. Linear stability analysis from a spatial viewpoint can be used to show that there is a critical mean film thickness $\bar{h}_c$ (which depends on the tube radius and liquid properties) such that for thick films where $\bar{h}_0 > \bar{h}_c$ the film is absolutely unstable while for films where $\bar{h}_0 < \bar{h}_c$ the film is convectively unstable. (This is in contrast to a planar film flow where the film is always convectively unstable, and a coating on the exterior of a tube, for which the film can be absolutely unstable only for a very small tube radius).

Solutions of the long-wave model reveal that small perturbations to a flat interface grow in time and propagate down the tube. If the film is 'thin enough', these instabilities saturate as a series of small-amplitude traveling waves as a balance is reached between the two nonlinear surface tension terms, one of which is stabilizing and one destabilizing due to the axial and azimuthal curvature respectively. If the film is too thick, however, these instabilities blow up in finite time. This behavior is indicative of plug formation, which occurs when the film is thicker

than some critical thickness (which depends on tube radius and liquid properties). Traveling wave solutions, found by refining an appropriate portion of the model solution after a sufficiently long time had elapsed and continued using the continuation software AUTO-07P, exist for those parameter values where plug formation does not occur. Interestingly, multiple solutions of the same type (often referred to in the literature as γ_1 waves) can be found for many parameter values, one with high amplitude and speed and one with lower amplitude and speed, though, in the experiment, only the smaller, slower waves are observed. Traveling wave solutions were only found to exist in those regions of parameter space where a perturbed film did not tend to form plugs; good agreement was again found between model and experiments.

In Chapter 3, we study the case when the air core is forced to move due to an imposed pressure gradient. This core airflow creates stress at the free surface which, if the flow is strong enough, causes the liquid film to move up the tube against gravity. A locally-Poiseuille long-wave model was derived to model the flow. Temporal stability analysis shows that the free surface stress created by the airflow changes the speed of linear disturbances in the same qualitative way as seen in experiments. Several thin-film models were recovered in the appropriate limits.

In Section 5.1 this model is shown to give qualitative agreement with experiments, but does not quantitatively match the experiments, apparently due to the turbulence closure model underestimating the interfacial stress. For example, the model consistently predicts thicker films as a function of flux than what is observed in experiments, though results are qualitatively correct as experimental parameters are changed. Temporal linear analysis reveals that the speed of a linear disturbance is grossly underestimated by the model, and nonlinear results show that the amplitude of the waves that form is much smaller than that seen in experiments. One approach to improving the model is to simply use a phenomenologically modified gas viscosity; the improvements gained in the model's ability to predict the thickness of the film are unfortunately offset by losses in other regards.

The model qualitatively captures another feature of the flow. When traveling wave solutions are found as before and streamlines of the fluid flow are plotted in the moving reference frame, an interesting change in behavior is found as experimental parameters are altered. For small

amplitude traveling waves, the streamlines are fanned or constricted where the film is thicker or thinner, respectively. As the parameters S_i are altered, say S_0 decreased, the amplitude and corresponding streamline modulations grow. When S_0 reaches a critical value S_{0c}, a single stagnation point appears on the interface of the wave near the crest. As S_0 increases past S_{0c}, three stagnation points are found to emerge: two on the interface, and one in the fluid film. There is a region of closed streamlines which indicates the presence of a ring-wave that 'rolls' over the underlying film. This bifurcation separates 'mass transport' waves that have closed streamlines from 'shear waves' which do not.

Various thin-film models are derived and compared with the long-wave model. In Chapter 4 a thorough comparison is made between the long-wave model and thin-film, or Kerchman, model in the case of equal densities through study of their numerical solutions. While not directly applicable to the experiments studied here, the comparison elucidates what information can be sacrificed by using thin-film models. The Kerchman thin-film model retains, in some sense, some memory of the film's curvature by retaining the destabilizing surface tension term; this term is what separates it from its flat-film counterparts (e.g. a Benney equation where instability growth must come from inertia). However, the thin-film model does not retain a memory of the centerline of the tube. It is shown that this forgotten aspect of the original setup leads to different behavior than the long-wave model in several ways. First, for large enough surface tension in thin-film model solutions, waves grow in amplitude almost without bound through a series of mergers, only being limited by conservation of mass and the domain size; in the long-wave model, wave growth is restricted by the fact that larger waves impinge on the air core forcing the air to flow faster. Second, the possibility of waves which do not trap a recirculating core of fluid is artificially removed in the thin-film model. By retaining the full curvature, the long-wave model predicts that for thick enough films, or small enough surface tension, the waves will enhance the shear flow through fanning and constricting of streamlines, but do not trap a recirculating core of fluid.

In Chapter 5 the airflow is modeled by a second procedure in an attempt to better estimate the free surface stress caused by the airflow. A mixing-length model is used to find the leading-order axial velocity profile in pipe and channel flow. Assuming that the perturbations to the free-surface are long-wave, first-order corrections which are out of phase with the free surface are found for the stress. This stress is compared to experiments and existing models in the literature, first for wavy channel flow and then wavy pipe flow. These corrections improve on the stress predictions in the locally Poiseuille model (and to a much lesser extent a small-amplitude model from the literature), and are incorporated into the fluid film model. Through linear stability analysis it is shown that the additional stress is destabilizing, providing a mechanism for larger growth rates. Numerical solutions are again found for the model and compared to those of the locally-Poiseuille model. Finally, steps for future research are discussed.

APPENDIX A

Long-wave model including inertial terms

We here consider the case where the first-order inertial terms are significant in the model derivation given in Section 5.4; for simplicity we include only the leading-order free surface stress. We begin with the first-order equations given in (5.4.27)-(5.4.33) and find that

$$\partial_r(r\partial_r w_1) = Ar\ln\frac{r}{a} + B\left(\frac{r}{4} - \frac{r}{2}\ln ra + r(\ln(r/a))^2\right) + C\left(\frac{r^3}{2} - a^2 r\ln(r/a)\right) + Dr, \tag{A.0.1}$$

where

$$\begin{aligned} A &= ReR_t\left(\frac{8Q}{\pi mR^3} - 2R\right) \qquad (A.0.2)\\ &= Re\left(\frac{8Q}{\pi mR^3} - 2R\right)\left[-\frac{2Q^{(g)}}{\pi m}\left(\frac{a^2}{R^4} - \frac{1}{R^2}\right) + a^2 - R^2 + 2R^2\ln(R/a)\right]R_z \\ &= Re\left[-\frac{16Q^2}{\pi^2m^2}\left(\frac{a^2}{R^7} - \frac{1}{R^5}\right) + \frac{4Q}{\pi m}\left(\frac{3a^2}{R^3} - \frac{3}{R} + \frac{4}{R}\ln(R/a)\right)\right. \\ &\qquad \left. -2a^2R + 2R^3 - 4R^3\ln(R/a)\right]R_z, \\ B &= \frac{2Re}{R}\left(R^4 - \left(\frac{4Q}{\pi mR^2}\right)^2\right)R_z, \\ C &= Re\left(\frac{4Q}{\pi mR^3} - R\right)R_z, \qquad (A.0.3)\\ D &= \frac{1}{Cap}\left(\frac{R_z}{R^2} - \epsilon^2 R_{zzz}\right). \qquad (A.0.4) \end{aligned}$$

After solving one gets

$$w_1 = \frac{A}{4}\left(r^2\ln\frac{r}{a} - r^2\right) + \frac{B}{16}\left(9r^2 - 10r^2\ln\frac{r}{a} + 4r^2(\ln\frac{r}{a})^2\right) + \frac{C}{32}\left(r^4 + 8a^2r^2 - 8a^2r^2\ln\frac{r}{a}\right) + \frac{D}{4}r^2 + C_1\ln r + C_2. \tag{A.0.5}$$

where C_1 and C_2 can be determined from the boundary conditions to be:

$$C_1 = R\tau_1^{(g)} - \frac{A}{4}(2R^2 ln(R/a) - R^2) - \frac{B}{16}(8R^2 - 12R^2\ln(R/a) + 8R^2(\ln(R/a))^2)$$
$$- \frac{C}{32}(4R^4 + 8a^2R^2 - 16a^2R^2\ln(R/a)) - \frac{D}{2}R^2, \tag{A.0.6}$$
$$C_2 = \frac{A}{4}a^2 - \frac{9B}{16}a^2 - \frac{9C}{32}a^4 - \frac{D}{4}a^2 - C_1\ln a. \tag{A.0.7}$$

The second-order model then is given by

$$R_t + f_{gv}(R;a)R_z + \frac{1}{R}[Re\{f_{in}(R;a) + \tilde{\tau_0}f_{as1}(R;a) + \tilde{\tau_0}^2 f_{as2}(R;a)$$
$$+f_{curv}(R;a)\}R_z + f_{curv}(R;a)R^2R_{zzz}]_z = 0, \tag{A.0.8}$$

where

$$f_{gv}(R;a) = a^2 - R^2 + 2R^2\ln(R/a),$$
$$f_{in}(R;a) = -\frac{59}{192}R^7 + \frac{17}{64}a^2R^5 + \frac{5}{64}a^4R^3 - \frac{7}{192}a^6R + \frac{15}{16}a^2R^5\ln(R/a)$$
$$-\frac{5}{16}a^4R^3\ln(R/a) + \frac{5}{8}R^7(\ln(R/a))^2 - \frac{1}{2}a^2R^5(\ln(R/a))^2 - \frac{1}{2}R^7(\ln(R/a))^3,$$
$$f_{as1}(R;a) = -\frac{11}{24}R^3 + \frac{7}{8}a^2R - \frac{33}{64}\frac{a^4}{R} + \frac{1}{12}\frac{a^6}{R^3} + \frac{25}{16}R^3\ln(R/a) - \frac{7}{4}a^2R\ln(R/a)$$
$$+\frac{7}{16}\frac{a^4}{R}\ln(R/a) - 2R^3(\ln(R/a))^2 + a^2R(\ln(R/a))^2 + R^3(\ln(R/a))^3,$$
$$f_{as2}(R;a) = \frac{49}{64}\frac{1}{R} - \frac{73}{64}\frac{a^2}{R^3} + \frac{27}{64}\frac{a^4}{R^5} - \frac{3}{64}\frac{a^6}{R^7} - \frac{25}{16}\frac{1}{R}\ln(R/a) + \frac{13}{16}\frac{a^2}{R^3}\ln(R/a)$$
$$-\frac{1}{8}\frac{a^4}{R^5}\ln(R/a) + \frac{11}{8}\frac{1}{R}(\ln(R/a))^2 - \frac{1}{4}\frac{a^2}{R^3}(\ln(R/a))^2 - \frac{3}{4}\frac{1}{R}(\ln(R/a))^3,$$
$$f_{curv}(R;a) = \frac{1}{16C}\left(-3R^2 + 4a^2 - \frac{a^4}{R^2} + 4R^2\ln(R/a)\right).$$

Note that the leading-order free surface stress created by the airflow becomes a mechanism for instability growth through inertial effects, similar to the first-order stress corrections derived in Section 5.4. There, however, the instability mechanism did not depend on the Reynolds number and is hence relevant even for the high-viscosity flows considered here.

APPENDIX B

Alternate airflow modeling method

An alternate model for the shear stress is considered here, first for wavy channel flow, then wavy pipe flow. The model improves upon the stress predictions of the locally-Poiseuille model, but interestingly does not exhibit any dependence on Reynolds number in channel flow. As the model also depends on asymptotically inconsistent ordering and does not accurately incorporate the Reynolds stresses in turbulent flow, it is relegated to the Appendix and not studied further.

B.1. Wavy channel flow

The governing equations (5.2.1) are nondimensionalized using the following long-wave scalings

$$x = \bar{x}/\bar{S}_0, \quad z = \bar{z}/\bar{\lambda}, \quad u = \bar{u}/\bar{U}_0, \quad w = \bar{w}/\bar{W}_0,$$
$$t = \bar{t}\bar{W}_0/\bar{\lambda}, \quad p = \epsilon\bar{p}\bar{S}_0/(\bar{\mu}\bar{W}_0), \tag{B.1.1}$$

where the continuity equation again requires that $\bar{U_0} = \epsilon\bar{W}_0$ and where $\bar{S}_0$ is the mean channel half-width, t is the dimensionless time and p is the dimensionless pressure. Substituting (B.1.1) into (5.2.1) the momentum and continuity equations for the liquid become:

$$\epsilon^3 Re(u_t + uu_x + wu_z) = -p_x + \epsilon^2 u_{xx} + \epsilon^4 u_{zz}, \tag{B.1.2}$$

$$\epsilon Re(w_t + uw_x + ww_z) = -p_z + w_{xx} + \epsilon^2 w_{zz}, \tag{B.1.3}$$

$$u_x + w_z = 0, \tag{B.1.4}$$

where $Re = \rho\bar{W}_0\bar{S}_0/\mu$ is the Reynolds number. The boundary conditions are no-slip at the wall $x = S(z)$

$$u = w = 0, \tag{B.1.5}$$

and the requirement that $w_x = 0$ at the centerline of the channel, $x = 0$. To leading order we have

$$p_{0x} = 0, \quad p_{0z} = w_{0xx}, \quad \bar{u}_{0\bar{x}} + \bar{w}_{0\bar{z}} = 0, \tag{B.1.6}$$

which gives

$$w_0 = \frac{p_z}{2}(x^2 - S^2), \tag{B.1.7}$$

or in dimensional form

$$\bar{w}_0 = \frac{\bar{p}_{\bar{z}}}{2\mu}(\bar{x}^2 - \bar{S}^2), \tag{B.1.8}$$

We assume that the flux $\bar{Q}$ is prescribed and let

$$b\bar{Q} = \int_{-\bar{S}}^{\bar{S}} \bar{w}_0 d\bar{x}, \tag{B.1.9}$$

where b is the percentage of the volume flux attributed to this viscous flow. This gives

$$\bar{p}_{\bar{z}} = -\frac{3\mu b\bar{Q}}{2\bar{S}^3}, \tag{B.1.10}$$

and so

$$\bar{w}_0 = -\frac{3b\bar{Q}}{4\bar{S}^3}(\bar{x}^2 - \bar{S}^2), \quad \bar{u}_0 = -\frac{3b\bar{Q}}{4}\left(\frac{\bar{x}}{\bar{S}^2} - \frac{\bar{x}^3}{\bar{S}^4}\right), \tag{B.1.11}$$

Going to the first-order, we see that the momentum equations are

$$p_{1x} = 0, \tag{B.1.12}$$

$$Re(u_0 w_{0x} + w_0 w_{0z}) = -p_{1z} + w_{1xx}. \tag{B.1.13}$$

The first-order correction to the streamwise velocity is

$$w_1 = \frac{p_{1z}}{2}(x^2 - S^2) + \left(\frac{3b\tilde{Q}}{4}\right)^2 \left[-\frac{x^6}{30S^7} + \frac{x^4}{6S^5} - \frac{x^2}{2S^3} + \frac{11}{30S}\right] S_z. \tag{B.1.14}$$

We now apply the remaining portion of the flux to the first-order axial velocity corrections (here in dimensional form):

$$(1 - b)\bar{Q} = \int_{-\bar{S}}^{\bar{S}} \bar{w}_1 d\bar{x}, \tag{B.1.15}$$

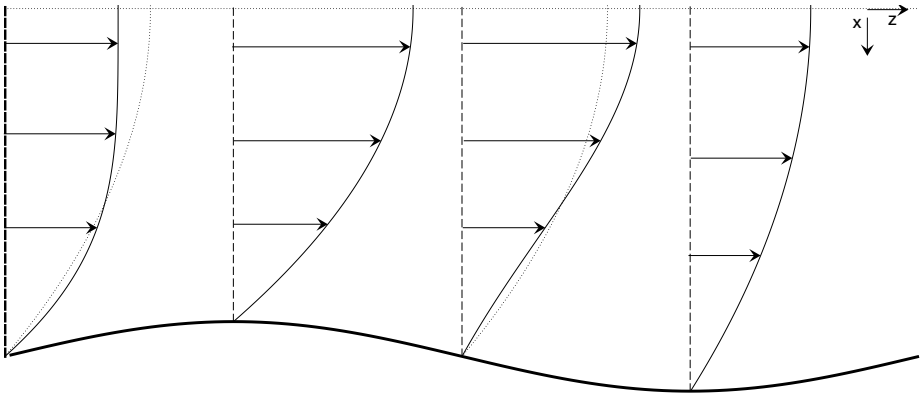

Figure B.1.1: Long-wave velocity profile $w = w_0 + w_1$ (solid lines) and locally Poiseuille velocity profile (dotted lines) in the bottom half of a sinusoidally wavy channel.

which gives

$$\bar{p}_{1\bar{z}} = \frac{3(1-b)\bar{Q}}{2\bar{S}^3} + \left(\frac{3b\bar{Q}}{2}\right)\frac{24}{35\bar{S}^3}\bar{S}_{\bar{z}}. \tag{B.1.16}$$

After substituting (B.1.16) into (B.1.15), the wall shear stress is found by evaluating the derivative of the total axial velocity at the wall $\bar{x} = \bar{S}$:

$$\mu(\bar{w}_{0\bar{x}} + \bar{w}_{1\bar{x}}) = \frac{3\mu\bar{Q}}{2\bar{S}^2} + \frac{3b^2\rho\bar{Q}^2}{35\bar{S}^2}\bar{S}_{\bar{z}}. \tag{B.1.17}$$

Figure B.1.1 shows how the long-wave velocity profile varies along a sinusoidally varying channel. At crests and troughs where $R_z = 0$ the profiles are identical. Where $R_z > 0$ the long-wave model predicts lower wall stress than the leading-order model; where $R_z < 0$ the long-wave model predicts higher wall stress. Note the same dependence on channel half-width and wall gradient in both (B.1.17) and the stress derived in Section 5.4.

We need a method to determine an approximate value for the fraction b of volume flux attributed to the viscous terms. To do this, we consider the velocity profile in a channel. Experiments have shown that a reasonable approximation for the profile across the channel is given by the logarithmic law of the wall

$$u = \frac{u_\tau}{\kappa}\ln\left(\frac{u_\tau y}{\nu}\right) + C^+, \tag{B.1.18}$$

where $\kappa \approx 0.41$ (von Karman's constant) and C^+ are constants which have been empirically determined. The value of C^+ is the source of some debate in the literature, and may depend on the Reynold's number of the flow, but is usually in the range $5 - 5.5$. We describe below how we select the value of C^+.

In laminar channel flow where a pressure gradient drives the flow, the pressure gradient is balanced entirely be viscous forces and the velocity profile is given by

$$w_{visc}(r) = \frac{3\tilde{Q}}{4S_0^3}(2S_0 x - x^2). \tag{B.1.19}$$

For steady, parallel inviscid flow, the velocity profile is given everywhere by the average velocity

$$w_{inv}(r) = \frac{\tilde{Q}}{2S_0}. \tag{B.1.20}$$

The actual velocity in turbulent channel flow, approximated by the log law of the wall, lies somewhere in between these two extremes: in the core region, the velocity is closest to the inviscid profile, while near the wall the velocity profile is closer to the viscous profile. The empirical velocity profile can be expressed as a weighted average of the viscous and inviscid solutions as follows:

$$w(r) = f(r)w_{visc}(r) + [1 - f(r)]w_{inv}. \tag{B.1.21}$$

All three velocity profiles are shown in Figure B.1.2(a), while the function f is shown in Figure B.1.2(b).

In order for $f(r)$ to remain positive and bounded between 0 and 1, all three velocity profiles must agree at some value of y. This value can be determined by setting the viscous (B.1.19) and inviscid (B.1.20) velocity profiles equal and solving for y:

$$y_c = \left(1 - \frac{1}{\sqrt{3}}\right). \tag{B.1.22}$$

In order for b to remain positive and bounded between 0 and 1, we insist

$$w(y_c) = w_{visc}(y_c) = w_{inv}(y_c). \tag{B.1.23}$$

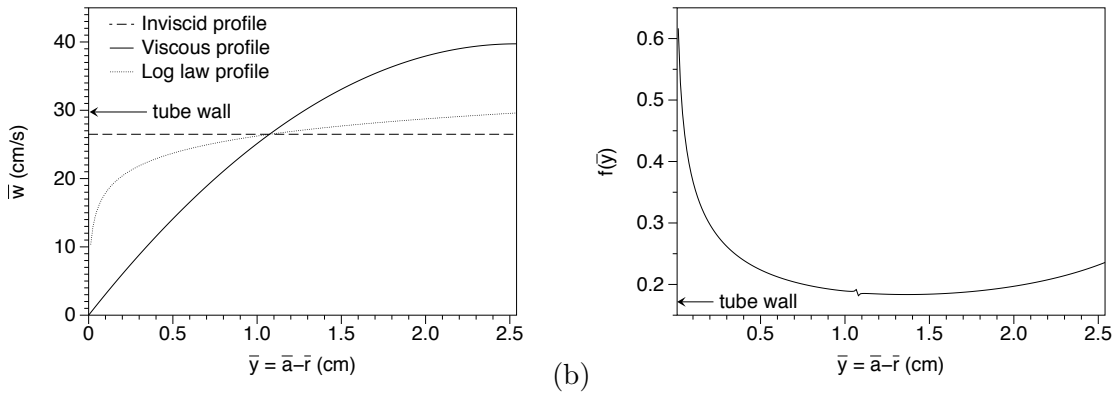

(a) (b)

Figure B.1.2: (a) Mean velocity profiles for viscous, inviscid, and turbulent channel flow. (b) The proportion of flux due to 'leading-order' balance of viscosity and pressure gradient.

This is achieved by adjusting the constant C^+ as necessary in (B.1.18). For all profiles considered here C^+ was found to lie between 4.9 and 5.4, roughly consistent with values found in the literature.

With b now determined we compare $\bar{\tau}^{(g)}$ with experiments performed by Zilker, Cook & Hanratty [85]. In these experiments, a liquid flowed over a linearly wavy pipe. The Reynolds numbers ranged from 7850 to 31,000. The wall stress over one wavelength is shown in Figure B.1.3 for Reynolds numbers of (a) 7850 and (b) 31,000. Predictions from both the long-wave model and the small-amplitude model (as developed in [79]) are shown. For the $Re = 7850$ we can see that both models miss the phase shift slightly - the long-wave model overstates the shift while the small-amplitude model understates the shift - while the long-wave model better predicts the amplitude of the phase shift. For $Re = 31,000$ the long-wave model appears to better capture the phase shift while overstating the amplitude of the shear stress variations. It is not surprising that the small-amplitude model has the most difficulty quantitatively matching the highest Reynolds number experiments (see Figures 7-9 in [79]) since the lengthscale is smallest, thus making the wall modulations largest in the chosen nondimensional scalings.

B.2. Wavy pipe flow

As before, we seek an approximate expression for $\bar{\tau}^{(g)}$ to use in modeling the liquid film flow. In modeling the gas flow, it will be assumed that the gas flows faster than the liquid by

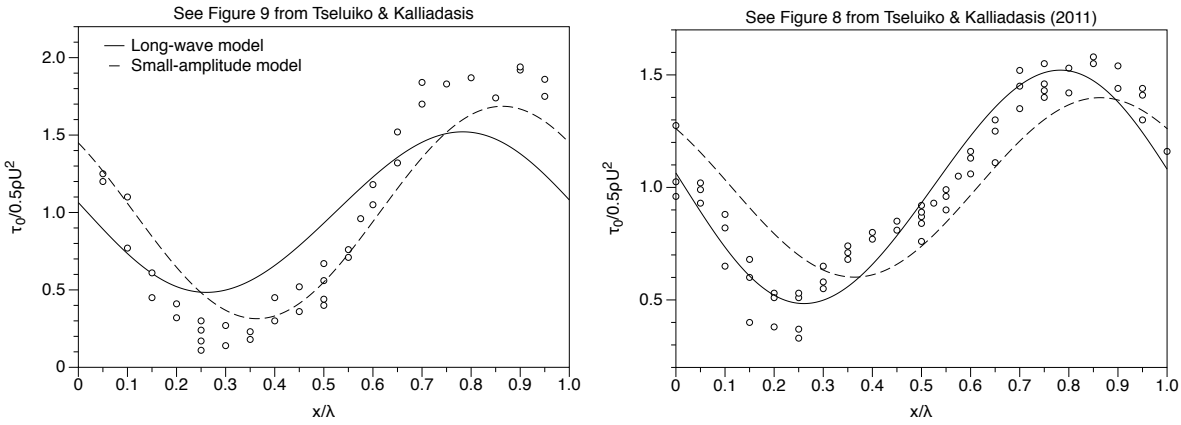

Figure B.1.3: Wall shear stress in a wavy channel according to long-wave model (solid line), small-amplitude model in [79] (dashed line) and experiments by Zilker *et al.* [85]. (a) $Re = 7850$, (b) $Re = 31,000$. (Compare (a) and (b) to Figures 9 and 8 in [79] respectively.

at least two orders of magnitude, so that the gas essentially views the air-liquid free surface as motionless, or as a rigid wall. The nondimensional governing equations are then the axisymmetric Navier-Stokes equations in cylindrical coordinates (1.3.1). To non-dimensionalize, we use the following scalings:

$$r = \bar{r}/\bar{R}_0, \quad z = \bar{z}/\bar{\lambda}, \quad u = \bar{u}/\bar{U}_0, \quad w = \bar{w}/\bar{W}_0,$$

$$t = \bar{t}\bar{W}_0/\bar{\lambda}, \quad p = \epsilon\bar{p}\bar{R}_0/(\bar{\mu}^{(g)}\bar{W}_0), \quad \tau = \bar{\tau}\bar{R}_0/(\bar{\mu}^{(g)}\bar{W}_0), \tag{B.2.1}$$

where t is the dimensionless time, τ is the dimensionless tangential stress, p is the dimensionless pressure, $\bar{W}_0 = 2\bar{Q}/\pi\bar{R}_0^2$ is the centerline laminar gas velocity, and $\bar{U}_0 = \epsilon\bar{W}_0$ from the continuity equation. As before, if $\epsilon = \bar{R}_0/\bar{\lambda} \ll 1$ the distortions to the air-liquid interface are considered long-wave.

This leads to the nondimensional governing equations

$$\epsilon^3 Re^{(g)}(u_t^{(g)} + u^{(g)}u_r^{(g)} + w^{(g)}u_z^{(g)}) = -p_r^{(g)} + \epsilon^2\left(\frac{1}{r}\partial_r(ru_r^{(g)}) + \epsilon^2 u_{zz}^{(g)} - \frac{u^{(g)}}{r^2}\right), \tag{B.2.2}$$

$$\epsilon Re^{(g)}(w_t^{(g)} + u^{(g)}w_r^{(g)} + w^{(g)}w_z^{(g)}) = -p_z^{(g)} + \frac{1}{r}\partial_r(rw_r^{(g)}) + \epsilon^2 w_{zz}^{(g)}, \tag{B.2.3}$$

$$\frac{1}{r}\partial_r(ru^{(g)}) + w_z^{(g)} = 0. \tag{B.2.4}$$

The boundary condition at the wall $r = R$ is no-slip,

$$w^{(g)} = 0, u^{(g)} = 0, \tag{B.2.5}$$

while at the center of the tube $r = 0$ we require that the velocity field be finite.

We now expand each of the gas variables in a regular perturbation expansion as beforeand substitute the expansions into (B.2.2)-(B.2.5). We then take $\epsilon \to 0$ and find at leading order

$$0 = p_{0r}^{(g)}, \quad \frac{1}{r}\partial_r(rw_{0r}^{(g)}) = p_{0z}^{(g)}, \quad \frac{1}{r}\partial_r(ru_0^{(g)}) + w_{0z}^{(g)} = 0. \tag{B.2.6}$$

with boundary conditions at the wall ($r = R$)

$$u_0^{(g)} = w_0^{(g)} = 0. \tag{B.2.7}$$

This gives an axial velocity of

$$w_0^{(g)} = \frac{p_{0z}^{(g)}}{4}(r^2 - R^2), \tag{B.2.8}$$

which is exactly the Poiseuille velocity profile for a steady laminar pipe flow if R is constant, i.e. an unperturbed interface. We now find the pressure gradient by assuming that some fraction b ($0 < b < 1$), still to be determined, of the volume flux of air $Q^{(g)} = \pi/2$ is accounted for by these leading-order terms.

$$\begin{aligned} bQ^{(g)} &= \int_0^R 2\pi r w_0^{(g)} dr \\ &= \frac{\pi p_{0z}}{8} R^4, \end{aligned}$$

which gives

$$p_{0z}^{(g)} = \frac{4b}{R^4}, \tag{B.2.9}$$

and

$$w_0^{(g)} = \frac{b}{R^4}(r^2 - R^2). \tag{B.2.10}$$

We now determine the corrections at $O(\epsilon)$, assuming that b is independent of z, i.e. at every point in the wavy tube the ratio of flux caused by viscous forces to that caused by inertial

forces is the same. The equations of motion at $O(\epsilon)$ are

$$0 = p_{1r}^{(g)}, \tag{B.2.11}$$

$$\frac{1}{r}\partial_r(rw_{1r}^{(g)}) = p_{1z}^{(g)} + Re^{(g)}(u_0^{(g)}w_{0r}^{(g)} + w_0^{(g)}w_{0z}^{(g)}), \tag{B.2.12}$$

$$\frac{1}{r}\partial_r(ru_1^{(g)}) + w_{1z}^{(g)} = 0. \tag{B.2.13}$$

As before, no-slip at the wall ($r = R$) is enforced:

$$u_1^{(g)} = w_1^{(g)} = 0. \tag{B.2.14}$$

This gives a first-order axial velocity correction of

$$w_1^{(g)} = \frac{p_{1z}^{(g)}}{4}(r^2 - R^2) - \frac{2b^2Rey}{R^9}\left(\frac{r^2R^4}{4} - \frac{r^4R^2}{8} + \frac{r^6}{36} - \frac{11R^6}{72}\right)R_z. \tag{B.2.15}$$

We then find the value of p_{1z} as before, by using the remaining portion of the air volume flux:

$$(1-b)Q^{(g)} = \int_0^R 2\pi r w_1 dr, \tag{B.2.16}$$

which gives

$$p_{1z}^{(g)} = \frac{4(1-b)}{R^4} + \frac{b^2ReyR_z}{R^5}. \tag{B.2.17}$$

Substitution of (B.2.17) into (B.2.15) allows the wall stress to be calculated as before:

$$\tau^{(g)} = \frac{2}{R^3} + \epsilon\frac{ReyR_z}{6R^4} + O(\epsilon^2), \tag{B.2.18}$$

or in dimensional terms

$$\bar{\tau}^{(g)} = -\frac{4\bar{\mu}^{(g)}\bar{Q}^{(g)}}{\pi\bar{R}^3} + \frac{2b^2\bar{\rho}^{(g)}(\bar{Q}^{(g)})^2}{3\pi^2\bar{R}^4}\bar{R}_{\bar{z}}. \tag{B.2.19}$$

Figure B.2.1 shows the variations in the locally Poiseuille and long-wave model velocity profiles along a tube with sinusoidal walls. The models agree at crests and troughs where $R_z = 0$. Where $R_z > 0$ the long-wave model predicts less wall stress than the locally Poiseuille model; where $R_z < 0$ the long-wave model predicts greater wall stress. The long-wave model thus predicts a wall stress out of phase with the wall itself, a property also observed in experiments.

As before, we approximate b by using the log law of the wall velocity profile. Turbulent pipe flow is well-studied, and several empirical formulas for the mean velocity profile have been

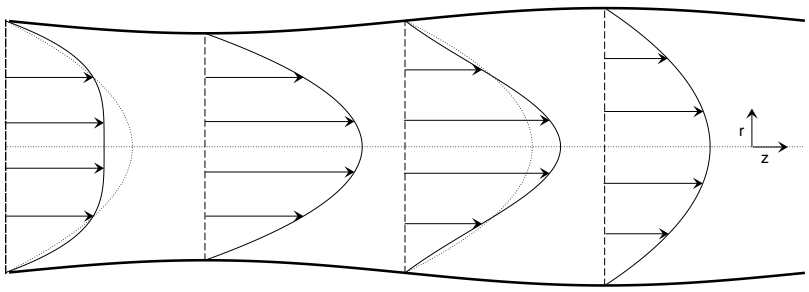

Figure B.2.1: Long-wave velocity profile $w = w_0 + w_1$ (solid lines) and locally Poiseuille velocity profile (dotted lines) along a sinusoidally wavy tube.

developed (see, e.g. [46; 17; 53; 50; 13; 9; 83; 65]. Most of these formulas are due in some part to an approach matching separate self-similar expressions for the velocity near the wall and for that in the core region. Near the wall, viscous effects are expected to dominate; the higher the Reynolds number, the thinner this laminar wall-layer is, a fact reflected in the traditional 'inner-coordinate' scaling using the shear velocity. The standard 'law of the wall' states that in a very small region in the immediate viscinity of the wall, the velocity profile is linear. Just outside this thin layer, there is a region where the mean velocity transitions to a logarithmic profile. This logarithmic law is not universally accepted, but gives generally good agreement with many experiments, even in the core region past its asymptotic validity (with the exception of a wake region where the log-law slightly undestimates the velocity). The logarithmic law is typically stated in the 'inner-coordinate' scaling as:

$$u = \frac{u_\tau}{\kappa} \ln\left(\frac{u_\tau y}{\nu}\right) + C^+, \tag{B.2.20}$$

where $\kappa \approx 0.41$ (von Karman's constant) and C^+ are constants which have been empirically determined. The value of C^+ is a source of some debate in the literature, and is seen to increase slightly with decreasing Reynolds number. We will revisit this value shortly.

In laminar pipe flow where a pressure gradient drives the flow, the pressure gradient is balanced by viscous forces, and the velocity profile is given by

$$w_{visc}(r) = \frac{2Q^{(g)}}{\pi R^4}(r^2 - R^2). \tag{B.2.21}$$

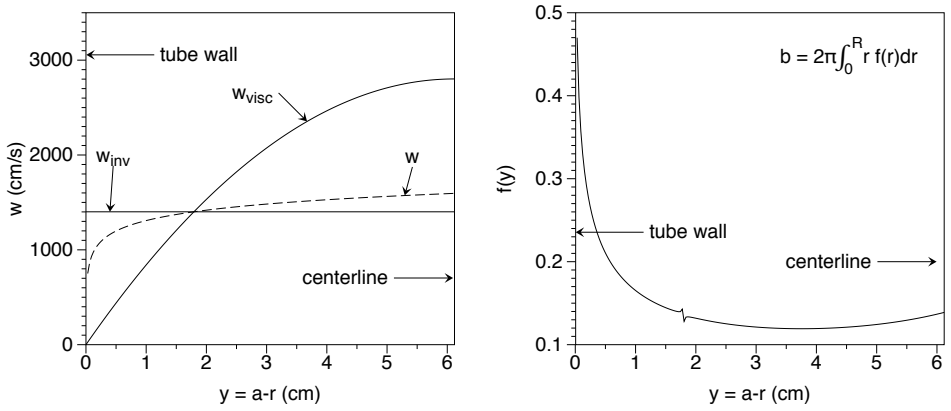

Figure B.2.2: (a) Mean velocity profiles for viscous, inviscid, and turbulent pipe flow. (b) The proportion of flux due to 'leading-order' balance of viscosity and pressure gradient.

In steady, parallel inviscid flow, the velocity profile is everywhere given by the average velocity,

$$w_{inv} = \frac{Q}{\pi R^2}. \tag{B.2.22}$$

The actual velocity profile in turbulent pipe flow, approximated by the log law of the wall, lies somewhere in between these two extremes: in the core region, the velocity is closest to the inviscid solution, while near the wall, the velocity profile is closer to the viscous solution. We can express the empirical velocity profile as a weighted average of the viscous and inviscid solutions as follows:

$$w = f(r)w_{visc}(r) + [1 - f(r)]w_{inv}. \tag{B.2.23}$$

All three velocity profiles are shown in Figure B.2.2(a), while the function f is showing in Figure B.2.2(b).

As before, there must be one point $r = r_c$ where

$$w(r_c) = w_{visc}(r_c) + w_{inv}(r_c); \tag{B.2.24}$$

this point is found to be $r_c = \frac{1}{\sqrt{2}}R$. The value of C^+ is adjusted to guarantee that this condition is met.

The long-wave model is compared with the locally Poiseuille model developed in Chapter 3 and with experiments performed by Hsu & Kennedy [27]. The experiments were conducted at

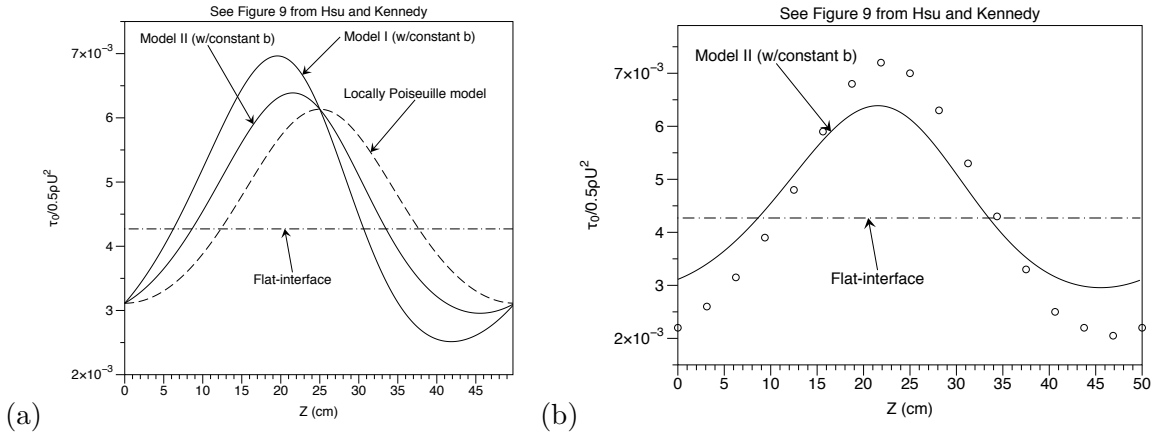

Figure B.2.3: (a) Comparison of shear stress predicted by flat-interface (dash-dot line), locally-Poiseuille model (dashed line) and the long-wave model (solid). (b) Comparison of the stress data in [27] with the present approach (Model II in [27]).

two different Reynolds numbers with two different wall wavelengths. As was shown in [27], the locally Poiseuille model predicts no phase shift in the stress and underestimates the amplitude of the stress modulations. The long-wave model also underestimates the magnitude of the stress modulations, but seems to capture the phase shift fairly well.

APPENDIX C

Modeling a shear-thinning film flow

Thus far it has been assumed that the liquid film is Newtonian. Mucus, however, is known to be non-Newtonian. We thus seek to adapt the long-wave modeling approach to the study of a non-Newtonian liquid film.

Mucus is known to be a shear-thinning liquid, and this section describes an adaptation of the gravity-driven model from Chapter 2 to include shear-thinning effects. It is of particular interest whether the mass transport behavior seen in some traveling wave solutions to (2.2.12) is present in shear-thinning liquid films. Palacios-Morales & Zenit [63] studied the behavior of vortex rings in a power-law shear-thinning fluid, showing that the circulation decreased with increasing shear-thinning behavior. Other studies of interest include thin-film non-Newtonian models by Zhang *et al.* [84] and by Moore & Shelley [55]; further modeling along similar lines to these studies is left for future work.

The fluid flow is described by the incompressible, axisymmetric Navier-Stokes equations in cylindrical coordinates:

$$\rho(\vec{u}_t + \vec{u}\cdot\nabla\vec{u}) = -\nabla p + \nabla\cdot\mathbf{T} + \vec{g}, \tag{C.0.1}$$

where the velocity components $\vec{u} = (\bar{u}, \bar{v}, \bar{w})$ correspond to the coordinates $(\bar{r}, \bar{\theta}, \bar{z})$. Here $\bar{z}$ increases as one moves down the tube. The stress tensor is denoted by $\mathbf{T}$.

As before, we denote a typical wavelength in the axial direction by $\bar{\lambda}$, and the mean thickness of the film by $\bar{h_0} = \bar{a} - \bar{R}_0$. We then take the ratio of the two lengthscales to be small, i.e. $\epsilon = \bar{h_0}/\bar{\lambda} \ll 1$. We nondimensionalize (C.0.1) with $r = \bar{r}/\bar{h}_0$, $z = \bar{z}/\bar{\lambda}$, $u = \bar{u}/\bar{U}_0$, $w = \bar{w}/\bar{W}_0$, $t = \bar{t}\bar{W}_0/\bar{\lambda}$, $p = \bar{p}\bar{h}_0/(\mu\bar{W}_0)$, where $\bar{W}_0 = g\bar{h}_0^2\rho/\mu$ is the axial velocity scale and $\bar{U}_0 = \epsilon\bar{W}_0$:

$$\epsilon^2 Re(u_t + uu_r + wu_z) = -p_r + \epsilon\left(\frac{1}{r}\partial_r(r\mu u_r) + \epsilon^2\partial_z(\mu u_z) - \frac{\mu u}{r^2}\right), \tag{C.0.2}$$

$$\epsilon Re(w_t + uw_r + ww_z) = -\epsilon p_z + \frac{1}{r}\partial_r(r\mu w_r) + \epsilon^2\partial_z(\mu w_z) + 1, \tag{C.0.3}$$

$$\frac{1}{r}\partial_r(ru) + w_z = 0. \tag{C.0.4}$$

$Re = W_0\rho h_0/\mu_{ch}$ is the Reynolds number (where μ_{ch} is some chosen characteristic viscosity). Note that μ is no longer constant, as in the Newtonian case studied in Chapter 2.

The viscosity of a shear-thinning fluid depends on the rate-of-strain tensor

$$\dot{\gamma} = \begin{pmatrix} \epsilon u_r & 0 & \frac{1}{2}(w_r + \epsilon^2 u_z) \\ 0 & \frac{\epsilon u}{r} & 0 \\ \frac{1}{2}(w_r + \epsilon^2 u_z) & 0 & \epsilon w_z \end{pmatrix} \tag{C.0.5}$$

The second invariant of the rate-of-strain tensor is used as the scalar shear-rate and is given by

$$\begin{aligned} \dot{\gamma} &= \sqrt{\frac{1}{2}\dot{\gamma} : \dot{\gamma}} \\ &= \sqrt{\frac{1}{2}w_r^2 + O(\epsilon^2)}. \end{aligned} \tag{C.0.6}$$

We express the velocities, pressure, and viscosity as a regular perturbation expansion around the long-wave parameter ϵ:

$$\begin{aligned} u &= u_0 + \epsilon u_1 + ..., \\ w &= w_0 + \epsilon w_1 + ..., \\ p &= p_0 + \epsilon p_1 + ..., \end{aligned} \tag{C.0.7}$$

$$\mu(\nabla\vec{u}) = \mu_0(\nabla\vec{u}) + \mu_1(\nabla\vec{u})\epsilon + O(\epsilon^2), \tag{C.0.8}$$

The deviatoric stress tensor is given by

$$2\mu\dot{\gamma} = \begin{pmatrix} 2u_{0r}\mu_o\epsilon & 0 & w_{0r}\mu_0 + (w_{1r}\mu_0 + w_{0r}\mu_1)\epsilon \\ 0 & \frac{2u_0\mu_0}{r}\epsilon & 0 \\ w_{0r}\mu_0 + (w_{1r}\mu_0 + w_{0r}\mu_1)\epsilon & 0 & 2w_{0z}\mu_0\epsilon \end{pmatrix} + O(\epsilon^2),$$

and the divergence of the deviatoric stress tensor is

$$\nabla\cdot(2\mu\dot{\gamma}) = \begin{pmatrix} \left[\frac{2}{r}\partial_r(ru_{0r}\mu_0) + \partial_z(w_{0r}\mu_0)\right]\epsilon \\ 0 \\ \frac{1}{r}\partial_r(rw_{0r}\mu_0) + \frac{1}{r}\partial_r[r(w_{1r}\mu_0 + w_{0r}\mu_1)]\epsilon \end{pmatrix} + O(\epsilon^2). \tag{C.0.9}$$

Substituting (C.0.9) and (C.0.7) into the Navier-Stokes equations leads to the following expressions for the radial and axial momentum equations up to $O(\epsilon)$, respectively:

$$p_{0r} + \epsilon p_{1r} = \epsilon\left(\frac{2}{r}\partial_r(ru_{0r}\mu_0) + \partial_z(w_{0r}\mu_0)\right) + O(\epsilon^2), \tag{C.0.10}$$

$$\epsilon Re(w_{0t} + u_0 w_{0r} + w_0 w_{0z}) + \epsilon p_{0z} = \frac{1}{r}\partial_r(rw_{0r}\mu_0) + \frac{\epsilon}{r}\partial_r[r(w_{1r}\mu_0 + w_{0r}\mu_1)] + 1 + O(\epsilon^2),$$

$$\frac{1}{r}\partial_r[r(u_0 + \epsilon u_1)] + w_{0z} + \epsilon w_{1z} = O(\epsilon^2).$$

We then take $\epsilon \to 0$ and find at leading order

$$0 = p_{0r}, \quad \frac{1}{r}\partial_r(rw_{0r}\mu_0) = -1, \quad \frac{1}{r}\partial_r(ru_0) + w_{0z} = 0, \tag{C.0.11}$$

with boundary conditions at the wall

$$u_0 = w_0 = 0, \tag{C.0.12}$$

and at the free surface

$$\mu_0 w_{0r} = 0, \quad p_0 = -\frac{1}{C}\left(\frac{1}{R} - \epsilon^2 R_{zz}\right). \tag{C.0.13}$$

The leading-order model for the evolution of the interface is

$$R_t = \frac{1}{R}\frac{\partial}{\partial z}\int_R^a w_0 r dr. \tag{C.0.14}$$

The leading-order radial velocity u_0 can be calculated from the continuity equation.

The first-order correction to the axial momentum equation (after integrating once and ignoring inertial effects) is

$$p_{0z}\left(\frac{r}{2} - \frac{R^2}{2r}\right) = w_{1r}\mu_0 + w_{0r}\mu_1, \tag{C.0.15}$$

Boundary conditions at the wall $r = a$ are

$$u_1 = w_1 = 0, \tag{C.0.16}$$

and at the interface $r = R(z,t)$

$$w_{1r} = 0, \quad p_1 = 2u_{0r}, \tag{C.0.17}$$

where the first condition in (C.0.17) has already been used in determining (C.0.15).

The first-order model for the interface is then given by

$$R_t = \frac{1}{R}\frac{\partial}{\partial z}\int_R^a r(w_0 + \epsilon w_1)dr. \tag{C.0.18}$$

A model is now needed for the viscosity's dependence on shear rate. We adopt a Newtonian/ power-law hybrid model, where we suppose that for shear-rates below some critical shear-rate, $w_r < w_r^*$, the viscosity is constant i.e. $\mu = \mu_0$, while for higher shear-rates $w_r > w_r^*$ the viscosity follows the power law model, i.e. $\mu = m w_r^{n-1}/2^{\frac{n-1}{2}}$. The dependence is determined by the value of n: for $n < 1$ the fluid is shear-thinning (the case of interest here) and for $n > 1$ the fluid is shear-thickening. Here m is the consistency and is simply the Newtonian viscosity in the case $n = 1$. See Figure C.0.1.

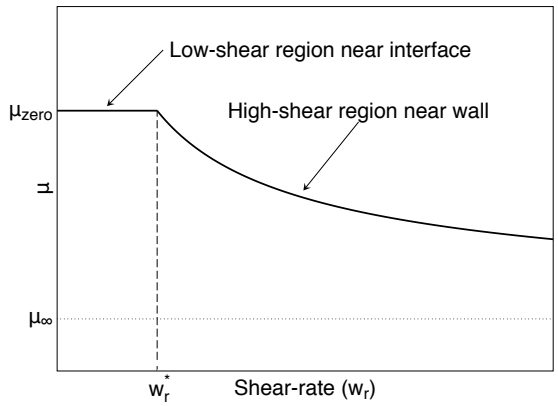

Figure C.0.1: Dependence of viscosity on shear-rate.

For fluid near the interface, the shear-rates are expected to be small due to the boundary condition $w_r(R) = 0$; in this region we use the Newtonian expression for the velocity gradient

(in dimensional form):

$$\begin{aligned}\tilde{w}_r &= \tilde{w}_{0r} + \tilde{w}_{1r} \\ &= \frac{\rho g}{\mu_{zero}}\left(\frac{r}{2} - \frac{R^2}{2r}\right) - \frac{\gamma}{\mu_z}\left(\frac{r}{2} - \frac{R^2}{2r}\right)\left(\frac{R_z}{R^2} + R_{zzz}\right) \\ &= \frac{1}{\mu_z}\left(\frac{r}{2} - \frac{R^2}{2r}\right)\left[\rho g - \gamma\left(\frac{R_z}{R^2} + R_{zzz}\right)\right], \end{aligned} \tag{C.0.19}$$

where the zero-stress boundary condition at the free surface has been enforced. We assume that this description of the velocity gradient is valid from the interface into the fluid until the radial location $r = r^*$ when the velocity gradient reaches the critical shear-thinning value $w_r^* = \tilde{w}_r(r^*)$; this is true for

$$r^*(z) = \frac{\mu_z w_r^*}{\rho g - \gamma(R_z/R^2 + R_{zzz})} + \sqrt{\frac{\mu_z^2 (w_r^*)^2}{\rho g - \gamma(R_z/R^2 + R_{zzz})} + R^2}. \tag{C.0.20}$$

If $r^* > a$, we set $r^* = a$ and have a strictly Newtonian flow.

If however, $r^* < a$, then in the rest of the fluid layer, i.e. the portion of the layer closer to the wall $r^* < r < a$, we assume that the leading-order velocity gradient is described by the power law model

$$\frac{m w_{0r}^n}{2^{\frac{n-1}{2}}} = \left(\frac{r}{2} - \frac{A_0(z)}{r}\right)\rho g, \tag{C.0.21}$$

which gives

$$w_{0r} = \left(\frac{2^{\frac{n-1}{2}}\rho g}{m}\right)^{\frac{1}{n}}\left(\frac{r}{2} - \frac{A_0(z)}{r}\right)^{\frac{1}{n}}. \tag{C.0.22}$$

The constant of integration $A_0(z)$ is found by insisting that $w_{0r}(r^*) = b w_{0r}^*$ where $b(z,t)$ represents the portion of stress accounted for by the leading-order flow:

$$\begin{aligned} A_0(z) &= \frac{(r^*)^2}{2} - \frac{m(b(z,t)w_{0r}^*)^n r^*}{2^{\frac{n-1}{2}}\rho g}, \\ b(z,t) &= \frac{\rho g}{\rho g - \gamma(R_z/R^2 + R_{zzz})}. \end{aligned} \tag{C.0.23}$$

As long as $\rho g - \gamma(R_z/R^2 + R_{zzz}) \neq 0$, b is well-defined. A brief argument that b will always be well-defined is outlined here: as the contributions from the first-order corrections become

significant in a way that sends $\rho g - \gamma(R_z/R^2 + R_{zzz}) \to 0$ at some location z_0, $r^* \to \infty$ and so the fluid is described by the Newtonian flow throughout the layer before b is no longer well-defined.

We now have a continuous velocity gradient across the fluid layer. Integrating will give us a velocity profile that is continuous and once differentiable. Since our velocity boundary condition occurs at the wall (no-slip), we begin by integrating in the high-shear region (here we're assuming that $r^* < a$, i.e. the fluid is treated as non-Newtonian in some portion of the flow). w_0 can be found in terms of the hypergeometric function ${}_2F_1$ by integrating:

$$w_0 = \frac{nr}{n-1}\left(\frac{2^{\frac{n-1}{2}}\rho g}{m}\right)^{\frac{1}{n}}\left(\frac{r}{2} - \frac{A_0}{r}\right)^{\frac{1}{n}}\left(1 - \frac{r^2}{2A_0}\right)^{-\frac{1}{n}} \times {}_2F_1\left(-\frac{1}{n}, \frac{n-1}{2n}, \frac{3n-1}{2n}, \frac{r^2}{2A_0}\right) + B_0(z). \tag{C.0.24}$$

$B_0(z)$ is found by enforcing the no-slip boundary condition at the wall, i.e.

$$B_0(z) = -\frac{na}{n-1}\left(\frac{2^{\frac{n-1}{2}}\rho g}{m}\right)^{\frac{1}{n}}\left(\frac{a}{2} - \frac{A_0}{a}\right)^{\frac{1}{n}}\left(1 - \frac{a^2}{2A_0}\right)^{-\frac{1}{n}} {}_2F_1\left(-\frac{1}{n}, \frac{n-1}{2n}, \frac{3n-1}{2n}, \frac{a^2}{2A_0}\right).$$

Using the fact that the velocity profile must be continuous at $r = r^*$, we can find the low-shear velocity as

$$\tilde{w_0} = \frac{\rho g}{\mu_{zero}}\left(\frac{r^2}{4} - \frac{R^2}{2}\ln r\right) + C_0(z), \tag{C.0.25}$$

where

$$C_0(z) = w_0(r^*) - \frac{\rho g}{\mu_{zero}}\left(\frac{(r^*)^2}{4} - \frac{R^2}{2}\ln r^*\right), \tag{C.0.26}$$

is found using the value of $w_0(r^*)$ already found. This gives a continuous and once-differentiable velocity profile which approximates the true velocity profile.

As before, the leading-order model equation is given by

$$R_t = \frac{1}{R}\frac{\partial}{\partial z}\int_R^a r w_0(r) dr. \tag{C.0.27}$$

The first-order corrections can be found in a similar fashion. For the Newtonian region, we have already found that

$$\tilde{w}_{1r} = -\frac{\gamma}{\mu_{zero}}\left(\frac{r}{2} - \frac{R^2}{2r}\right)\left(\frac{R_z}{R^2} + R_{zzz}\right). \tag{C.0.28}$$

As before, we find w_{1r}:

$$w_{1r} = \frac{\gamma}{n\rho g}\left(\frac{R_z}{R^2} + R_{zzz}\right)\left(\frac{2^{\frac{n-1}{2}}\rho g}{m}\right)^{\frac{1}{n}}\left(\frac{r}{2} - \frac{A_1(z)}{r}\right)^{\frac{1}{n}}. \tag{C.0.29}$$

$A_1(z)$ is found by enforcing the boundary conditions $w_{1r}(r^*) = (1-b)w_r^*$ in the standard way, i.e.

$$A_1(z) = \frac{(r^*)^2}{2} - \frac{mr^*}{2^{\frac{n-1}{2}}\rho g}\left(\frac{n\rho g(1-b)w_r^*}{\gamma(R_z/R^2 + R_{zzz})}\right)^n. \tag{C.0.30}$$

As before, we now integrate the velocity gradient in the near-wall high-shear region:

$$w_1 = \frac{\gamma r}{(n-1)\rho g}\left(\frac{R_z}{R^2} + R_{zzz}\right)\left(\frac{2^{\frac{n-1}{2}}\rho g}{m}\right)^{\frac{1}{n}}\left(\frac{r}{2} - \frac{A_1}{r}\right)^{\frac{1}{n}}\left(1 - \frac{r^2}{2A_1}\right)^{-\frac{1}{n}} \times$$
$${}_2F_1\left(-\frac{1}{n}, \frac{n-1}{2n}, \frac{3n-1}{2n}, \frac{r^2}{2A_1}\right) + B_1(z).$$

$B_1(z)$ is found by enforcing the no-slip boundary condition:

$$B_1(z) = -\frac{\gamma a}{(n-1)\rho g}\left(\frac{R_z}{R^2} + R_{zzz}\right)\left(\frac{2^{\frac{n-1}{2}}\rho g}{m}\right)^{\frac{1}{n}}\left(\frac{a}{2} - \frac{A_1}{a}\right)^{\frac{1}{n}}\left(1 - \frac{a^2}{2A_1}\right)^{-\frac{1}{n}} \times$$
$${}_2F_1\left(-\frac{1}{n}, \frac{n-1}{2n}, \frac{3n-1}{2n}, \frac{a^2}{2A_1}\right).$$

Using the fact that the velocity profile must be continuous at $r = r^*$, we can find the low-shear velocity as

$$\tilde{w}_1 = -\frac{\gamma}{\mu_{zero}}\left(\frac{R_z}{R^2} + R_{zzz}\right)\left(\frac{r^2}{4} - \frac{R^2}{2}\ln r\right) + C_1(z), \tag{C.0.31}$$

where

$$C_1(z) = w_1(r^*) + \frac{\gamma}{\mu_{zero}}\left(\frac{R_z}{R^2} + R_{zzz}\right)\left(\frac{(r^*)^2}{4} - \frac{R^2}{2}\ln r^*\right), \tag{C.0.32}$$

is found using the value of $w_1(r^*)$ already found.

This gives a continuous velocity profile across the entire fluid layer that is consistent with the long-wave assumption to first-order. As before, the equation which models the evolution of

the free surface is

$$R_t = \frac{1}{R}\frac{\partial}{\partial z}\int_R^a r[w_0(r) + \epsilon w_1(r)]dr$$
$$= \frac{1}{R}\frac{\partial}{\partial z}\left[\int_R^{r^*} r[\tilde{w}_0(r) + \epsilon\tilde{w}_1(r)]dr + \int_{r^*}^a r[w_0(r) + \epsilon w_1(r)]dr\right].$$

Integrating the velocity profile in the Newtonian low-shear region is straightforward; integrating the velocity profile analytically in the power-law high-shear region is not as straightforward. In order to find an approximate model equation, we will approximate the velocity profile with a polynomial in the non-Newtonian high-shear region as follows:

Evaluating $w(a)$ and $w(r^*)$, with $w = w_0 + w_1$, gives the value of the velocity profile at the two boundaries of the high-shear region. We also need $w_r(r^*)$ to match the value determined from the low-shear region, and so choose to approximate w with a quadratic $w_{est} = c_2r^2+c_1r+c_0$ subject to the three conditions:

$$a^2c_2 + ac_1 + c_0 = 0,$$

$$(r^*)^2c_2 + r^*c_1 + c_0 = w(r^*),$$

$$2r^*c_2 + c_1 = w_r^*.$$

This system is solved and found to be

$$c_0(z) = -aw_r^* + \frac{2a(a-r^*)w_r^* + 2aw(r^*)}{a-r^*},$$
$$c_1(z) = w_r^* + \frac{2r^*(a-r^*)w_r^* + 2r^*w(r^*)}{(a-r^*)^2},$$
$$c_2(z) = -\frac{(a-r^*)w_r^* + w(r^*)}{(a-r^*)^2}.$$

Once this system of equations is solved, we have a quadratic expression approximating the velocity profile. The model is then implemented as

$$R_t = \frac{1}{R}\frac{\partial}{\partial z}\left[\int_R^{r^*} r\tilde{w}(r)dr + \int_{r^*}^a rw_{est}(r)dr\right].$$

To estimate the error, we can periodically keep track of the expression $\int_{r^*}^a r[w(r) - w_{est}(r)]dr$.

Experiments are currently being prepared by Jeff Olander using two different non-Newtonian fluids, one of which is hyaluoronic acid (HA). In HA, shear-thinning effects dominate elastic

effects, making it a good candidate for comparison with the model derived here. Comparison of the model to experiments is an ongoing area of research, and further study of this shear-thinning gravity-driven model is left for future work.

BIBLIOGRAPHY

1. Aul, R.W. & Olbricht, W.L. 1990 Stability of a thin annular film in pressure-driven, low-Reynolds-number flow through a capillary. *J. Fluid Mech.* **215**, 585-599.
2. Benjamin, T.B. 1959 Shearing flow over a wavy boundary. *J. Fluid Mech.* **6**, 161-205.
3. Benney, D.J. 1966 Long waves in liquid films. *J. Math. Phys.* **45**, 150-155.
4. Camassa, R., Forest, M.G., Lee, L., Ogrosky, H.R. & Olander, J. 2012 Ring waves as a mass transport mechanism in air-driven core-annular flows. *Phys. Rev. E* **86**, 066305-1-11.
5. Camassa, R. & Lee, L. 2006 *Advances in Engineering Mechanics - Reflections and Outlooks*, Chwang, A., Teng, M. & Valentine, D. eds., World Scientific, 222-238.
6. Campana, D.M., Ubal, S., Giavedoni, M. & Saita, F. 2007 Stability of the steady motion of a liquid plug in a capillary tube. *Ind. Eng. Chem. Res.* **46**, 1803-1809.
7. Chang, H.-C. & Demekhin, E.A. 2002 *Complex Wave Dynamics on Thin Films*. Elsevier, Amsterdam.
8. Chang, H.-C., Demekhin, E.A. & Kopelevich, D.I. 1993 Laminarizing effects of dispersion in an active-dissipative nonlinear medium. *Physica D* **63**, 299-320.
9. Chen, S. *et al.* 1998 Camassa-Holm equations as a closure model for turbulent channel and pipe flow. *Phys. Rev. Lett.* **81**, 5338-5341.
10. Clarke, S.W., Jones, J.G., & Oliver, D.R. 1970 Resistance to two-phase gas-liquid flow in airways. *J. Appl. Physiol.* **29**, 464-471.
11. Craster, R.V. & Matar, O.K. 2006 On viscous beads flowing down a vertical fibre. *J. Fluid Mech.* **553**, 85-105.
12. Craster, R.V. & Matar, O.K. 2009 Dynamics and stability of thin liquid films. *Rev. Mod. Phys.* **81**, 1131-1198.
13. den Toonder, J.M.J. & Nieuwstadt, F.T.M. 1997 Reynolds number effects in a turbulent pipe flow for low to moderate Re. *Phys. Fluids* **9**, 3398-3409.
14. Doedel, E.J. *et al.* 2008 AUTO-07P: Continuation and bifurcation software for ordinary differential equations.
15. Duprat, C. *et al.* 2009 Liquid film coating a fiber as a model system for the formation of bound states in active dispersive-dissipative nonlinear media. *Phys. Rev. Lett.* **103**, 234501.
16. Duprat, C., Ruyer-Quil, C., Kalliadasis, S. & Giorgiutti-Dauphine, F. 2007 Absolute and convective instabilities of a viscous film flowing down a vertical fiber. *Phys. Rev. Lett.* **98**, 244502.
17. Eggels, J.G.M., Westerweel, J. & Nieuwstadt, F.T.M. 1993 Direct numerical simulation of turbulent pipe flow. *Appl. Sci. Res.* **51**, 319-324.
18. Frenkel, A.L. 1992 Nonlinear theory of strongly undulating thin films flowing down vertical cylinders. *Europhys. Lett.* **18**, 583-588.
19. Frenkel, A.L. *et al.* 1987 Annular flows can keep unstable films from breakup: nonlinear saturation of capillary instability. *J. Colloid and Interface Sci.* **115**, 225-233.

20. Gauglitz, P.A. & Radke, C.J. 1990 The dynamics of liquid film breakup in constricted cylindrical capillaries. *J. Colloid Interface Sci.* **134**, 14-40.

21. Georgiou, E. *et al.* 1992 An asymptotic theory for the linear stability of a core-annular flow in the thin annular limit. *J. Fluid Mech.* **243**, 653-677.

22. Goren, S.L. 1962 The instability of an annular thread of fluid. *J. Fluid Mech.* **27**, 309-319.

23. Halpern, D. & Grotberg, J.B. 1992 Fluid-elastic instabilities of liquid-lined flexible tubes. *J. Fluid Mech.* **244**, 615-632.

24. Hammond, P.S. 1983 Nonlinear adjustment of a thin annular film of viscous fluid surrounding a thread of another within a circular cylindrical pipe. *J. Fluid Mech.* **137**, 363-384.

25. Hickox, C. 1971 Instability due to viscosity and density stratification in axisymmetric pipe flow. *Phys. Fluids* **14**, 251-262.

26. Hsu, S.T. 1968 Turbulent flow in wavy pipes. *Ph.D. Thesis, The University of Iowa* Iowa City, Iowa.

27. Hsu, S.-T. & Kennedy, J.F. 1971 Turbulent flow in wavy pipes. *J. Fluid Mech.* **47**, 481-502.

28. Huerre, P. & Monkewitz, P.A. 1990 Local and global instabilities in spatially developing flows. *Annu. Rev. Fluid Mech.* **22**, 473-537.

29. Hyman, J.M., Nicolaenko, B. & Zaleski, S. 1986 Order and complexity in the Kuramoto-Sivashinsky model of weakly turbulent interfaces. *Physica D* **23**, 265-292.

30. Jensen, O.E. 2000. Draining collars and lenses in liquid-lined vertical tubes. *J. Coll. Int. Sci.* **221**, 38-49.

31. Johnson, M. *et al.* 1991 The nonlinear growth of surface-tension-driven instabilities of a thin annular film. *J. Fluid Mech.* **233**, 141-156.

32. Johnson, M.A. *et al.* 2012 Spectral stability of periodic wave trains of the Korteweg-de Vries/Kuramoto-Sivashinsky equation in the Korteweg-de Vries limit. *arXiv:1202.6402v1*

33. Joseph, D.D. *et al.* 1997 Core-annular flows. *Annu. Rev. Fluid Mech.* **29**, 65-90.

34. Joseph, D., Renardy, M. & Renardy, Y. 1984 Instability of the flow of two immiscible liquids with different viscosities in a pipe. *J. Fluid Mech.* **141**, 309-317.

35. Joseph, D.D. & Renardy, Y. 1993 *Fundamentals of Two-Fluid Dynamics, Part 2: Lubricated Transport, Drops, and Miscible Liquids.* Springer Verlag, New York.

36. Kalliadasis, S. & Chang, H.-C. 1994 Drop formation during coating of vertical fibers. *J. Fluid Mech.* **261**, 135-168.

37. Keller, J.B., Rubinow, S.I. & Tu, Y.O. 1973 Spatial instability of a jet. *Phys. Fluids* **16**, 2052-2055.

38. Kerchman, V.I. 1995 Strongly nonlinear interfacial dynamics in core-annular flows. *J. Fluid Mech.* **290**, 131-166.

39. Kerchman, V.I. & Frenkel, A.L. 1994 Interactions of coherent structures in a film flow: Simulations of a highly nonlinear evolution equation. *Theor. Comput. Fluid Dyn.* **6**, 235-254.

40. Kim, C.S. *et al.* 1986 Criteria for mucus transport in the airways by two-phase gas-liquid flow mechanism. *J. Appl. Physiol.* **60**, 901-907.

41. Kim, C.S. *et al.* 1986 Mucus transport in the airways by two-phase gas-liquid flow mechanism: continuous flow model. *J. Appl. Physiol.* **60**, 908-917.

42. Kim, C.S., Iglesias, A.J., & Sackner, M.A. 1987 Mucus clearance by two-phase gas-liquid flow mechanism: asymmetric periodic flow model. *J. Appl. Physiol.* **62**, 959-971.

43. Kliakhandler, I.L., Davis, S.H. & Bankoff, S.G. 2001 Viscous beads on vertical fibre. *J. Fluid Mech.* **429**, 381-390.

44. Kouris, C. & Tsamopoulos, J. 2001 Dynamics of axisymmetric core-annular flow in a straight tube: I. The more viscous fluid in the core, bamboo waves. *Phys. Fluids* **13**, 841.

45. Kouris, C. &Tsamopoulos, J. 2002 Dynamics of the axisymmetric core-annular flow. II. The less viscous fluid in the core, saw tooth waves. *Phys. Fluids* **14**, 1011-1029.

46. Laufer, J. 1953 The structure of turbulence in fully developed pipe flow. *National Advisory Committee for Aeronautics.*

47. Lin, S.P. 1974 Finite amplitude side-band stability of a viscous film. *J. Fluid Mech.* **63**, 417-429.

48. Lin, S.P. & Liu, W.C. 1975 Instability of film coating of wires and tubes. *AIChE J.* **24**, 775-782.

49. Lister, J.R. *et al.* 2006 Capillary drainage of an annular film: the dynamics of collars and lobes. *J. Fluid Mech.* **552**, 311-343.

50. Manna, M. & Vacca, A. 2001 Scaling properties of turbulent pipe flow at low Reynolds number. *Computers and Fluids* **30**, 393-415.

51. Ma, T. & Wang, S. 2001 *Nonlinear Analysis: Real World Applications.* **1**, 467.

52. Malamataris, N.A. & Balakotaiah, V. 2008 Flow structure underneath the large amplitude waves of a vertically falling film. *AIChE* **54**, 1725-1740.

53. McKeon, B.J. *et al.* 2004 Friction factors for smooth pipe flow. *J. Fluid Mech.* **511**, 41-44.

54. Miles, J.W. 1957 On generation of surface waves by shear flows. *J. Fluid Mech.* **3**, 185-204.

55. Moore, M.N.J. & Shelley, M.J. 2012 A weak-coupling expansion for viscoelastic fluids applied to dynamic settling of a body. *J. Non-Newtonian Fluid Mech.* **183-184**, 25-36.

56. Mouza, A.A., Pantzali, M.N. & Paras, S.V. 2005 Falling film and flooding phenomena in small diameter vertical tubes: the influence of liquid properties. *Chem. Eng. Sci.* **60**, 4981-4991.

57. Mouza, A.A., Paras, S.V. & Karabelas, A.J. 2002 The influence of small tube diameter on falling film and flooding phenomena. *Intl. J. Multiphase Flow* **28**, 1311-1331.

58. Novbari, E. & Oron, A. 2009 Energy integral method for the nonlinear dynamics of an axisymmetric thin liquid film falling on a vertical cylinder. *Phys. Fluids* **21**, 062107.

59. Novbari, E. & Oron, A. 2010 Analysis of time-dependent nonlinear dynamics of the axisymmetric liquid film on a vertical circular cylinder: Energy integral model. *Phys. Fluids* **23**, 012105.

60. Ogawa, T. 1902 Traveling wave solutions to a perturbed Korteweg-de Vries equation. *Hiroshima Math J.* **24**, 401-422.

61. Oron, A., Davis, S.H. & Bankoff, S.G. 1997 Long-scale evolution of thin liquid films. *Rev. Mod. Phys.* **69**, 932-980.

62. Oron, A. & Gottlieb, O. 2002 Nonlinear dynamics of temporally excited falling liquid films. *Phys. Fluids* **14**, 2622-2636.

63. Palacios-Morales, C. & Zenit, R. 2013 The formation of vortex rings in shear-thinning liquids. *J. Non-Newtonian Fluid Mech.* **194**, 1-13.

64. Papageorgiou, D.T., Maldarelli, C. & Rumschitzki, D.S. 1990 Nonlinear interfacial stability of core-annular film flows. *Phys. Fluids A* **2(3)**, 340-352.

65. Pope, S.B. 2000 *Turbulent Flows*. Cambridge University Press, Cambridge.

66. Pumir, A., Manneville, P. & Pomeau, Y. 1983 On solitary waves running down an inclined plane. *J. Fluid Mech.* **135**, 27-50.

67. Quere, D. 1990 Thin films flowing on vertical fibers. *Europhys. Lett.* **13(8)**, 721-726.

68. Roberts, A.J. & Li, Z. 2006 An accurate and comprehensive model of thin fluid flows with inertia on curved substrates. *J. Fluid Mech.* **553**, 33-73.

69. Roy, R.V., Roberts, A.J. & Simpson, M.E. 2002 A lubrication model of coating flows over a curved substrate in space. *J. Fluid Mech.* **454**, 235-261.

70. Ruyer-Quil, C. *et al.* 2008 Modelling film flows down a fibre. *J. Fluid Mech.* **603**, 431-462.

71. Ruyer-Quil, C. & Kalliadasis, S. 2012 Wavy regimes of film flow down a fiber. *Phys. Rev. E* **85**, 046302.

72. Ruyer-Quil, C. & Manneville, P. 2000 Improved modeling of flows down inclined planes. *Eur. Phys. J. B* **15**, 357-369.

73. Sisoev, G., Craster, R., Matar, O. & Gerasimov, S. 2006 Film flow down a fibre at moderate flow rates. *Chem. Eng. Sci.* **61**, 7279-7298.

74. Smolka, L., North, J. & Guerra, B. 2008 Dynamics of free surface perturbations along an annular viscous film. *Phys. Rev. E* **77**, 036301.

75. Suresh, V. & Grotberg, J.B. 2005 The effect of gravity on liquid plug propagation in a two-dimensional channel. *Phys. Fluids* **17**, 031507.

76. Thorsness, C.B., Morrisroe, P.E. & Hanratty, T.J. 1978 A comparison of linear theory with measurements of the variation of shear stress along a solid wave. *Chem. Eng. Sci.* **33**, 579-592.

77. Trifonov, Y. 1992 Steady-state traveling waves on the surface of a viscous liquid film falling down on vertical wires and tubes. *AIChE J.* **38**, 821-834.

78. Trifonov, Y. & Tsvelodub, O. 1991 Nonlinear waves on the surface of a falling liquid film. Part I. Waves of the first family and their stabiliy. *J. Fluid Mech.* **229**, 531-554.

79. Tseluiko, D. & Kalliadasis, S. 2011 Nonlinear waves in counter-current gas-liquid film flow. *J. Fluid Mech.* **673**, 19-59.

80. Ubal, S. *et al.* 2008 Stability of the steady-state displacement of a liquid plug driven by a constant pressure difference along a prewetted capillary tube," Ind. Eng. Chem. Res. **47**, 6307-6315.

81. White, F.M. 1991 *Viscous Fluid Flow*. McGraw-Hill, New York.

82. Yih, C.-S. 1967 Instability due to viscosity stratification. *J. Fluid Mech.* **27**, 337-352.

83. Zagarola, M.V. & Smits, A.J. 1998 Mean-flow scaling of turbulent pipe flow. *J. Fluid Mech.* **373**, 33-79.

84. Zhang, Y.L., Matar, O.K. & Craster, R.V. 2002 Surfactant spreading on a thin weakly viscoelastic film. *J. Non-Newtonian Fluid Mech.* **105**, 53-78.

85. Zilker, D.P., Cook, G.W. & Hanratty, T.J. 1977 Influence of the amplitude of a solid wavy wall on a turbulent flow. Part 1. Non-separated flows. *J. Fluid Mech.* **82**, 29-51.